

Mapping the sensitivity of hadronic experiments to nucleon structure

Bo-Ting Wang,^{1,*} T. J. Hobbs,^{1,2,†} Sean Doyle,¹ Jun Gao,³
Tie-Jiun Hou,⁴ Pavel M. Nadolsky,^{1,‡} and Fredrick I. Olness¹

¹*Department of Physics, Southern Methodist University,
Dallas, TX 75275-0181, U.S.A.*

²*Jefferson Lab, EIC Center, Newport News, VA 23606, U.S.A.*

³*INPAC, Shanghai Key Laboratory for Particle Physics and Cosmology,
School of Physics and Astronomy,
Shanghai Jiao-Tong University, Shanghai 200240, China*

⁴*School of Physics Science and Technology, Xinjiang University,
Urumqi, Xinjiang 830046 China*

Determinations of the proton's collinear parton distribution functions (PDFs) are emerging with growing precision due to increased experimental activity at facilities like the Large Hadron Collider. While this copious information is valuable, the speed at which it is released makes it difficult to quickly assess its impact on the PDFs, short of performing computationally expensive global fits. As an alternative, we explore new methods for quantifying the potential impact of experimental data on the extraction of proton PDFs. Our approach relies crucially on the Hessian correlation between theory-data residuals and the PDFs themselves, as well as on a newly defined quantity — the *sensitivity* — which represents an extension of the correlation and reflects both PDF-driven and experimental uncertainties. This approach is realized in a new, publicly available analysis package PDFSENSE, which operates with these statistical measures to identify particularly sensitive experiments, weigh their relative or potential impact on PDFs, and visualize their detailed distributions in a space of the parton momentum fraction x and factorization scale μ . This tool offers a new means of understanding the influence of individual measurements in existing fits, as well as a predictive device for directing future fits toward the highest impact data and assumptions. Along the way, many new physics insights can be gained or reinforced. As one of many examples, PDFSENSE is employed to rank the projected impact of new LHC measurements in jet, vector boson, and $t\bar{t}$ production and leads us to the conclusion that inclusive jet production at the LHC has a potential for playing an indispensable role in future PDF fits. These conclusions are independently verified by preliminarily fitting this experimental information and investigating the constraints they supply using the Lagrange multiplier technique.

Keywords: parton distribution functions; hadron structure; Large Hadron Collider; Higgs boson

arXiv:1803.02777v4 [hep-ph] 23 Jan 2019

*Electronic address: botingw@mail.smu.edu

†Electronic address: tjhobbs@smu.edu

‡Electronic address: nadolsky@physics.smu.edu

Contents

I. Introduction	3
II. PDF preliminaries	7
A. Data residuals in a global QCD analysis	7
B. Visualization of the global fit with the help of residuals	8
C. Manifold learning and dimensionality reduction	10
1. <i>PCA and t-SNE visualizations</i>	10
2. <i>Reciprocated distances</i>	11
III. Quantifying distributions of residual variations	13
A. Correlation cosine	14
B. Sensitivity in the Hessian method	14
C. Sensitivity in the Monte-Carlo method	16
IV. Case study: CTEQ-TEA global data	16
A. Maps of correlations and sensitivities	16
B. Experiment rankings according to cumulative sensitivities	20
C. Estimating the impact of LHC datasets on CTEQ-TEA fits	21
D. Comparing PDFSENSE predictions to post-fit constraints from Lagrange Multiplier scans	22
V. Conclusions	25
Acknowledgments	27
A. Approximate kinematical variables	27
B. Tabulated results	28
C. Supplementary Material	28
References	42

I. INTRODUCTION

The determination of collinear parton distribution functions (PDFs) of the nucleon is becoming an increasingly precise discipline with the advent of high-luminosity experiments at both colliders and fixed-target facilities. Several research groups are involved in the rich research domain of the modern PDF analysis [1–7]. By quantifying the distribution of a parent hadron’s longitudinal momentum among its constituent quarks and gluons, PDFs offer both a description of the hadronic structure and an essential ingredient of perturbative QCD computations. PDFs enjoy a symbiotic relationship with high-energy experimental data, in the sense that they are crucial for understanding hadronic collisions in the Standard Model (SM) and beyond, while reciprocally benefiting from a wealth of high-energy data that constrain the PDFs. In fact, since the start of the Large Hadron Collider Run II (LHC Run II), the volume of experimental data pertinent to the PDFs is growing with such speed that keeping pace with the rapidly expanding datasets and isolating measurements of greatest impact presents a significant challenge for PDF fitters. This paper intends to meet this challenge by presenting a method for identifying high-value experiments which constrain the PDFs and the resulting SM predictions that depend on them.

That such expansive datasets can constrain the PDFs is a consequence of the latter’s universality — a feature which relies upon QCD factorization theorems to separate the inherently nonperturbative PDFs (at long distances) from process-dependent, short-distance matrix elements. For instance, the cross section for inclusive single-particle hadroproduction (of, *e.g.*, a weak gauge boson W/Z) in proton-proton collisions at the LHC is directly sensitive to the nucleon PDFs via an expression of the form

$$\begin{aligned} \sigma(AB \rightarrow W/Z+X) &= \sum_n \alpha_s^n(\mu_R^2) \sum_{a,b} \int dx_a dx_b \\ &\times f_{a/A}(x_a, \mu^2) \hat{\sigma}_{ab \rightarrow W/Z+X}^{(n)}(\hat{s}, \mu^2, \mu_R^2) f_{b/B}(x_b, \mu^2), \end{aligned} \quad (1)$$

in which $f_{a/A}(x_a, \mu^2)$ represents the PDF for a parton of flavor f_a carrying a fraction x_a of the 4-momentum of proton p_A at a factorization scale μ ; the n^{th} -order hard matrix element is denoted by $\hat{\sigma}_{ab \rightarrow W/Z+X}^{(n)}(\hat{s}, \mu^2, \mu_R^2)$ and is dependent upon the partonic center-of-mass energy $\hat{s} = x_a x_b s$, in which s is the center-of-mass energy of the initial hadronic system; and μ_R is the renormalization scale in the QCD coupling strength $\alpha_s(\mu_R)$. In Eq. (1), subleading corrections $\sim \Lambda^2/M_{W/Z}^4$ have been omitted, and we emphasize that factorization theorems like Eq. (1) have been proved to arbitrary order in α_s for essential observables in the global PDF analysis, such as the inclusive cross sections in DIS and Drell-Yan processes. For compactness and generality, we shall refer henceforth to a PDF for the parton of flavor f simply as $f(x, \mu)$.

Given this formalism, one is confronted with the problem of finding those experiments that provide reliable new information about the PDF behavior. With the proliferation of potentially informative new data, incorporating them all into a global QCD fit inevitably incurs significant cost both in terms of computational resources and required fitting time. Indeed, tremendous progress in the precision of PDFs and robustness of SM predictions is driven by the technology for performing global analysis that has vastly grown in complexity and sophistication. Nowadays, the state-of-the-art in perturbative QCD (pQCD) treatments are done at NNLO (and increasingly even N³LO), and advanced statistical techniques are commonly employed in PDF error estimation. The magnitude of this subject is vast, and we refer the interested reader to Refs. [8, 9] for comprehensive reviews. The tradeoff of this progress is that the impact of an experiment on the ultimate PDF uncertainty is often hard to foresee without doing a complicated fit. Various publications claim sensitivity of new experiments to the PDFs. In this paper, we look into these claims using statistical techniques that bypass doing the fits, and with an eye on theoretical, experimental, and methodological components relevant at the NNLO precision.

The potential cost is steepened by the large size of the global datasets usually involved. This point can be seen in Fig. 1, which plots the default dataset considered in the present analysis in a space of partonic momentum fraction x and factorization scale μ . We label these data as the “CTEQ-TEA set,” given that it is an extension of the 3287 raw data points (given by the sum over N_{pt} in Tables II and III) treated in the NNLO CT14HERA2 analysis of Ref. [10], now augmented by the inclusion of 734 raw data points (given by the sum over N_{pt} in Table IV) from more recent LHC data. These raw measurements can ultimately be mapped to 5227 typical $\{x, \mu\}$ values in Fig. 1, such that each symbol corresponds to a data point from an experiment shown in the legend, at the approximate x and μ values characterizing the data point as described in Appendix A. The experiments are labeled by a short-hand name which includes the year of final publication (*e.g.*, “HERAI+II’15” — corresponding to the 2015 combined HERA Run I and Run II data), following the translation key also given in Tables II–IV of App. B. The experiments included in the CT14HERA2 analysis are listed in the left column and upper part of the right column of the legend, while the newer LHC data considered for the upcoming CTEQ-TEA analysis are the last 14 entries of the right column.

The growing complexity of PDF fitting stimulates development of less computationally involved approaches to

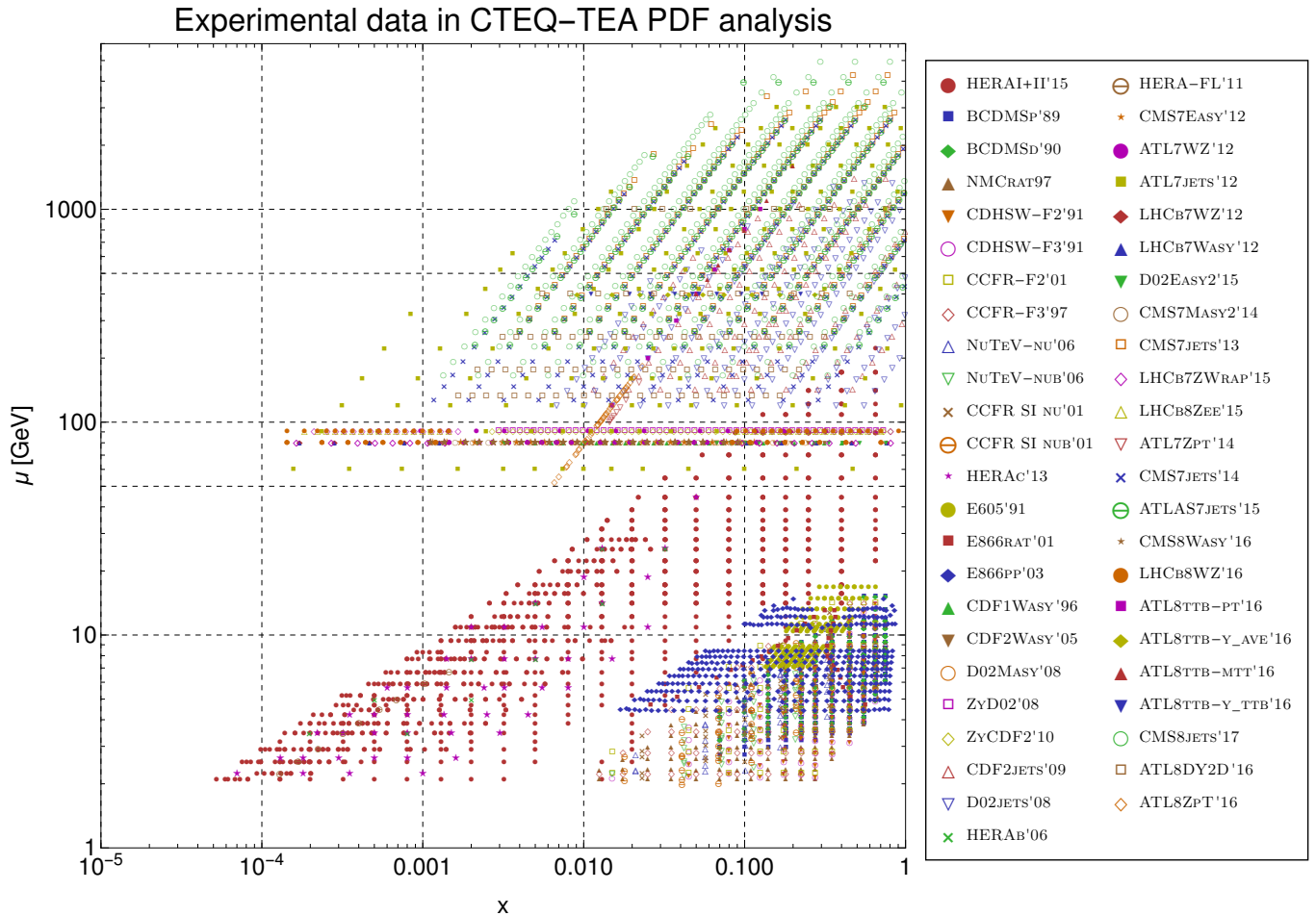


FIG. 1: A graphical representation of the space of $\{x, \mu\}$ points probed by the full dataset treated in the present analysis, designated as “CTEQ-TEA”. It represents an expansion to include newer LHC data of the CT14HERA2 dataset [10] fitted in the most recent CT14 framework [1], which involved measurements from Run II of HERA [6]. Details of the datasets corresponding to the short-hand names given in the legend may be found in Tables II–IV.

estimate the impact of new experimental data on full global fits, such as Hessian profiling techniques [11] and Bayesian reweighting [12, 13] of PDFs. Although these approaches do simulate the expansion of a particular global fit by including theretofore absent dataset(s), they are also limited in that the interpretation of their outcomes is married to the specific PDF parametrization and definition of PDF errors. For example, conclusions obtained by PDF reweighting regarding the importance of a given data set strongly depend on the assumed statistical tolerance or the choice of reweighting factors [14, 15].

Parallel to these efforts, the notion of using correlations between the PDF uncertainties of two physical observables was proposed in Refs. [16, 17] as a means of quantifying the degree to which these quantities were related based upon their underlying PDFs. The PDF-mediated correlation C_f in this case, which we define in Sec. III A, embodies the Pearson correlation coefficient computed by a generalization of the “master formula” [18] for the Hessian PDF uncertainty. The Hessian correlation was deployed extensively in Ref. [19] to explore implications of the CTEQ6.6 PDFs for envisioned LHC observables. It proved to be instrumental for identifying the specific PDF flavors and x ranges most correlated with the PDF uncertainties for W , Z , H , and $t\bar{t}$ production cross sections as well as other processes. The Pearson correlation coefficient has also proven to be informative in the approach based on Monte-Carlo PDF replicas, see, e.g., Refs. [20, 21]. However, the PDF-mediated correlation with a theoretical cross section is only partly indicative of the sensitivity of the experiment. The constraining power of the experiment also depends on the size of experimental errors that were not normally considered in correlation studies, as well as on correlated systematic effects that are increasingly important.

As a remedy to these limitations, we introduce a new format for the output of CTEQ-TEA fits and a natural extension of the correlation technique to quantify the sensitivity of any given experimental data point to a PDF-

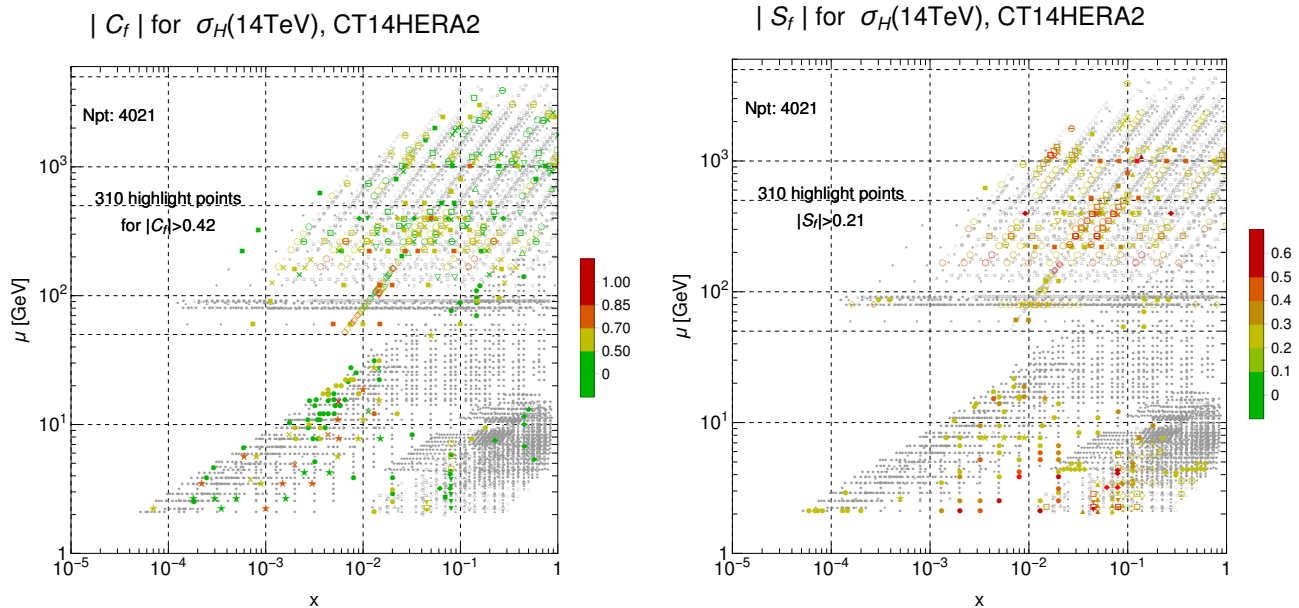


FIG. 2: For the full CTEQ-TEA dataset of Fig. 1, we show the absolute correlation $|C_f|$ and sensitivity $|S_f|$ associated with the 14 TeV Higgs production cross section $\sigma_{H^0}(14 \text{ TeV})$. 310 input data points with most significant magnitudes of $|C_f|$ and $|S_f|$ are highlighted with color. When only the $|C_f|$ plot is considered, only a very small subpopulation of jet production data (diagonal open circles and closed squares with $\mu \gtrsim 100 \text{ GeV}$) exhibits significant correlations with $|C_f| > 0.7$ (orange and red colors), as well as some HERA DIS, high- p_T Z boson, and $t\bar{t}$ production data points. Our novel definition for the sensitivity in the right panel, on the other hand, reveals more points that have comparable potency for constraining the Higgs cross section. In this case, a larger fraction of the jet production points is important (especially CMS measurements of CMS8jets'17 and CMS7jets'14), as well as a number of other processes at smaller μ , particularly DIS data from HERA, BCDMS, NMC, CDHSW, and CCFR (experiments HERAI+II'15, BCDMSd'90, NMCrat'97, CDHSW-F2'91, CCFR-F2'01, CCFR-F3'97). Although its cumulative impact is comparatively modest, ATLAS $t\bar{t}$ production data (ATL8ttb-pt'16, ATL8ttb-y_ave'16, ATL8ttb-mtt'16, ATL8ttb-y_ttb'16) register significant per-point sensitivities, as do E866 pp Drell-Yan pair production (E866pp'03), LHCb W, Z production (LHCb7ZWrap'15, LHCb8WZ'16), and charge lepton asymmetries at D0 and CMS (D02Masy'08, CMS7Masy2'14, CMS7Easy'12). Similarly, some of the high- p_T Z production information (ATL7ZpT'14, ATL8ZpT'16) from ATLAS provide modest constraints.

dependent observable of the user's choice. In this approach, we work with *statistical residuals* quantifying the goodness-of-fit to individual data points. We demonstrate that the complete set of residuals computed for Hessian PDF sets characterizes the CTEQ-TEA fit well enough to permit a means of gauging the influence of empirical information on PDFs in a fashion that does not require complete refits.

A generalization of the PDF-mediated correlations called the *sensitivity* S_f — to be characterized in detail in Sec. III B — better identifies those experimental data points that tightly constrain PDFs both by merit of their inherent precision and their ability to discriminate among PDF error fluctuations. Such an approach aids in identifying regions of $\{x, \mu\}$ for which PDFs are particularly constrained by physical observables.

In fact, in the numerical approach presented in the forthcoming sections, the user can quantify the sensitivity of data not only to individual PDF flavors, but even to specific physical observables, including the modifications due to correlated systematic uncertainties in every experiment of the CT14HERA2 analysis. For example, for Higgs boson production via gluon fusion ($gg \rightarrow H$) at the LHC 14 TeV, the short-distance cross sections are known up to N³LO with a scale uncertainty of about 3% [22]. It has been suggested that $t\bar{t}$ production and high- p_T Z boson production on their own constrain the gluon PDF in the x region sensitive to the LHC Higgs production, and that these are comparable to the constraints from LHC and Tevatron data [23, 24]. Verifying the degree to which this hypothesis is true has been difficult without actually including all these data in a fit.

As an alternative to doing a full global fit, we can critically assess this supposition in the context of the entire global dataset of Fig. 1 using the Hessian correlations and sensitivities, $|C_f|$ and $|S_f|$. The detailed procedure is explained in Secs. III A and III B. In the example at hand, we could rely on the established wisdom that the theoretical cross sections that have an especially large correlation with σ_{H^0} may constrain the PDF dependence of σ_{H^0} ; say, when $|C_f| \gtrsim 0.7$ [19]. Along this reasoning, the left frame in Fig. 2 illustrates 310 experimental data points in $\{x, \mu\}$ space that have the highest absolute correlation, $|C_f|$, between the point's statistical residual defined in Sec. III A

and the cross section σ_{H^0} at 14 TeV via the CT14HERA2 NNLO PDFs. To locate such points in the figure, we highlighted them with color according to the convention shown on the color scale to the right. The respective $|C_f|$ for the highlighted data points ranges between 0.42 and 1. The rest of the data points have smaller correlations and are shown in gray.

We find that the 310 data points with the highest correlation for σ_{H^0} belong to 20 experiments. Nearly all of them are contributed by HERA Neutral Current (NC) DIS, LHC and Tevatron jet production, and HERA charm production. Some of the data points with highest $|C_f|$ come from high- p_T Z boson and even $t\bar{t}$ production.

The correlations C_f , however, do not reflect the experimental uncertainties, which vary widely across the experiments. In the left panel of Fig. 2, fewer than 30 points have a strong correlation of 0.7 or more; but more data points impose relevant constraints in the global fit. To include the information about the uncorrelated and correlated experimental errors, in the right panel of Fig. 2, we plot the distributions of 310 data points with the highest sensitivity parameter S_f , which more faithfully reproduces the actual constraints during the fitting. In general, we find substantial differences between the C_f and S_f distributions. Even the most significant correlations, of order $|C_f| \sim 0.7$ and above, do not guarantee a significant contribution of the experimental point to the log-likelihood χ^2 if the errors are large. On the other hand, we argue that $|S_f|$ is closely related to a contribution of the data point to χ^2 . According to the distribution in the right figure, the 310 data points with the highest sensitivity $|S_f|$ to $\sigma_{H^0}(14 \text{ TeV})$ arise from 27 experiments. Among these data points, only some have a large correlation $|C_f|$ with $\sigma_{H^0}(14 \text{ TeV})$. Nonetheless, they have medium-to-large sensitivity, $|S_f| > 0.21$, according to the criterion developed in Sec. III B. We stress that, while one might suggest plausible dynamical reasons why certain experiments might be particularly sensitive to Higgs production via the gluon PDF, (*e.g.*, via the leading-order qg and gg hard cross sections in jet production and DGLAP scaling violations in inclusive DIS), this reasoning alone does not predict the actual sensitivity revealed by S_f in the presence of multiple experimental constraints.

As one noticeable difference from the $|C_f|$ figure, while inclusive DIS at HERA continues to contribute a large number of data points (about 80) with a high $|S_f|$, also the fixed-target DIS experiments (BCDMS, NMC, CDHSW, CCFR) contribute about the same number of sensitive points in the right panel that were not identified by large correlations. Other sensitive points belong to the jet production data sets from ATLAS and CMS and some vector boson production experiments (muon charge asymmetries at D0, CMS; E866 low-energy Drell-Yan production; LHCb 7 TeV W and Z cross sections).

On the other hand, HERA charm production, ATLAS 7/8 TeV high- p_T Z production, have suppressed sensitivities despite their large correlations, reflecting the larger experimental uncertainties in these measurements. While the LHC $t\bar{t}$ production experiments have large per-point sensitivities, they contribute relatively little to χ^2 because of their small total number of data points. From this comparison, one finds, perhaps somewhat unexpectedly, that fixed-target DIS experiments impose important constraints on $\sigma_{H^0}(14 \text{ TeV})$, thus complementing the HERA inclusive DIS data. One would conclude that efforts to constrain PDF-based SM predictions for Higgs production by relying only on a few points of $t\bar{t}$ data, but to the neglect of high-energy jet production points, would be significantly handicapped by the absence of the latter. We will return to this example in Sec. IV.

The discriminating power of a sensitivity-based analysis therefore forms the primary motivation for this work, and we present the attendant details below. To assess information about the PDFs encapsulated in the residuals for large collections of hadronic data implemented in the CTEQ-TEA global analysis, we make available a new statistical package PDFSENSE to map the regions of partonic momentum fractions x and QCD factorization scales μ where the experiments impose strong constraints on the PDFs. In companion studies, we have applied PDFSENSE to select new data sets for the next generation of the CTEQ-TEA global analysis, to quantitatively explore the physics potential for constraining the PDFs at a future Electron-Ion Collider (EIC) [25–28] and Large Hadron-Electron Collider (LHeC) [29], and to investigate the potential of high-energy data to inform lattice-calculable quantities [30] like the Mellin moments of structure functions [31] and quark quasi-distributions [32]. We reserve many instructive results for follow-up publications currently in preparation, while presenting select calculations in this article to demonstrate the power of the method. We find that the sensitivity technique generally agrees with the preliminary CTEQ-TEA fits and Hessian reweighting realized in the ePUMP program [33]. However, assessing the sensitivity is much simpler than doing the global fit. It does not require access to a fitting program or the application of (potentially subtle) PDF reweighting techniques.

The remainder of the article proceeds as follows. Pertinent aspects of the PDFs and their standard determination via QCD global analyses are summarized in Sec. II. Then, we introduce *normalized residual variations* to extract, visualize, and quantify statistical information about the global QCD fit. In Sec. III, we construct a number of statistical quantities that characterize the PDF constraints in the global analysis using the residual variations. In Sec. IV, we apply the thus constructed sensitivity parameter to examine the impact of various CTEQ-TEA datasets on extractions of the gluon PDF $g(x, \mu)$. In this section and in the conclusion contained in Sec. V, we emphasize a number of *physics insights* that we obtained by applying our sensitivity analysis techniques. Additional aspects of the technique and supplementary tables are reserved for Apps. A, B, and C.

II. PDF PRELIMINARIES

A. Data residuals in a global QCD analysis

While various theoretical models exist for computing nucleon PDFs [34–36], unambiguous evaluation of the PDFs entirely in terms of QCD theory is not yet possible due to the fact that the PDFs can in general receive substantial nonperturbative contributions at infrared momenta. For this reason, precise PDF determination has proceeded mainly through the technique of the QCD global analysis — a method enabled by QCD factorization and PDF universality.

In this approach, a highly flexible parametric form is ascribed for the various flavors in a given analysis at a relatively low scale Q_0^2 . For example, one might take the input PDF for a given quark flavor f to be a parametric form

$$f(x, \mu^2 = Q_0^2) = A_{f,0} x^{A_{f,1}} (1-x)^{A_{f,2}} F(x; A_{f,3}, \dots), \quad (2)$$

in which $F(x; A_{f,3}, \dots)$ can be a suitable polynomial function, *e.g.*, a Chebyshev or Bernstein polynomial, or replaced with a feed-forward neural network $\text{NN}_f(x)$ as in the NNPDF approach. While the full statistical theory for PDF determination and error quantification is beyond the intended range of this analysis, roughly speaking, a best fit is found for a vector \vec{A} of N PDF parameters A_l by minimizing a goodness-of-fit function χ^2 describing agreement of the QCD data and physical observables computed in terms of the PDFs. Based on the behavior of χ^2 in the neighborhood of the global minimum, it is then possible to construct an ensemble of error PDFs to quantify uncertainties of PDFs at a predetermined probability level.

There are various ways to evaluate uncertainties on PDFs, *e.g.*, the Hessian [16, 18], the Monte Carlo [37, 38], and the Lagrange Multiplier approaches [39]. In this analysis our default PDF input set is CT14HERA2, which uses the Hessian method to estimate uncertainties and is therefore based on the quadratic assumption for $\chi^2(\vec{A})$ in the vicinity of the global minimum. In the Hessian method, an orthonormal basis of PDF parameters \vec{a} is derived from the input PDF parameters \vec{A} by the diagonalization of a Hessian matrix H , which encodes the second-order derivatives of χ^2 with respect to A_l . The eigenvector PDF combinations \vec{a}_l^\pm are found for two extreme variations from the best-fit vector \vec{a}_0 along the direction of the l^{th} eigenvector of H allowed at a given probability level. The uncertainty on a QCD observable X can then be estimated with one of the available “master formulas” [17, 18], the “symmetric” variety of which is

$$\Delta X = \frac{1}{2} \sqrt{\sum_{l=1}^N (X_l^+ - X_l^-)^2}. \quad (3)$$

In the CTEQ-TEA global analysis, the χ^2 function accounts for multiple sources of experimental uncertainties, as well as for some prior theoretical constraints on the a_l parameters. Consequently, the global χ^2 function takes the form

$$\chi_{\text{global}}^2 = \sum_E \chi_E^2 + \chi_{\text{th}}^2, \quad (4)$$

where the sum runs over all experimental datasets (E); and χ_{th}^2 imposes theoretical constraints. The complete formulas for χ_E^2 and χ_{th}^2 can be found in Ref. [40]. For the purposes of this paper, we express χ_E^2 for each experiment E in a compact form as a sum of squared *shifted residuals* $r_i^2(\vec{a})$, which are summed over N_{pt} individual data points i in this experiment, as well as the contributions of N_λ best-fit nuisance parameters $\bar{\lambda}_\alpha$ associated with correlated systematic errors:

$$\chi_E^2(\vec{a}) = \sum_{i=1}^{N_{pt}} r_i^2(\vec{a}) + \sum_{\alpha=1}^{N_\lambda} \bar{\lambda}_\alpha^2(\vec{a}). \quad (5)$$

In turn, $r_i(\vec{a})$ for the i^{th} data point is constructed from the theoretical prediction $T_i(\vec{a})$ evaluated in terms of PDFs, total uncorrelated uncertainty s_i , and the shifted central data value $D_{i,sh}(\vec{a})$:

$$r_i(\vec{a}) = \frac{1}{s_i} (T_i(\vec{a}) - D_{i,sh}(\vec{a})). \quad (6)$$

This representation arises in the Hessian formalism due to the presence of correlated systematic errors in many experimental datasets, which require χ_E^2 to depend on nuisance parameters λ_α . This is in addition to the dependence

of χ_E^2 on the PDF parameters \vec{a} and theoretical parameters such as $\alpha_s(M_Z)$ and particle masses. The λ_α parameters are optimized for each \vec{a} according to the analytic solution derived in Appendix B of Ref. [18]. Optimization effectively shifts the central value D_i of the data point by an amount determined by the optimal nuisance parameters $\bar{\lambda}_\alpha(\vec{a})$ and the correlated systematic errors $\beta_{i\alpha}$:

$$D_i \rightarrow D_{i,sh}(\vec{a}) = D_i - \sum_{\alpha=1}^{N_\lambda} \beta_{i\alpha} \bar{\lambda}_\alpha(\vec{a}) . \quad (7)$$

It should be noted that the contribution of the squared best-fit nuisance parameters to χ_E^2 in Eq. (5) is dominated in general by the first term involving the shifted residuals, which tends to be much larger — especially for more sizable datasets.

We point out also that some alternative representations for χ^2 include the correlated systematic errors via a covariance matrix $(\text{cov})_{ij}$, rather than the above mentioned CTEQ-preferred form that explicitly operates with λ_α . Various χ^2 definitions in use are reviewed in [41], as well as in [7]. Crucially, however, the representations based upon operating with λ_α and $(\text{cov})_{ij}$ are derivable from each other [40]. From an extension of the derivation in Ref. [18], we may relate the shifted residual to the covariance matrix at an i^{th} point and optimal nuisance parameters as

$$r_i(\vec{a}) = s_i \sum_{j=1}^{N_{pt}} (\text{cov}^{-1})_{ij} (T_j(\vec{a}) - D_j) , \quad (8)$$

$$\bar{\lambda}_\alpha(\vec{a}) = \sum_{i,j=1}^{N_{pt}} (\text{cov}^{-1})_{ij} \frac{\beta_{i\alpha} (T_j(\vec{a}) - D_j)}{s_i s_j} , \quad (9)$$

where

$$(\text{cov}^{-1})_{ij} = \left[\frac{\delta_{ij}}{s_i^2} - \sum_{\alpha,\beta=1}^{N_\lambda} \frac{\beta_{i\alpha} A_{\alpha\beta}^{-1} \beta_{j\beta}}{s_i^2 s_j^2} \right] , \quad (10)$$

and

$$A_{\alpha\beta} = \delta_{\alpha\beta} + \sum_{k=1}^{N_{pt}} \frac{\beta_{k\alpha} \beta_{k\beta}}{s_k^2} . \quad (11)$$

Thus, even for those PDF analyses which operate with the covariance matrix one is still able to determine the shifted residuals r_i from $(\text{cov}^{-1})_{ij}$ using Eq. (8). In this article, we conveniently follow the CTEQ methodology and obtain $r_i(\vec{a})$ directly from the CTEQ-TEA fitting program, together with the optimal nuisance parameters $\bar{\lambda}_\alpha(\vec{a})$ and shifted central data values $D_{i,sh}(\vec{a})$.

B. Visualization of the global fit with the help of residuals

The shifted residuals r_i draw our interest because, in consequence of the definitions in Eqs. (5)-(6), they contain substantial low-level information about the agreement of PDFs with every data point in the global QCD fit in the presence of systematic shifts. The response of $r_i(\vec{a})$ to the variations in PDFs depends on the experiment type and kinematic range associated with the i^{th} data point, and the totality of these responses can be examined with modern data-analytical methods. The sum of squared residuals over all points of the global dataset renders the bulk of the log-likelihood, or experimental, component χ_E^2 of the global χ^2 . In turn, the root-mean-squared residual $\langle r_0 \rangle_E$ for experiment E and the central PDF set \vec{a}_0 is tied to $\chi_E^2(\vec{a}_0)/N_{pt}$, the standard measure of agreement with experiment E at the best fit:

$$\langle r_0 \rangle_E \equiv \sqrt{\frac{1}{N_{pt}} \sum_{i=1}^{N_{pt}} r_i^2(\vec{a}_0)} = \sqrt{\frac{1}{N_{pt}} \left(\chi_E^2(\vec{a}_0) - \sum_{\alpha=1}^{N_\lambda} \bar{\lambda}_\alpha^2(\vec{a}_0) \right)} \approx \sqrt{\frac{\chi_E^2(\vec{a}_0)}{N_{pt}}} . \quad (12)$$

Notice that $\langle r_0 \rangle_E \approx 1$ when the fit to the experimental data set E is good.

We will now invoke the Hessian formalism to first organize the analysis of the PDF dependence of individual residuals, and then introduce a framework to evaluate sensitivity of individual data points to PDF-dependent physical observables. To test the effectiveness of the proposed method, we study constraints using CT14HERA2 parton distributions [10] fitted to datasets from DIS processes, $Z \rightarrow l^+l^-$, $d\sigma/dy_l$, $W \rightarrow l\nu$, and jet production ($p_1p_2 \rightarrow jjX$). We include both the experiments that were used to construct the CT14HERA2 dataset, as well as a number of LHC experiments that may be fitted in the future. The experimental data sets are summarized in Tables II-IV.

Given the urgency in improving constraints on the gluon PDF for investigations of the Higgs sector, we focus attention on several candidate experiments that may probe $g(x, \mu)$: high- p_T Z -boson production (ATL8ZpT'16, ATL7ZpT'14), $t\bar{t}$ production (ATL8ttb-pt'16, ATL8ttb-y_ave'16, ATL8ttb-mtt'16, ATL8ttb-y_ttb'16), as well as high-luminosity or alternative data sets for jet production, such as the high-luminosity ATLAS 7 TeV jet data (ATLAS7jets'15) that is to replace the counterpart low-luminosity set ATL7jets'12, or the CMS 7 TeV jet data set (CMS7jets'14) that extends to lower jet p_T and higher rapidity, $2.5 < |y_j| < 3$, than the previously fitted CMS 7 TeV jet data set (CMS7jets'13).¹ The dependence of such experiments on $g(x, \mu)$ is scrutinized in a number of ways. We examine their statistical properties using both the PDFs from the CT14HERA2 NNLO analysis, which already impose significant constraints on the large- x gluon using the Tevatron inclusive jet data sets, CDF2jets'09 and D02jets'08; and in some comparisons using a special version of the NNLO PDFs that are fitted to the same CT14HERA2 data set, except without including the above jet data sets. As yet another aspect, we investigate a range of measurements of Drell-Yan pair production cross sections and charge lepton asymmetries with the goal to understand their sensitivity predominantly to the (anti)quark sector.

To parametrize the response of a residual \vec{r}_i , we evaluate it for every eigenvector PDF \vec{a}_l^\pm of the CT14HERA2 PDF set with $N = 28$ PDF parameters. Then, given the *normalized residual variations*

$$\delta_{i,l}^\pm \equiv (r_i(\vec{a}_l^\pm) - r_i(\vec{a}_0)) / \langle r_0 \rangle_E \quad (13)$$

between the residuals for the PDF eigenvectors \vec{a}_l^\pm and for the CT14HERA2 central PDF \vec{a}_0 , we construct a $2N$ -dimensional vector

$$\vec{\delta}_i = \left\{ \delta_{i,1}^+, \delta_{i,1}^-, \dots, \delta_{i,N}^+, \delta_{i,N}^- \right\} \quad (14)$$

for each data point of the global dataset.

The components of $\vec{\delta}_i$ parametrize responses of r_i to PDF variations along the independent directions given by \vec{a}_l^\pm . The differences are normalized to the central root-mean-square (r.m.s.) residual $\langle r_0 \rangle_E$ of experiment E [see Eq. (12)] so that the normalized residual variations do not significantly depend on $\chi^2(\vec{a}_0)/N_{pt}$, the quality of fit to experiment E . Recall that a substantial spread over the fitted experiments is generally obtained for χ_E^2/N_{pt} . Moreover, it is reasonable to expect significantly larger values for χ_E^2/N_{pt} for the experiments that have not been yet fitted, but are included in the analysis of the residuals, *e.g.*, the new LHC experiments shown in Fig. 1. With the definitions in Eqs. (13) and (14), however, $\vec{\delta}_i$ is only weakly sensitive to χ_E^2/N_{pt} .

Thus, we represent the PDF-driven variations of the residuals of a global dataset by a bundle of vectors $\vec{\delta}_i$ in a $2N$ -dimensional space.² This mapping opens the door to applying various data-analytical methods for classification of the data points and identifying the data points of the utmost utility for PDF fits. As the length of $\vec{\delta}_i$ is equal to the PDF-induced fractional error on r_i as compared to the average residual at the best fit, it can be argued that important PDF constraints arise from new data points that either have a large $|\vec{\delta}_i|$ or are otherwise distinct from the existing data points. Conversely, new data points with a small $|\vec{\delta}_i|$, or the ones that are embedded in the preexisting clusters of points, are not likely to improve constraints on the PDFs.

¹ As a result, a small number of data points that contributes to both the data sets CMS7jets'14 and CMS7jets'13 is double-counted in the histograms, without affecting the conclusions.

² In this section, we consider separate variations along \vec{a}_l in the positive and negative directions. Alternatively, it is possible to work with a vector of N symmetric differences $\delta_{i,l} \equiv (r_i(\vec{a}_l^+) - r_i(\vec{a}_l^-)) / (2\langle r_0 \rangle_E)$ and arrive at similar conclusions. Symmetric differences will be employed to construct correlations and sensitivities in Sec. III.

C. Manifold learning and dimensionality reduction

1. PCA and t-SNE visualizations

We illustrate a possible analysis technique carried out with the help of the TensorFlow Embedding Projector software for the visualization of high-dimensional data [42]. A table of 4021 vectors $\vec{\delta}_i$ for the CTEQ-TEA dataset (corresponding to our total number of raw data points) is generated by our package PDFSENSE and uploaded to the Embedding Projector website. As variations along many eigenvector directions result only in small changes to the PDFs, the 56-dimensional $\vec{\delta}_i$ vectors can in fact be projected onto an effective manifold spanned by fewer dimensions. Specifically, the Embedding Projector approximates the 56-dimensional manifold by a 10-dimensional manifold using principal component analysis (PCA). In practice, this 10-dimensional manifold is constructed out of the 10 components of greatest variance in the effective space, such that the most variable combinations of $\delta_{i,l}$ are retained, while the remaining 46 components needed to fully reconstruct the original 56-dimensional $\vec{\delta}_i$ are discarded. However, because the 10 PCA-selected components describe the bulk of the variance of $\delta_{i,l}$, the loss of these 46 components results in only a minimal relinquishment of information, and in fact provides a more efficient basis to study $\delta_{i,l}$ variations.

We encourage the reader to download the table of the normalized residual variations $\vec{\delta}_i$ for CT14HERA2 NNLO from the PDFSENSE website [43] and explore it for themselves using the Embedding Projector [42] or another program for multidimensional data visualization such as a tour [44]. These tools help to understand the detailed PDF dependence of individual data sets *without doing the global fit*. Performing such task has been challenging for non-experts, if not for the PDF fitters themselves. With the proposed method, we can visually examine the PDF dependence of the residuals from the diverse data sets before quantitatively characterizing these distributions using the estimators developed in the next sections. In the future, a computer algorithm can be written to select the experimental data for PDF fits, based on the residual variations, and with minimal involvement from humans.

To offer an illustration, while grasping the full PDF dependence of the data points in the original 56-parameter space is daunting, in the 10-dimensional representation obtained via PCA, some directions result in efficient separation of the data points of different types according to their residual variations. The left panel of Fig. 3 shows one such 3-dimensional projection of $\vec{\delta}_i$ that separates clusters of residual variations arising from data for DIS, vector boson production, and jet/ $t\bar{t}$ production. In this example, the jet/ $t\bar{t}$ cluster, shown in red, is roughly orthogonal to the blue DIS cluster and intersects it. This separation is quite remarkable, as it is based only on numerical properties of the $\vec{\delta}_i$ vectors, and not on the meta-data about the types of experiments that is entered only after the PCA is completed; in other projections, the data types are not separated. The underlying reasons for this separation, namely, dependence on independent PDF combinations, will be quantified by the sensitivities in the next section.

As an alternative, the Embedding Projector can organize the $\vec{\delta}_i$ vectors into clusters according to their similarity using t -distributed stochastic neighbor embedding (t-SNE) [45]. A representative 3-dimensional distribution of the vectors obtained by t-SNE is displayed in the right panel of Fig. 3. In the figure, we show that the t-SNE method is able to identify and separate the clusters of data according to the experimental process (DIS, vector production, or jet production). In fact, the reader can perform the t-SNE analysis on the Embedding Projector website themselves and verify that it actually sorts the $\vec{\delta}_i$ vectors into the clusters according to their values of x and μ , and even the experiment itself. This exercise demonstrates, yet again, that the statistical residuals provided in PDFSENSE reflect the key properties of the global fit. Information can be extracted from them and examined in a number of ways.

The breakdown of the vectors over experiments in the PCA representation is illustrated by Fig. 4. Here, we see that the bulk of the DIS cluster from the left Fig. 3 originates with the combined HERA1+2 DIS data [HERAI+II'15]. The jet cluster in Fig. 3 will be dominated by ATLAS and CMS inclusive jet datasets [CMS7jets'14, ATLAS7jets'15, and CMS8jets'17], which add dramatically more points across a wider kinematical range on top of the CDF Run-2 and D0 Run-2 jet production datasets (CDF2jets'09) and (D02jets'08).

In contrast, although the $t\bar{t}$ production experiments (ATL8ttb-pt'16, ATL8ttb-y_ave'16, ATL8ttb-mtt'16, ATL8ttb-y.tt'16) are generally characterized by large $\vec{\delta}_i$ vectors, they contribute only a few data points lying within the jet cluster of Fig. 4 and, by themselves, will not make much difference in a global fit. The same conclusion applies to data from high- p_T Z production, which has too few points to stand out in a fit with significant inclusive jet data samples. We return to this point in the discussion of reciprocated distances below.

It is also interesting to note that semi-inclusive charm production at HERA [HERAc'13] lies between, and partly overlaps with, the DIS and jet clusters. Finally, CCFR/NuTeV dimuon semi-inclusive DIS [SIDIS] (CCFR-F2'01, CCFR-F3'97, NuTeV-nu'06, NuTeV-nub'06) extends in an orthogonal direction, not well separated from the other datasets in the selected three-dimensional projection.

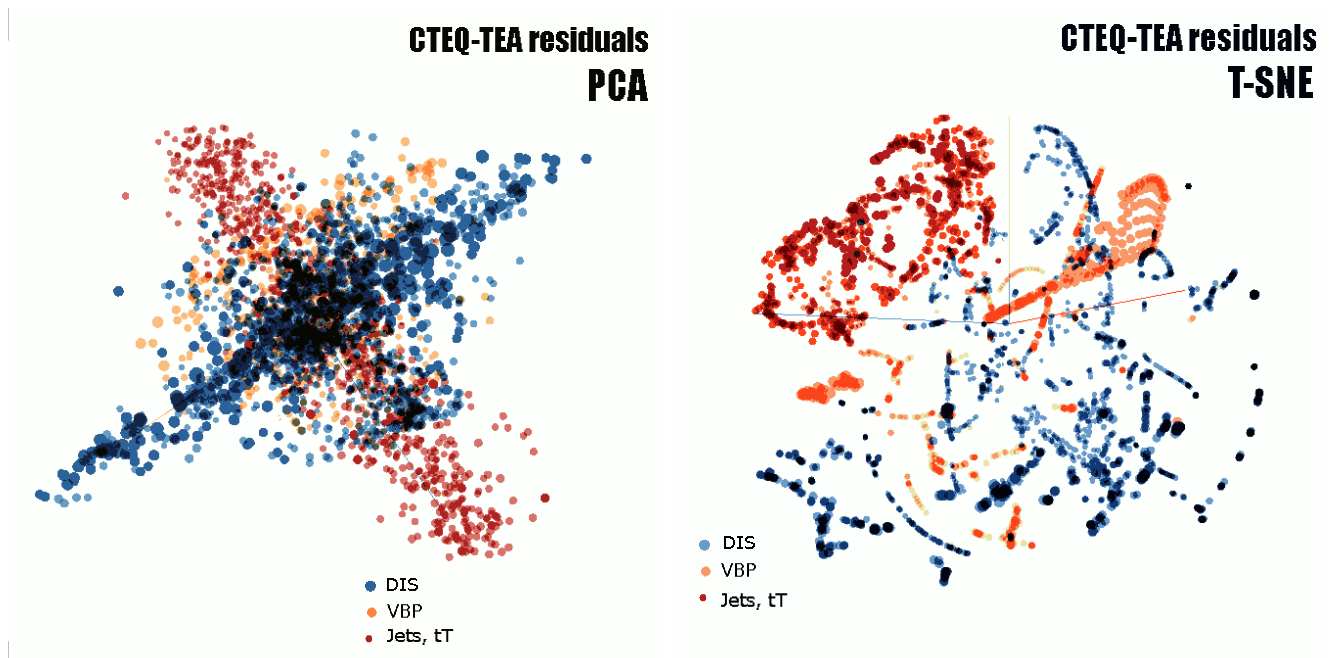


FIG. 3: Distributions of residual variations $\vec{\delta}_i$ from the CTEQ-TEA analysis obtained by dimensionality reduction methods. Left: a 3-dimensional projection of a 10-dimensional manifold constructed by principal component analysis (PCA). Right: a distribution from the 3-dimensional t-SNE clustering method. Blue, orange, and red colors indicate data points from DIS, vector boson production, and jet/ $t\bar{t}$ production processes.

2. Reciprocated distances

As a complement to the visualization methods based on PCA and t-SNE just presented, it is also possible to evaluate another similarity measure based on the distances between the vectors of the residual variations. For example, rather than applying the PCA to an ensemble of $\vec{\delta}_i$ vectors to perform dimensionality reduction, we might instead compute over the vector space a pair-wise *reciprocated distance* measure, which we define as

$$\mathcal{D}_i \equiv \left(\sum_{j \neq i}^{N_{all}} \frac{1}{|\vec{\delta}_j - \vec{\delta}_i|} \right)^{-1}, \quad (15)$$

and evaluate for the i points in each experimental dataset. We allow the sum over j in Eq. (15) to run over all the data points in the CTEQ-TEA set regardless of experiment (denoted by N_{all}). The distances can be computed either in the 56-dimensional space or in the reduced dimensionality space.³ We plot the result of applying Eq. (15) to the 56-dimensional residual variations of the full CTEQ-TEA dataset computed using two PDF ensembles: CT14HERA2 fitted to all data in the left panel, and CT14HERA2 fitted only to the DIS and vector boson production data (excluding jet production data) in the right panel. Fig. 5 represents the distribution of the reciprocated distances over individual experiments of the CTEQ-TEA dataset. The CT Experiment ID # is shown on the abscissa, and the \mathcal{D}_i values for every point of the experiment are indicated by the scatter points.

The advantage of the definition in Eq. (15) is that it enables a quantitative measure of the degree to which separate experiments broadly differ in terms of their residual variations, and therefore provides information analogous to that found in Figs. 3–4. For example, by inspection of Eq. (15) it can be seen that those experimental measurements which are widely separated from the rest of the CTEQ-TEA dataset in space of $\vec{\delta}_i$ vectors will correspond to comparatively large values of \mathcal{D}_i , and experiments that systematically differ from the rest of the total dataset are thus expected

³ Alternative definitions for the reciprocated distance can be also used, with qualitatively similar conclusions. For example, we could sum over all experimental data, but excluding those points belonging to the same experiment as point i , and normalizing \mathcal{D}_i by $(N_{pt} - N_{all})/N_{pt}$ to compensate for different numbers of points in the experiment.

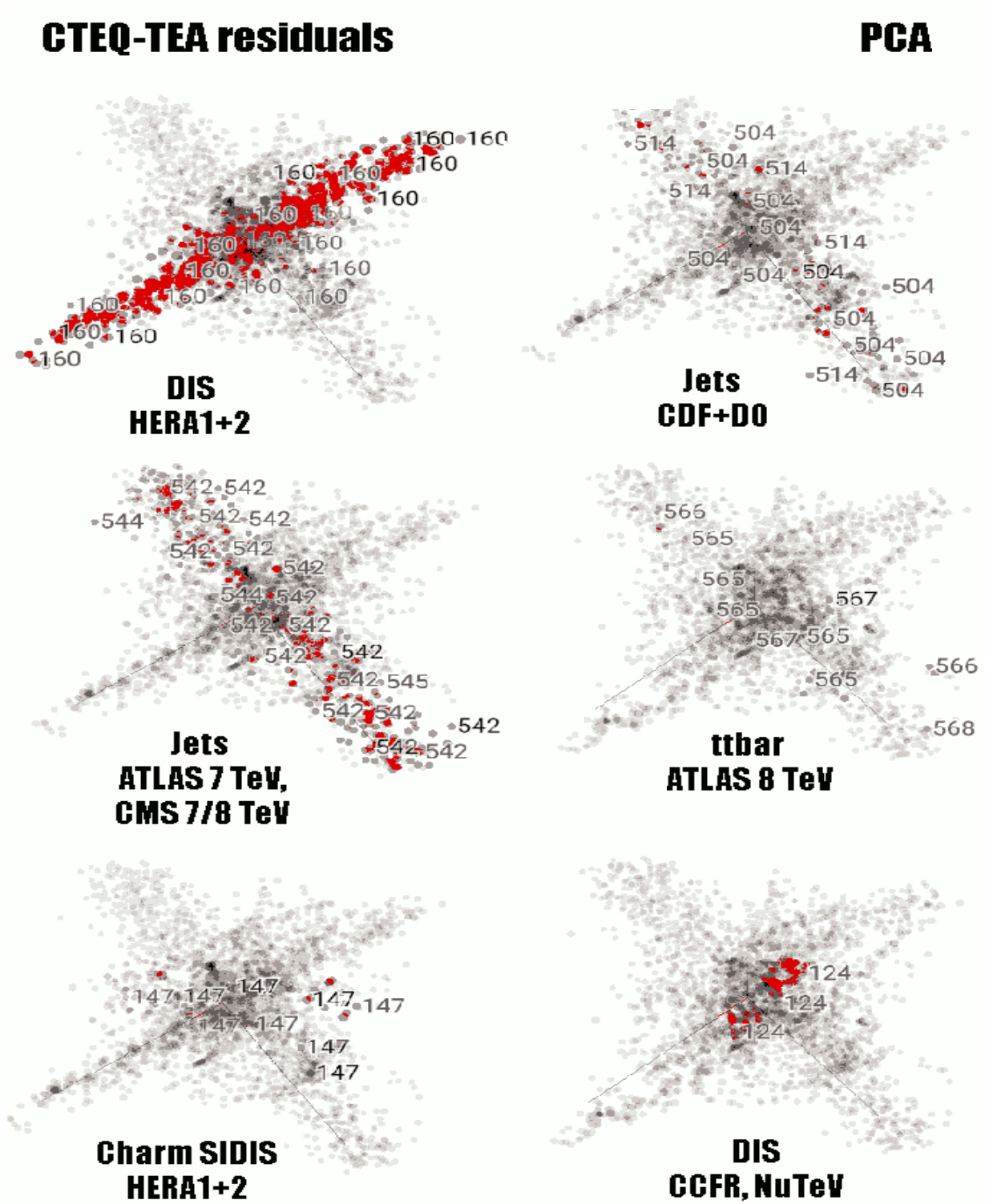


FIG. 4: The PCA distribution from Fig. 3, indicating distributions of points from classes of experiments. In the numbering scheme used here, points labeled 1XX correspond to fixed-target measurements and 5XX to jet and $t\bar{t}$ production as given in Tables II–IV. The specific experiments are noted in the plots.

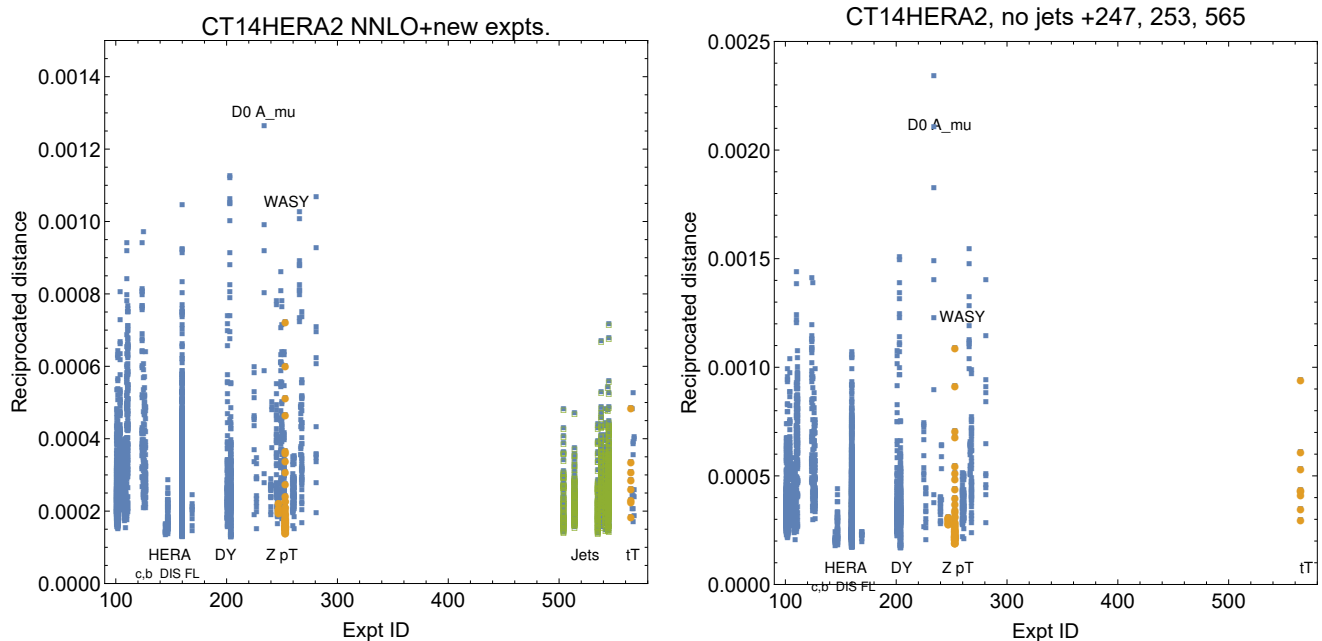


FIG. 5: A plot of the reciprocated distances \mathcal{D}_i obtained from the PDFs fitted to the full CT14HERA2 dataset [left] and to the CT14HERA2 dataset without jet production experiments [right]. The horizontal axis displays numerical experimental CT IDs of the constituent CTEQ-TEA datasets, for each of which is shown a column of values of the reciprocated distance. We highlight columns corresponding to Expt. IDs ATL7ZpT’14 [247], ATL8ZpT’16 [253], and ATL8ttb-pt’16 [565] as discussed in text.

to have especially tall distributions in the panels of Fig. 5. On this basis, it can be seen that information yielded by W asymmetry measurements (D02Masy’08, CMS7Masy2’14, D02Easy2’15) are particularly distinct, as well as the combined HERA DIS data (HERAI+II’15) and fixed-target Drell-Yan measurements, such as E605 (E605’91) and E866 data (E866rat’01 and E866pp’03). Similarly, direct comparison of the \mathcal{D}_i distributions in the panels of Fig. 5 allows one to compare constraints with and without the jet data. We note that the 7 and 8 TeV ATLAS high- p_T Z production (ATL7ZpT’14 and ATL8ZpT’16) and $t\bar{t}$ production (ATL8ttb-pt’16) provide a number of “remote” points and hence are potentially useful in the fits sensitive to the gluon. On the other hand, new jet production experiments (CMS7jets’14, ATLAS7jets’15, CMS8jets’17) all include large numbers of points characterized by significant reciprocated distances.

III. QUANTIFYING DISTRIBUTIONS OF RESIDUAL VARIATIONS

We have demonstrated that the multi-dimensional distribution of the $\vec{\delta}_i$ vectors reflects the PDF dependence of individual data points. In this section, we will focus on numerical metrics to assess the emerging geometrical picture associated with the $\vec{\delta}_i$ distribution, and to visualize the regions of partonic momentum fractions x and QCD factorization scales μ where the experiments impose strong constraints on a given PDF-dependent observable X .

Gradients of r_i in a space of Hessian eigenvector PDF parameters \vec{a} are naturally related to the PDF uncertainty. Recall that in the Hessian method the PDF uncertainty on $X(\vec{a})$ is found as

$$\Delta X(\vec{a}) = X(\vec{a}) - X(\vec{a}_0) = \vec{\nabla} X|_{\vec{a}_0} \cdot \Delta \vec{a}, \quad (16)$$

where \vec{a}_0 is the best-fit combination of PDF parameters, and $\Delta \vec{a}$ is the maximal displacement along the gradient that is allowed within the tolerance hypersphere of radius T centered on the best fit [16, 18]. The standard master formula

$$\Delta X = \left| \vec{\nabla} X \right| = \frac{1}{2} \sqrt{\sum_{l=1}^N (X_l^+ - X_l^-)^2} \quad (17)$$

is obtained by representing the components of $\vec{\nabla}X$ by a finite-difference formula

$$\frac{\partial X}{\partial a_i} = \frac{1}{2}(X_i^+ - X_i^-), \quad (18)$$

in terms of the values X_i^\pm for extreme displacements of \vec{a} within the tolerance hypersphere along the l -th direction.

In this setup, a dot product between the gradients provides a convenient measure of the degree of similarity between PDF dependence of two quantities [19]. A dot product $\vec{\nabla}r_i \cdot \vec{\nabla}f$ between the gradients of a shifted residual r_i and another QCD variable f , such as the PDF at some $\{x, \mu\}$ or a cross section, can be cast in a number of useful forms.

A. Correlation cosine

The correlation for the i^{th} $\{x, \mu\}$ point, which we define following Refs. [8, 16, 17, 19] as

$$C_f \equiv \text{Corr}[f, r_i] = \frac{\vec{\nabla}f \cdot \vec{\nabla}r_i}{\Delta f \Delta r_i}, \quad (19)$$

can determine whether there *may* exist a predictive relationship between f and goodness of fit to the i^{th} point. The correlation function $\text{Corr}[X, Y]$ for the quantities X, Y in Eq. (19) represents the realization in the Hessian formalism of Pearson's correlation coefficient, which we express as

$$\text{Corr}[X, Y] = \frac{1}{4\Delta X \Delta Y} \sum_{j=1}^N (X_j^+ - X_j^-)(Y_j^+ - Y_j^-), \quad (20)$$

with the sum in these expressions being over the j parameters of the full PDF model space. Geometrically, $\text{Corr}[X, Y]$ represents the cosine of the angle that determines the eccentricity of an ellipse satisfying $\chi^2(\vec{a}) < \chi^2(\vec{a}_0) + T^2$ in the $\{X, Y\}$ plane. This latter point follows from the fact that the mapping of the tolerance hypersphere onto the $\{X, Y\}$ plane is an ellipse with an eccentricity that depends on the correlation of X and Y , which is given in turn by Eq. (20) above.

$\text{Corr}[f, r_i]$ does not indicate how constraining the residual is, but it may indicate a predictive relation between r_i and f . On the basis of previous work [19], we say that the (anti-)correlation between X and Y is significant roughly if $|\text{Corr}[X, Y]| \gtrsim 0.7$, while smaller (anti-)correlation values are less robust or predictive. Following this rule-of-thumb, correlations have been used successfully to identify PDF combinations that dominate PDF uncertainties of complicated observables, for instance to show that the gluon uncertainty dominates the total uncertainty on LHC W and Z production, or that the uncertainty on the ratio σ_W/σ_Z of W^\pm and Z^0 boson cross sections at the LHC is dominated by the strangeness PDF, rather than u and d (anti-)quark PDFs [19].

B. Sensitivity in the Hessian method

The correlation C_f alone does not fully encode the potential impact of separate or new measurements on improving PDF determinations in terms of the uncertainty reduction. Rather, we employ $\vec{\nabla}f \cdot \vec{\nabla}r_i$ again to define the *sensitivity* S_f to f of the i^{th} point in experiment E :

$$S_f \equiv \frac{\vec{\nabla}f \cdot \vec{\nabla}r_i}{\Delta f \langle r_0 \rangle_E} = \frac{\Delta r_i}{\langle r_0 \rangle_E} C_f, \quad (21)$$

where Δr_i and $\langle r_0 \rangle_E$ are computed according to Eqs. (3) and (12), respectively. In other words, Δr_i again represents the variation of the residuals across the set of Hessian error PDFs, and we normalize it to the r.m.s. residual for the whole dataset E to reduce the impact of random fluctuations in the data values $D_{i,sh}$. This definition has the benefit of encoding not only the correlated relationship of f with r_i , but also the comparative size of the experimental uncertainty with respect to the PDF uncertainty. In consequence, for example, if new experimental data have reported uncertainties that are much tighter than the present PDF errors, these data would then register as high-sensitivity points by the definition in Eq. (21).

Geometrically, S_f represents a projection onto the direction of the gradient $\vec{\nabla}f$ of the residual variation $\vec{\delta}_i$, defined in Sec. III using the symmetrized formula for $\delta_{i,l}$ noted in footnote 2, namely,

$$\delta_{i,l} \equiv (r_i(\vec{a}_l^+) - r_i(\vec{a}_l^-)) / (2\langle r_0 \rangle_E). \quad (22)$$

C. Sensitivity in the Monte-Carlo method

The above statistical measures are general enough and can be extended to other representations for the PDF uncertainties, such as the representation based on Monte-Carlo replica PDFs [20, 37, 38] of the kind employed, e.g., in the NNPDF framework. A family of Monte-Carlo PDFs consists of N_{rep} member PDF sets $q_a^{(k)}(x, \mu) \equiv \{q^{(k)}\}$, with $k = 1, \dots, N_{\text{rep}}$, and those are used to determine an expectation value $\langle X \rangle$ for a PDF-dependent quantity $X[\{q\}]$ such as a high-energy cross section:

$$\langle X \rangle = \frac{1}{N_{\text{rep}}} \sum_{k=1}^{N_{\text{rep}}} X[\{q^{(k)}\}] . \quad (24)$$

The resulting Monte-Carlo uncertainty on X can be extracted from the ensemble as

$$\Delta_{\text{MC}} X = \left(\frac{1}{N_{\text{rep}} - 1} \sum_{k=1}^{N_{\text{rep}}} \left(X[\{q^{(k)}\}] - \langle X \rangle \right)^2 \right)^{1/2} . \quad (25)$$

In consequence of these definitions, the central value of a particular PDF itself in the NNPDF framework is specified as

$$q_{(0)} \equiv \langle q \rangle = \frac{1}{N_{\text{rep}}} \sum_{k=1}^{N_{\text{rep}}} q^{(k)} . \quad (26)$$

Akin to the Pearson correlation defined in Eq. (19) of Sec. III A, statistical correlations between two PDF-dependent quantities $X[\{q\}]$ and $Y[\{q\}]$ can be constructed from the PDF replica language above in terms of ensemble averages [20]:

$$\text{Corr}_{\text{MC}} [X, Y] = \frac{\langle XY \rangle - \langle X \rangle \langle Y \rangle}{\Delta_{\text{MC}} X \Delta_{\text{MC}} Y} . \quad (27)$$

Then, using our definitions in Eqs. (19) and (21), we immediately construct the realizations of the correlation and sensitivity for a PDF-dependent quantity f in the Monte-Carlo method:

$$C_{f, \text{MC}} = \text{Corr}_{\text{MC}} [f, r_i] , \quad (28)$$

$$S_{f, \text{MC}} = \frac{\Delta_{\text{MC}} r_i}{\langle r_0 \rangle_E} \text{Corr}_{\text{MC}} [f, r_i] . \quad (29)$$

IV. CASE STUDY: CTEQ-TEA GLOBAL DATA

A. Maps of correlations and sensitivities

We will now discuss a number of practical examples of using C_f or S_f to quickly evaluate the impact of various hadronic data sets upon the knowledge of the PDFs in a fashion that does not require a full QCD analysis of the type described in Sec. II. For this demonstration, we will continue to study the dataset shown in Fig. 1 of the CT14HERA2 analysis [10] augmented by the candidate LHC data.

We have already noted the extent of this dataset in the $\{x, \mu\}$ plane in Fig. 1, where it is decomposed into constituent experiments labeled according to the conventions in Tables II-IV. It is instructive to create similar maps in the $\{x, \mu\}$ plane showing the C_f or S_f values for each data point. Such maps are readily produced by the PDFSENSE program for a variety of PDF flavors and for user-defined observables, such as the Higgs cross section. For demonstration we have collected a large number of these maps at the companion website [43]. We invite the reader to review these additional figures while reading the paper to validate the conclusions that will be summarized below.

Thus, we obtain scatter plots of $C_f(x_i, \mu_i)$ or $S_f(x_i, \mu_i)$ for a given QCD observable $f = \sigma$, such as the LHC Higgs production cross section shown in Fig. 2, or with a PDF f evaluated at the same $\{x_i, \mu_i\}$ determined by the data points, with examples shown for $g(x_i, \mu_i)$ in Figs. 7 and 8. The typical $\{x_i, \mu_i\}$ values characterizing the data points are found according to Born-level approximations appropriate for each scattering process included in the CTEQ-TEA dataset, with the formulas to compute these kinematic matchings summarized in App. A. Here and in general, we

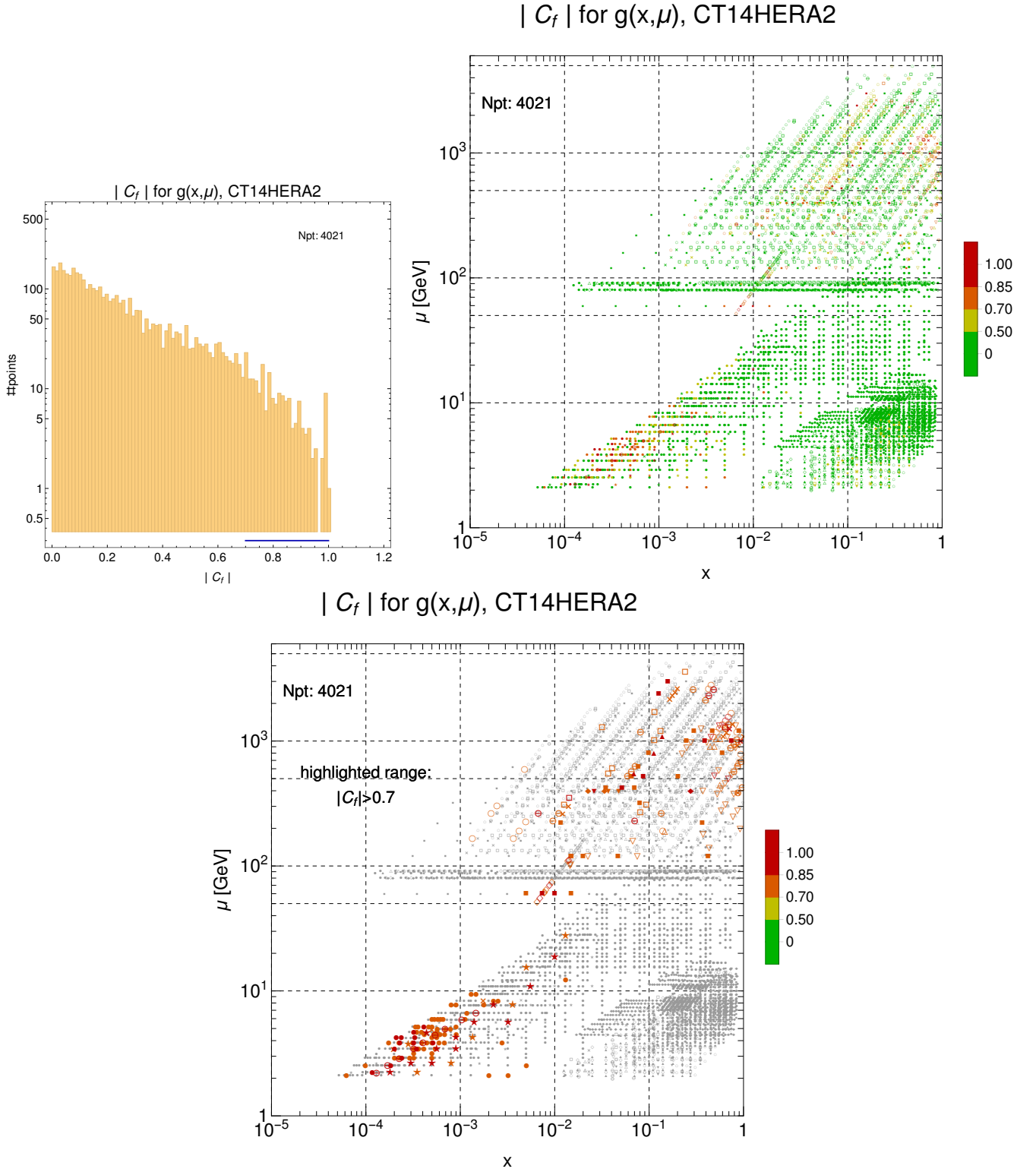


FIG. 7: Representations of the correlation $|C_g|(x_i, \mu_i)$ of the gluon PDF $g(x, \mu)$ with the point-wise residual r_i of the augmented CT14HERA2 analysis. In the first panel, we plot a histogram showing the distribution of correlations for 4021 physical measurements. In the second panel we show the 5227-point $\{x_i, \mu_i\}$ map corresponding to these data within the full dataset, generated as in Appendix A. To adjust for the fact that some measurements of rapidity dependent quantities match to two distinct points in $\{x_i, \mu_i\}$ space using the rules of Appendix A, we assign weights of 0.5 to these complementary $\{x_i, \mu_i\}$ points in computing the $N_{pt} = 4021$ -count histogram at left. The third figure is the same as the second one, but only the data points satisfying $|C_f| > 0.7$ are highlighted.

find it preferable to consider the absolute values $|C_f|$ and $|S_f|$ on the grounds that the signs of C_f and S_f flip when the data points randomly overshoot or undershoot their theory predictions.

Together with the map in the $\{x, \mu\}$ plane, PDFSENSE also returns a histogram of the values for each quantity it plots. An example is shown for $|C_g|(x_i, \mu_i)$ in the first panel of Fig. 7. One would judge that stronger constraints are in general provided to those PDFs for which the $|C_f|$ histogram has many entries comparatively closely to $|C_f| \sim 1$. In the first panel of Fig. 7, we can see that, while the distribution peaks at low correlations, $|C_g| \sim 0$, the distribution has an extended tail in the region $0.7 \lesssim |C_g| \lesssim 1$. This feature shows that, of the 4021 experimental data points within the augmented CT14HERA2 set in Fig. 1, nearly two-hundred — specifically, 192 — have especially strong ($|C_f| \geq 0.7$) correlations (or anti-correlations) with the gluon PDF. This region of such strong correlations within the histogram is indicated by the horizontal blue bar that runs along the abscissa.

To identify these points, we plot complementary information in the second panel of the same figure — specifically, a map in $\{x, \mu\}$ space of each of the data points shown in Fig. 1. As before, they are colorized according to the magnitude of $|C_g|$ following the color palette in the “rainbow strip” on the right. “Cooler” colors (green/yellow) correspond to weaker correlation strengths, while “hotter” colors (orange/red) represent comparatively stronger correlations, as indicated. To reveal the data points with the highest correlations, we reproduce the same figure in the third panel, but showing in color only the data points satisfying $|C_f| > 0.7$. Thus, we obtain two maps in the $\{x, \mu\}$ plane that look similar to the $|C_f|$ map in the left panel of Fig. 2, apart from the differences that (a) Fig. 7 shows the correlation $|C_g|$ for $g(x_i, \mu_i)$ at the same typical values $\{x_i, \mu_i\}$ as in the data, rather than $|C_{\sigma_{H^0}}|$ for Higgs production cross section in Fig. 2; and (b) Fig. 2 highlights 310 points with the highest $|C_{\sigma_{H^0}}|$.

The correlations for the LHC Higgs production cross section trace those for $g(x_i, \mu_i)$, but not entirely, as we will see in a moment. Large magnitudes of $|C_g|$ in Fig. 7 are found for inclusive jet production measurements, especially those recently obtained by CMS at 8 TeV [46] (Expt. CMS8jets’17, inverted triangles) with $|C_g|(x_i, \mu_i)$ as high as 0.85, including at the highest values of x and μ . Beyond these, a sizable cluster of HERA (HERAI+II’15) data points at the lowest values of x are also seen to have large correlations with the gluon PDF, consistent with the common wisdom that HERA DIS constrains the gluon PDF at small x via DGLAP scaling violations. Under the jet production cluster, high- p_T Z production (ATL7ZpT’14, ATL8ZpT’16) and $t\bar{t}$ production (ATL8ttb-pt’16, ATL8ttb-y_ave’16, ATL8ttb-mtt’16, ATL8ttb-y_ttb’16) at the LHC show a high $|C_g|(x_i, \mu_i)$ correlation. At the same time, many other measurements, including fixed-target data at large x and W asymmetry data near $\mu \sim 100$ GeV, have feeble correlations with $g(x_i, \mu_i)$ and would therefore be less emphasized by an analysis based solely upon the PDF-residual correlations.

We can also consider the analogous plots for the sensitivity $|S_g|(x_i, \mu_i)$ as defined in Eq. (21), which we plot in Fig. 8. In the first panel, we again consider the histogram, here for the magnitudes of the gluon sensitivity $|S_g|(x_i, \mu_i)$, in which the correlations $|C_g|$ are now weighted by the relative size of the PDF uncertainty Δr_i in the residual. As discussed in Sec. IIIB, this additional weighting emphasizes those data points for which the PDF-driven fluctuations in the residuals are comparatively large relative to experimental uncertainties. This leads to a redistribution of the data points shown in the $|C_g|$ histogram of Fig. 7, with the result being a considerably longer-tailed histogram for $|S_g|$ such that, in this instance, there are 546 raw data points with larger sensitivities, $|S_f| \geq 0.25$, indicated by the horizontal blue bar. Unlike the correlation, $|S_g|$ can be arbitrarily large, depending on the Δr_i value. It is suppressed at the data points with large uncertainties or smeared over the regions of data points with correlated systematic uncertainties.

In the second and third panels, we show the respective $\{x, \mu\}$ maps for $|S_g|$, with color highlighting given either for all points or only those with high sensitivities $|S_f| > 0.25$, respectively. $|S_g|$ places additional emphasis on the combined HERA dataset (HERAI+II’15) constraining $g(x_i, \mu_i)$ at lowest x . In contrast to the $|C_g|$ plot, we observe increased sensitivity in the precise fixed-target DIS data from BCDMS (BCDMSp’89, BCDMSd’90) and CCFR (CCFR-F2’01, CCFR-F3’97), which are sensitive to the gluon via scaling violations despite only moderate correlation values. Similarly, we observe heightened sensitivities at highest x for the LHC (CMS7jets’14, ATLAS7jets’15, CMS8jets’17) and Tevatron (D02jets’08) jet production data, which have both large correlations with $g(x_i, \mu_i)$ and small experimental uncertainties. Sensitivity $|S_g|$ of LHC jet experiments, CMS7jets’14, ATLAS7jets’15, CMS8jets’17, varies in a large range, and can significantly improve, depending on the implementation of experimental systematic uncertainties in the analysis, cf. the discussion of the jet data in the next section.

We also observe enhanced sensitivity for *individual points* in a large number of experiments, including CDHSW DIS (CDHSW-F2’91); HERA F_L (HERA-FL’11); the Drell-Yan process (E605’91, E866pp’03); CDF 8 TeV W charge asymmetry (CMS7Masy2’14); HERA charm SIDIS (HERAc’13); ATLAS high- p_T Z production (ATL7ZpT’14, ATL8ZpT’16); and especially strongly sensitive points in $t\bar{t}$ production (ATL8ttb-pt’16, ATL8ttb-y_ave’16, ATL8ttb-mtt’16, ATL8ttb-y_ttb’16). However, since the latter category includes fewer points per each experiment, it constrains the gluon less than the high-statistics DIS and jet production data.

These findings comport with the idea that the gluon PDF remains dominated by substantial uncertainties at both $x \sim 0$ and in the elastic limit $x \rightarrow 1$, a fact which has driven an intense focus upon production of hadronic jets, $t\bar{t}$ pairs,

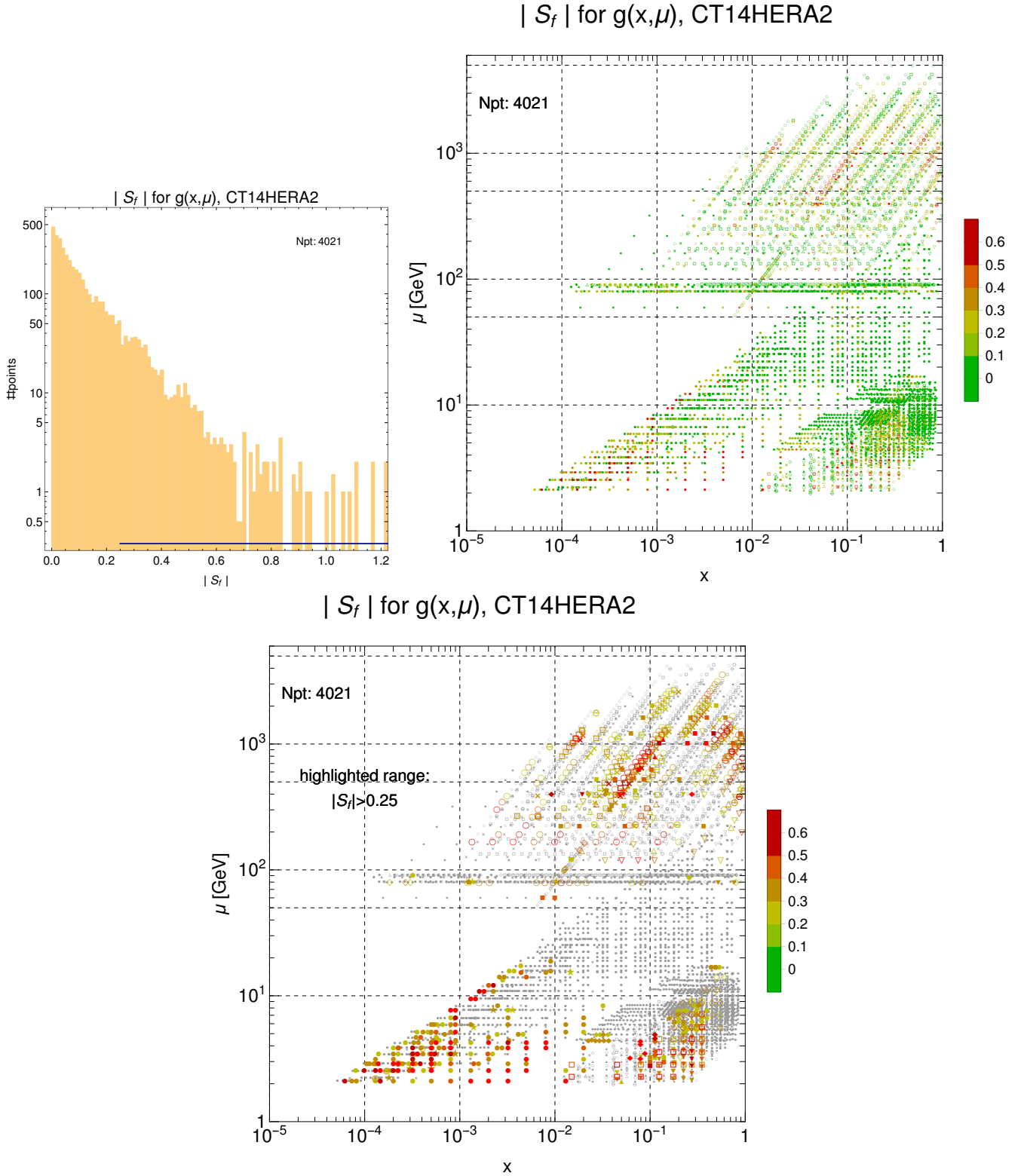


FIG. 8: Like Fig. 7, but for the gluon sensitivity $|S_g|(x_i, \mu_i)$ as defined in Eq. (21). In the third figure, only the data points satisfying $|S_f| > 0.25$ are highlighted.

and high- p_T Z bosons, which themselves are measured at large center-of-mass energies \sqrt{s} and are expected to be sensitive to the gluon PDF across a wide interval of x , including $x \sim 0.01$ typical for Higgs boson production via gluon fusion at the LHC. Turning back to the distributions of $|C_{\sigma_H}|(x_i, \mu_i)$ and $|S_{\sigma_H}|(x_i, \mu_i)$ for the Higgs cross section σ_H at $\sqrt{s} = 14$ TeV in Fig. 2, we notice that they largely reflect the distributions of $|C_g|(x_i, \mu_i)$ and $|S_g|(x_i, \mu_i)$ around $x \sim M_H/\sqrt{s} = 125/14000 = 0.009$ and $\mu = M_H = 125$ GeV. We also see some differences: although the average x and μ are fixed in σ_H , it is nonetheless sensitive to some constraints at much lower x values as a result of the momentum sum rule.

The reader is welcome to examine the plots of sensitivities and correlations available on the PDFSENSE website for a large collection of PDF flavors and PDF ratios, such as d/u , \bar{d}/\bar{u} , and $(s + \bar{s})/(\bar{u} + \bar{d})$. Sensitivities for other PDF combinations and hadronic cross sections can be computed and plotted in a matter of minutes using the PDFSENSE program. We will now turn to another aspect of this analysis: summarizing the abundant information contained in the sensitivity plots. For this purpose, we will introduce numerical indicators and propose a practical procedure to rank the experimental data sets according to their sensitivities to the PDFs or PDF-dependent observables of interest.

B. Experiment rankings according to cumulative sensitivities

Being one-dimensional projections of normalized residual variations $\vec{\delta}_i$ on a given direction in the PDF parameter space, sensitivities can be linearly added to construct a number of useful estimators. By summing absolute sensitivities $|S_f^{(i)}|$ over the data points i of a given data set E , we find the maximal cumulative sensitivity of E to the PDF dependence of a QCD observable f .

Alternatively, from the examination of multiple $\{x, \mu\}$ maps for $|S_f|$ of various PDF flavors collected on the website [43], we find that the most precise experiments constrain several flavors at the same time; most notably, the combined HERA data. For the purpose of identifying such experiments, we can compute an overall sensitivity statistic for each experiment E to the parton distributions $f_a(x_i, \mu_i)$ evaluated at the same kinematic parameters $\{x_i, \mu_i\}$ as the data. Furthermore, to obtain one overall ranking, we can add up sensitivity measures as an unweighted sum over the ‘‘basis PDF’’ flavors, such as the six light flavors ($\bar{d}, \bar{u}, g, u, d, s$). To obtain these measures, we say that an experiment E consisting of N_{pt} physical measurements can be characterized by its mean sensitivity per raw data point⁴ to a PDF of given flavor $f_a(x, \mu)$: $\langle |S_f^E| \rangle \equiv (N_{pt})^{-1} \sum_{i=1}^{N_{pt}} |S_f|(x_i, \mu_i)$, from which we derive several additional statistical measures of experimental sensitivity. For each experiment and flavor we then determine a cumulative sensitivity measure, numerically adjusted to the size of each experimental dataset E , according to $|S_f^E| \equiv N_{pt} \langle |S_f^E| \rangle$. In addition, we also track cumulative, flavor-summed sensitivity measures $\sum_f |S_f^E|$ and $\langle \sum_f |S_f^E| \rangle$, with f running over $\bar{d}, \bar{u}, g, u, d, s$.

We list the corresponding values of these four types of sensitivities for each experiment of the CTEQ-TEA dataset in summary tables in App. B as well as extensive Supplementary Material in App. C. This is also detailed for categories of experiments from the CTEQ-TEA dataset.

With the above estimators, we *quantify* and *compare* the cumulative sensitivities of each experiment to the basis 6 parton flavors. In fact, based on the various trials that we performed, we find that the cumulative sensitivity to the 6 basic flavors is a good measure of the overall sensitivity to a large range of PDF combinations. Recall that the $N_f = 5$ CT14HERA2 PDFs (with up to 11 independent parton species) are obtained by DGLAP evolution of the 6 basic parton flavors from the initial scale of order 1 GeV. There exist alternative approaches for measuring the importance of a given experiment in a global fit, for example, by counting the numbers of eigenvector parameters [47] or eigenvector directions [2] that the experiment constrains. Those other methods, however, require access to the full machinery of the global fit, while the sensitivities allow the reader to rank the experiments according to much the same information, for a variety of PDF-dependent observables, with the help of PDFSENSE, and at a fraction of computational cost.

In fact, in a companion study we use the above sensitivity estimators to select the new LHC experiments for the inclusion in the next generation of the CTEQ-TEA PDF analysis. Full tables given in App. B and in the Supplementary Material of App. C provide detailed information about the PDF sensitivities of every experiment of the CTEQ-TEA data set. For a non-expert reader, along the full tables, we provide their simplified versions in Tables V-VI, where we rank the experimental sensitivities according to a reward system described in the caption of Table V. In each table, experiments are listed in descending order according to the cumulative sensitivity measure $\sum_f |S_f^E|$ to the six light-parton flavors. For each PDF flavor, the experiments with especially high overall flavor-specific sensitivities receive

⁴ For those circumstances in which an individual measurement, *e.g.*, obtained via the Drell-Yan process, maps to two sensitivity values in $\{x, \mu\}$ space, we compute the average of these and assign the result to that specific measurement.

an “A” rating (shown in bold), per the convention in the caption of Table V. Successively weaker overall sensitivities receive marks of “B” and “C,” while those falling below a lower limit $|S_f^E| = 20$ are left unscored.

We similarly evaluate each experimental dataset based on its point-averaged sensitivity, in this case scoring according to a complementary scheme in which the highest score is “1”. The short-hand names of the candidate experiments that were *not* included in the CT14HERA2 NNLO fit, that is, the new LHC experiments, are also shown in bold to facilitate their recognition in the tables.

Not only do the sensitivity rankings confirm findings known by applying other methods, they also provide new insights. According to this ranking system in Tables V-VI, we find that the expanded HERA dataset (HERAI+II’15) tallies the highest overall sensitivity to the PDFs, with enhanced sensitivity to the distributions of the u - and \bar{u} -quarks, as well as that of the gluon. On similar footing, but with slightly weaker overall sensitivities, are a number of other fixed-target measurements, including structure function measurements from BCDMS for $F_2^{p,d}$ (BCDMSp’89, BCDMSd’90) and CCFR extractions of xF_3^p (CCFR-F3’97) — as well as several other DIS datasets. Among the LHC experiments, the inclusive jet measurements have the highest cumulative sensitivities, with CMS jets at 8 TeV (CMS8jets’17), 7 TeV (CMS7jets’13, CMS7jets’14), and ATLAS 7 TeV (ATLAS7jets’15) occupying positions 10, 12/13, and 16 in the total sensitivity rankings. They demonstrate the strongest sensitivities among the candidate LHC experiments, and at the same time are not precise enough and fall behind the top fixed-target DIS and Drell-Yan experiments: BCDMS, CCFR, E605, E866, and NMC. The two versions CMS7jets’13 and CMS7jets’14 of the CMS 7 TeV jet data that largely overlap have very close sensitivities and rankings in Tables V-VI. The set CMS7jets’13 that extends to higher p_{Tj} has a slightly better overall sensitivity, surpassing the larger data set CMS7jets’14 that includes the extra data points at $p_{Tj} < 100$ GeV or $|y_j| > 2.5$, yet cannot beat CMS7jets’13 except for in the overall sensitivity to the Higgs cross section at 7 TeV.

Going beyond the rankings based upon overall sensitivities, which are more closely tied to the impact of an entire experimental dataset in aggregate, it is useful to consider the point-averaged sensitivity as well, which quantifies how sensitive each individual point is. [Some experiments with very high point-averaged sensitivity have a small cumulative sensitivity because of a small number of points.] Based on their high point-averaged sensitivity, CMS μ asymmetry measurements at 8 and 7 TeV (CMS8Wasy’16 and CMS7Masy2’14) especially stand out, despite their small number of individual points, $N_{pt} = 11$; this is especially true again for the gluon, \bar{d} -, and u -quark PDFs, for which this set of measurements is particularly highly rated in Table V. Another “small-size” data set with the exceptional point-average sensitivity is the $\sigma_{pd}/(2\sigma_{pp})$ ratio from the E866 lepton pair production experiment (E866rat’01). The average sensitivity of this data set to \bar{u} and \bar{d} PDFs is 0.8, making it extremely valuable for constraining the ratio \bar{d}/\bar{u} at $x \sim 0.1$, in spite of its small size (15 data points).

Aside from the quark- and gluon-specific rankings of specific measurements, we can also assess experiments based upon the constraints they impose on various interesting flavor combinations and observables as presented in Table VI. As was the case with Table V, a considerable amount of information resides in Table VI of which we only highlight several notable features here. Among these features are the sharp sensitivities to the Higgs cross section (*e.g.*, $|S|_{H7}$, $\langle |S_{H7}| \rangle$, *etc.*) found for Run I+II HERA data, as well as the tier-C overall sensitivities of the BCDMS $F_2^{p,d}$ and CMS jet production measurements, corresponding to Exps. BCDMSd’90, BCDMSp’89, CMS8jets’17 and CMS7jets’14. While their overall sensitivity is small, the corresponding ATLAS $t\bar{t}$ data also possesses significant point-averaged sensitivity. On the other hand, measurements of p_T -dependent Z production (ATL7ZpT’14, ATL8ZpT’16) appear to have somewhat less pronounced sensitivity to the gluon and other PDF flavor combinations. The total and mean sensitivities of high- p_T Z boson production experiment ATL8ZpT’16 at 8 TeV is on par with HERA charm SIDIS data (HERAc’13) and provides comparable constraints to charm DIS production, albeit in a different $\{x, \mu\}$ region.

For the light-quark PDF combinations like u_v , d_v , d/u , and \bar{d}/\bar{u} , the various DIS datasets — led by Run II of HERA and CCFR measurements of the proton structure function — demonstrate the greatest sensitivity. At the same time, however, Run-2 Tevatron data from D0 on the μ asymmetry (D02Easy2’15) and Run-1 CDF measurements for the corresponding $A_e(\eta^e)$ asymmetry (CDF1Wasy’96) also exhibit substantial point-wise sensitivity as well. We collect a number of other observations in the conclusion below, Sec. V.

C. Estimating the impact of LHC datasets on CTEQ-TEA fits

The presented rankings suggest that including the candidate LHC data sets will produce mild improvements in the uncertainties of the CT14 HERA2 PDFs. This projection may appear underwhelming, but keep in mind that the CT14HERA2 NNLO analysis already includes significant experimental constraints, for example, imposed on the gluon PDF at $x > 0.01$ by the Tevatron and LHC jet experiments, CDF2jets’09, D02jets’08, ATL7jets’12, CMS7jets’13. If all jet experiments are eliminated from the PDF fit, as illustrated in the Supplementary Material tables of App. C, the candidate LHC experiments will be promoted to higher rankings, with the CMS 8 and 7 TeV jet experiments

(CMS8jets'17 and CMS7jets'13/CMS7jets'14) elevated to positions 4 and 7/8 in the overall sensitivity rankings, respectively.

Our investigations also find that the sensitivities of CMS jet experiments may improve considerably if the current correlated systematic effects are moderately reduced compared to the published values. For instance, by requiring a full correlation of the JEC2 correlation error over all rapidity bins in the CMS 7 TeV jet data set CMS7jets'14, instead of its partial decorrelation implemented according to the CMS recommendation [48], we obtain a very strong sensitivity of the data set CMS7jets'14 to g over the full $\{x, \mu\}$ region; but also strong sensitivities to \bar{u}, \bar{d} , and even \bar{s} PDFs.⁵ The overall sensitivity of the data set CMS7jets'14 in this case is elevated to the 4th position from the 13th position in the CT14HERA2 NNLO analysis in Tables V and VI. Similarly, for the CMS 8 TeV jet data set CMS8jets'17, the sensitivity to the above flavors can increase under moderate reduction of systematic uncertainties, easily surpassing the sensitivity of CMS7jets'14 because of the larger number of points in CMS8jets'17.

D. Comparing PDFSENSE predictions to post-fit constraints from Lagrange Multiplier scans

How do the surveys based on PDFSENSE compare against the actual fits? As we noted, the PDFSENSE method is designed to provide a fast large-scope estimation of the impact of the existing and future data sets in conjunction with other tools, such as the EPUMP [33] program for PDF reweighting. It works the best in the quadratic (Hessian) approximation near the best fit, and when the new experiments are compatible with the old ones. When detailed understanding of the experimental constraints is necessary, the PDFSENSE approach must be supplemented by other techniques, such as Lagrange multiplier (LM) scans [39, 49, 50].

As an illustration of the scope of the differences between the PDFSENSE predictions before and after the fit, the left panels in Figs. 9 and 10 show the PDFSENSE maps for $d/u(x=0.1, \mu=1.3 \text{ GeV})$ and $g(x=0.01, \mu=125 \text{ GeV})$ evaluated using a preliminary CT18 NNLO fit (designated as ‘‘CT18pre’’) that includes 11 new LHC experimental data sets, namely CMS8jets'17, CMS7jets'14, ATLAS7jets'15, LHCb8WZ'16, CMS8Wasy'16, LHCb8Zee'15, LHCb7ZWrap'15, ATLASZpT'16, ATLAS8ttb-pt'16, ATLAS8ttb-mtt'16, and 8 TeV $t\bar{t}$ production at CMS (‘‘CMS8 ttb pTtyt’’) [51] in addition to the experiments included in the CT14HERA2 fit. The full details of the CT18 fit will be presented in an upcoming publication [52]. Some modifications were made in the methodology adopted in CT18, as compared to CT14HERA2; notably the PDF parametrization forms and treatment of NNLO radiative contributions have been changed, while some shown curves are also subject to a theoretical uncertainty associated with the QCD scale choices. In accord with the PDFSENSE predictions based on the CT14HERA2 NNLO PDFs, we find that including the above LHC experiments into the fit produces only mild differences between the CT18pre and CT14HERA2 NNLO PDFs. Consequently the PDFSENSE $\{x, \mu\}$ maps based on CT18pre NNLO PDFs are similar to the CT14HERA2 ones [43]. One noticeable difference is that the sensitivity of the new experiments decreases after they are included in the CT18pre fit, because the new information from the newly added experiments suppresses PDF uncertainties of data residuals.

In the right panels of Figs. 9 and 10, we illustrate the constraints on the same quantities, $d/u(0.1, 1.3 \text{ GeV})$ and $g(0.01, 125 \text{ GeV})$ in the candidate CT18pre NNLO fit, now obtained with the help of LM scans. A LM scan [39, 49, 50] is a powerful technique that elicits detailed information about a PDF-dependent quantity $X(\vec{a})$, such as a PDF or cross section, from a constrained global fit in which the value of $X(\vec{a})$ is fixed by an imposed condition. By minimizing a modified goodness-of-fit function $\chi_{LM}^2(\lambda, \vec{a})$ that includes a ‘generalized-force’ term equal to $X(\vec{a})$ with weight λ , in addition to the global χ_{global}^2 in Eq. (4), a LM scan reveals the parametric relationship between $X(\vec{a})$ and χ_{global}^2 or χ_{expt}^2 contributions from individual experiments, including any non-Gaussian dependence. In the LM scans at hand, the modified fitted function takes the form

$$\chi_{LM}^2(\lambda, \vec{a}) = \chi_{global}^2(\vec{a}) + \lambda X(\vec{a}), \quad (30)$$

and $X(\vec{a})$ are $d/u(x, \mu)$ or $g(x, \mu)$ at a specific location in $\{x, \mu\}$ space. For the optimal parameter combination $\vec{a} \equiv \vec{a}_0$ at which $\chi_{global}^2(\vec{a})$ is minimized, we find in Fig. 9 that $d/u(0.1, 1.3 \text{ GeV}) \approx 0.7$. The LM scan for the d/u then consists of a series of refits of the parameters \vec{a}_k , as the multiplier parameter λ is dialed along a set of discrete values λ_k , effectively pulling d/u away from the value ~ 0.7 at $\vec{a} = \vec{a}_0$ preferred by the global fit. The right panel of Fig. 9 shows the relationship between $d/u(0.1, 1.3 \text{ GeV})$ and χ_{global}^2 that is quantified this way; and similarly for $g(0.01, 125 \text{ GeV})$.

We can also examine how the χ^2 changes for the individual experiments. Figs. 9 and 10 show the curves for 11 experiments with the largest variations $\max(\chi^2) - \min(\chi^2)$ in the shown ranges of d/u and g , i.e., the most constraining

⁵ With the fully correlated jet energy correction JEC2 source, the data set CMS7jets'14 would provide a strong overall constraint on $s(x, \mu)$ comparable to one of the NuTeV or neutrino CCFR experimental data sets.

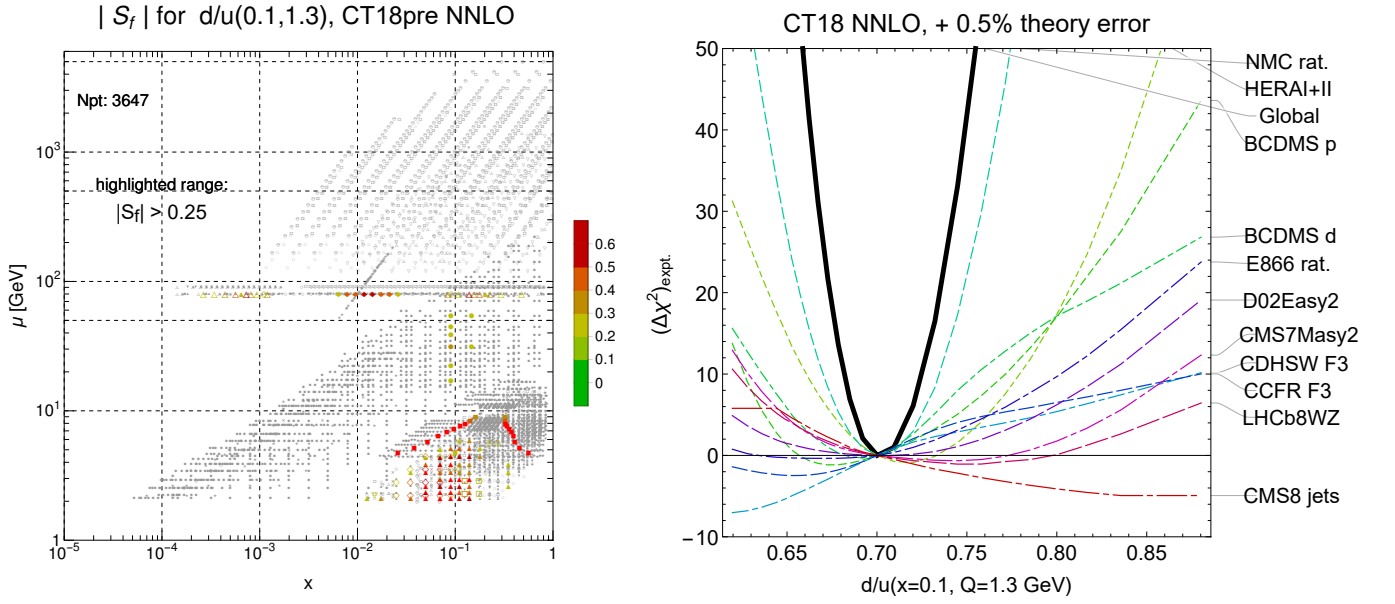


FIG. 9: Left: the PDFSENSE map for the sensitivity of the fitted dataset of the CT18pre NNLO analysis to the d/u PDF ratio, $d/u(x=0.1, \mu=1.3 \text{ GeV})$. Right: Dependence of χ^2 for the individual and all experiments of the CT18pre dataset on the value of $d/u(x=0.1, \mu=1.3 \text{ GeV})$ obtained with the LM scan technique. The curves show the deviations $\Delta\chi^2_{\text{expt.}} \equiv \chi^2_{\text{expt.}}(\bar{a}) - \chi^2_{\text{expt.}}(\bar{a}_0)$ from the best-fit values in χ^2 for the indicated experiments, as well as for the totality of all experiments.

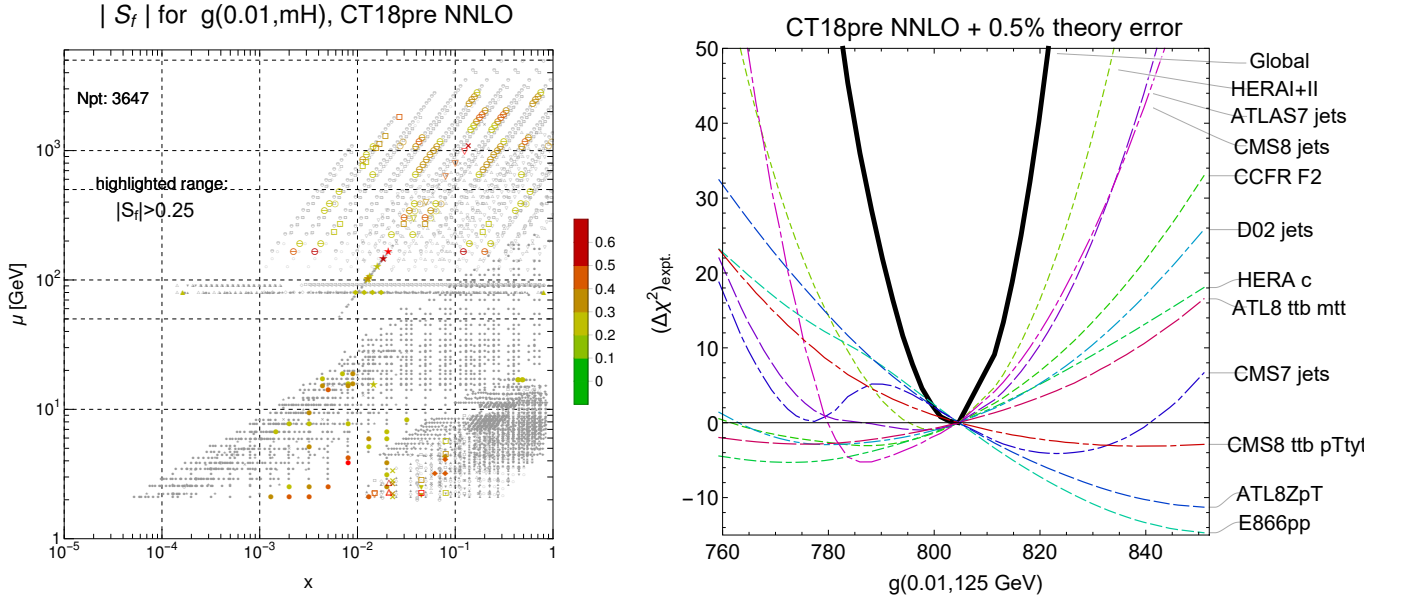


FIG. 10: Like Fig. 9, but comparing the PDFSENSE map (left) and LM scan (right) for the gluon PDF $g(x=0.01, \mu=m_H)$ in the Higgs boson production region.

$d/u(x=0.1, \mu=1.3 \text{ GeV})$			$g(x=0.01, \mu=125 \text{ GeV})$		
PDFSENSE		LM scan	PDFSENSE		LM scan
CT14HERA2	CT18pre	CT18pre	CT14HERA2	CT18pre	CT18pre
HERAI+II'15	NMCrat'97	NMCrat'97	HERAI+II'15	HERAI+II'15	HERAI+II'15
BCDMSp'89	HERAI+II'15	CCFR-F3'97	CMS8jets'17	CMS8jets'17	CMS8jets'17
NMCrat'97	BCDMSp'89	HERAI+II'15	CMS7jets'14	CMS7jets'14	ATL8ZpT'16
CCFR-F3'97	CCFR-F3'97	BCDMSd'90	ATLAS7jets'15	E866pp'03	E866pp'03
E866pp'03	BCDMSd'90	BCDMSp'89	E866pp'03	ATLAS7jets'15	ATLAS7jets'15
BCDMSd'90	E605'91	CDHSW-F3'91	BCDMSd'90	BCDMSd'90	CCFR-F2'01
CDHSW-F3'91	E866pp'03	E866rat'01	CCFR-F3'97	BCDMSp'89	D02jets'08
CMS8jets'17	E866rat'01	CMS7Masy2'14	D02jets'08	D02jets'08	HERAc'13
E866rat'01	CMS8jets'17	NuTeV-nu'06	NMCrat'97	NMCrat'97	NuTeV-nub'06
LHCb8WZ'16	CDHSW-F3'91	CMS8jets'17	BCDMSp'89	CDHSW-F2'91	CCFR-F3'97

TABLE I: We list the top 10 experiments predicted to drive knowledge of the d/u PDF ratio and of the gluon distribution in the Higgs region according to PDFSENSE and LM scans. For both, we list the PDFSENSE evaluations based both on the CT14HERA2 fit and on a preliminary CT18pre fit in the first and second columns on either side of the double-line partition.

experiments. We notice that, while the $\Delta\chi^2$ dependence is nearly Gaussian for the total χ^2 , it is sometimes less so for the individual experiments. Some experiments may be inconsistent when they have a large best-fit $\chi^2(\vec{a}_0)$ or prefer an incompatible X value. Figure 9 is an example of a good agreement between the experiments, when the individual $\Delta\chi_{\text{expt.}}^2$ curves are approximately quadratic and minimized at about the same location. Figure 10 shows more pronounced inconsistencies, notably in the case of the E866pp and ATL8ZpT curves that prefer a significantly larger $g(0.01, 125 \text{ GeV})$ than in the rest of the experiments.

The LM procedure thus allows a systematic exploration of the exact constraints from the experiments on X without relying on the Gaussian assumption that is inherent to the PDFSENSE method. Both PDFSENSE and LM scans successfully identify the experiments with the strongest sensitivity to X , while their specific rankings of such experiments are not strictly identical and reflect the chosen ranking prescription and settings of the global fit. We emphasize that, though informative, the LM scans are computationally intensive, with a typical 30-point scan at NNLO requiring ~ 6500 CPU core-hours on a high-performance cluster. This is in contrast to the PDFSENSE analysis, which can be run for our entire 4021-point dataset on a single CPU core of a modern workstation in ~ 5 minutes, representing a $\sim 0.8 \times 10^5$ savings in computational cost.

Let us further illustrate these observations by referring again to Figs. 9 and 10, as well as to Table I that displays the top 10 experiments with the largest cumulative sensitivity to $d/u(0.1, 1.3 \text{ GeV})$ and $g(0.01, 125 \text{ GeV})$ according to PDFSENSE and LM scans, with either CT14HERA2 or CT18pre PDFs used to construct the PDFSENSE rankings. In the PDFSENSE columns, the experiments are ranked in order of descending cumulative sensitivities $\sum_{i=1}^{N_{pt}} |S_f|(x_i, \mu_i)$ according to the same prescription as in Sec. IV B. For the LM scans, the table shows the experiments that have the largest variations $\max(\chi^2) - \min(\chi^2)$ in the range of X corresponding to $\Delta\chi_{\text{global}}^2 \leq 100$, that is, within approximately the 90% probability level interval of the CT18pre NNLO PDFs. As the residual uncertainties Δr_i in the sensitivities S_f are normalized to the root-mean-squared residuals $\langle r_0 \rangle_E$ at the best fit, cf. Eq. (21), we similarly divide $\max(\chi^2) - \min(\chi^2)$ by the best-fit $\chi^2(\vec{a}_0)/N_{pt}$ of the experiment in the rankings for the LM scans in Table I.

From the side-by-side examination of the figures and the table, we can draw a broad conclusion that both the pre-fit PDFSENSE and post-fit LM scan approaches agree in identifying the most constraining experiments, even though they may result in different orderings of these experiments. This agreement is especially impressive in the instance of $d/u(x=0.1, \mu=1.3 \text{ GeV})$, when the rankings agree on 8 out of 10 leading experiments, confirming the dominance of the NMC p/d ratio, HERAI+II, CCFR F_3 , and BCDMS p and d measurements. For $g(x=0.01, \mu=m_H)$, for which we see more tension and non-Gaussian behavior in Fig. 10, both PDFSENSE and LM scans concur on the crucial role played by the top 5-6 experiments, namely, HERAI+II, E866pp, and inclusive jet production data from CMS, ATLAS, and D0 Run-2. The upward pull on g from the incompatible ATL8ZpT data set seen in Fig. 10 modifies the rankings of the trailing experiments, such as CMS7 jets or BCDMS. Based upon an extended battery of LM scans we have performed, including the two examples presented here, we conclude that the PDFSENSE surveys perform as intended.

Lastly, we reiterate that a number of subtleties exists in comparing the results of LM scans and PDFSENSE sensitivity plots. Most importantly, PDFSENSE is intended by conception as a tool to quantify the anticipated *average* impact of potentially unfitted data based upon their precision in comparison to the PDF uncertainties. We discussed simplifying assumptions made in PDFSENSE in order to bypass certain complexities of the full fit and obtain quick estimates. LM scans, on the other hand, provide post-fit assessments of the contributions of specific data to the global χ^2 function, as specific quantities predicted by the QCD analysis are dialed away from their

optimal values. In the comparisons we made, the detailed pictures produced by both PDFSENSE and the LM scans depend on a variety of theoretical settings like pQCD scale choices, as well as upon the specific implementation of correlated experimental uncertainties [from up to ~ 100 different sources in some experiments] and the parametric forms chosen for the nonperturbative parametrizations at the starting scale $\mu = Q_0$. The inclusion of additional theory uncertainties and decorrelation of some experimental correlated errors are necessitated in a few experiments by the relatively large χ^2 values that would otherwise be obtained. All these have some peripheral effect on the specific orderings of experiments shown in Table I. Thus, rather than anticipating an exact point-to-point matching between the PDFSENSE and LM methods, we instead expect, and indeed find, the general congruity between the most important experiments identified by the two approaches illustrated in this section.

V. CONCLUSIONS

In the foregoing analysis, we have confronted the modern challenge of a rapidly growing set of global QCD data with new statistical methodologies for quantifying and exploring the impact of this information. These novel methodologies are realized in a new analysis tool PDFSENSE [43], which allows the rapid exploration of the impact of both existing and potential data on PDF determinations, thus providing a means of weighing the impact of measurements of QCD processes in a way that allows meaningful conclusions to be drawn without the cost of a full global analysis. We expect this approach to guide future PDF fitting efforts by allowing fitters to examine the world's data *a priori*, so as to concentrate analyses on the highest impact datasets. In particular, this work builds upon the existing CT framework with its reliance on the Hessian formalism and assumed quasi-Gaussianity, but these features do not impact the validity of our analysis and conclusions. Our approach provides a means to carry out a detailed study of data residuals, for which we explored novel visualizations in several ways, including the PCA, t-SNE, and reciprocated distance approaches discussed in Sec. II C. These techniques show promise for moving forward by providing useful insights into the numerical relationships among datasets and experimental processes.

Crucial to this analysis is the leveraging of both the existing and proposed statistical measures laid out in Secs. III A and III B. Of these, the flavor-specific sensitivity S_f of Eq. (21) for a data point to the PDF serves as a particularly powerful discriminator, and we deployed it and the correlation C_f of Eq. (19) to map PDF constraints provided by data over a wide range in $\{x, \mu\}$. This was facilitated by the fact that the sensitivity and correlation are readily computable over the extent of the global dataset. The companion website collects a large number of figures illustrating the sensitivities to various flavors as a function of x and μ .

To quantify the abundant information contained in the maps of sensitivities, in Sec. IV B we presented statistical estimators to systematically rank and assess subsidiary datasets within the world's data according to their potential to be influential in constraining PDFs. We note that one is allowed some freedom in choosing a specific ranking prescription, but we find our conclusions to be stable against variations among these possible choices. In this context, we reaffirmed the unique advantage of DIS and jet production for determination of the PDFs.

Many intriguing physics results can be established using our sensitivity methods, and the specific results in the previous sections are only illustrative examples. We stress that these results take the complementary form of sensitivity tables (for example, Table V) and $\{x, \mu\}$ plots (such as Fig. 2), which respectively offer global categorizations of the experimental landscape and detailed mappings of the placements of PDF constraints in $\{x, \mu\}$ space. In totality, the full range of physics insights from this method is beyond the scope of the present article, but the interested user can explore them using our PDFSENSE package at [43]. We mention only a representative sample of these to motivate the reader:

- A wide range of experimental processes possess sensitivity to the nucleon's quark sea distributions; for example, for the distribution $\bar{d}(x, \mu)$, the σ_{pd} DY measurements of E866 (E866rat'01) exhibit strong sensitivity, but so do DY data from E605 (E605'91) as well as (at larger μ) information on the μ -production asymmetry $A_\mu(\eta)$ from CMS at 7 TeV (CMS7Masy2'14); at high x and μ , CMS inclusive jet data (CMS8jets'17, CMS7jets'14) also acquire some sensitivity to \bar{u} and \bar{d} . Still, however, the recent HERA data (HERAI+II'15) registers the greatest overall sensitivity.
- Were they taken cumulatively together as a single dataset, CMS jet production at 7 and 8 TeV (CMS7jets'14 and CMS8jets'17) would provide a total sensitivity $|S_s^E| = 11.9 + 8.11$ to $s(x, \mu)$ that is comparable to one of the NuTeV (NuTeV-nu'06) or CCFR (CCFR SI nu'01, CCFR SI nub'01) dimuon SIDIS experiments, which have very strong average sensitivity to the strange distribution. Still, the strongest constraint is contributed by a mix of the DIS measurements, including $\nu\mu\mu$ data from NuTeV (NuTeV-nu'06), data on $\nu(\bar{\nu})\mu\mu$ processes from SIDIS at CCFR (CCFR SI nu'01 and CCFR SI nub'01), as well as the inclusive DIS data at lower x from HERA1+2 (HERAI+II'15) that actually has the strongest cumulative sensitivity. Similarly, various vector boson production data sets have a rank-3 point-averaged sensitivity to the strangeness, including the $A_\mu(\eta^\mu)$ data from

D0 (D02Masy'08) and CMS (CMS8Wasy'16, CMS7Masy2'14), as well ATLAS W/Z production (ATL8DY2D'16, ATL7WZ'12) and high- p_T Z production (ATL8ZpT'16) cross sections. Although each of the individual vector boson production data set has a weak cumulative sensitivity to $s(x, \mu)$ because of a small number of data points, in totality a group of *mutually consistent* LHC experiments on vector boson production can provide a competing constraint on $s(x, \mu)$ that confronts the low-energy CCFR/NuTeV constraints.

- Knowledge of the charm distribution $c(x, \mu)$ is most influenced by a number of datasets, with HERA (HERAI+II'15) at low x especially important. Fixed target measurements, particularly those of CDHSW on the proton's F_2^p structure function (CDHSW-F2'91) have strong sensitivity at slightly higher $x \sim 10^{-1}$, while a wide range of jet measurements, including 7 TeV data from ATLAS (ATLAS7jets'15) and CMS (CMS7jets'14), and 8 TeV CMS (CMS8jets'17) points are also sensitive. This pattern of sensitive measurements broadly follows the corresponding plot for $|S_g|(x_i, \mu_i)$ [as well as $|S_b|(x_i, \mu_i)$] due to the dominance of boson fusion graphs in heavy quark production. The datasets of importance we identify are broadly consistent with the conclusions of the recent CT14 analysis [53] of the nucleon's intrinsic charm [36].
- One can also study the correlations and sensitivities for various derived PDF combinations. For instance, for the \bar{d}/\bar{u} ratio representing deviations from flavor symmetry in the nucleon sea, the E866 experiment (E866rat'01) shows exceptional point-averaged sensitivity, $\langle |S_{\bar{d}/\bar{u}}| \rangle = 1.67$ such that its "C" ranking for its overall sensitivity to \bar{d}/\bar{u} places it in the company of only a few other DIS and DY experiments, despite their much larger number of measurements, $N_{pt} = 15$. At somewhat lower $x \gtrsim 0.01$, NMC data on the structure function ratio F_2^d/F_2^p (NMCrat'97) show sensitivity in the range $0.8 < |S_{\bar{d}/\bar{u}}| < 2$. At still lower x , the CMS 8 and 7 TeV A_μ points (CMS8Wasy'16, CMS7Masy2'14) and W/Z data from LHCb (LHCb8WZ'16) show strong pull, corresponding to point-averaged rankings of "2," "1," and "2," respectively.
- We also consider the PDF ratio $d/u(x, \mu)$, which often serves as a discriminant among various nucleon structure models, especially at high x . For $x > 0.1$ an amalgam of fixed-target experiments, including the NMC F_2^d/F_2^p data (NMCrat'97) particularly, but also F_2^p measurements from BCDMS (BCDMSp'89) and CCFR (CCFR-F2'01) as well as xF_3^p data from CCFR drive the current status. At higher μ , however, the LHCb W/Z data (LHCb8WZ'16) and $A_e(\eta)$ measurements from Run-2 of D0 (D02Easy2'15) also constrain the high x behavior of d/u together with $A_\mu(\eta)$ points from CMS at 7 TeV (CMS7Masy2'14).
- More generally, we note that, among the new LHC experiments to be considered for future global fits, the datasets for inclusive jet production are expected to have the greatest impact, followed by a group of vector boson production experiments at ATLAS, CMS, and LHCb. We find that the constraints from jet production at the LHC depend significantly on the treatment of experimental systematic uncertainties — especially the correlated systematic errors. It is conceivable that, with the full implementation of NNLO theoretical cross sections and modest reduction in the experimental systematic uncertainties, the constraints from the LHC jet production will catch up in strength to the effect of adding a large fixed-target DIS dataset, such as BCDMS F_2^p (BCDMSp'89). Meanwhile, the magnitude of the constraint on the gluon PDF from high- p_T Z production (ATL8ZpT'16) is comparable to those from the combined HERA SIDIS charm dataset (HERAc'13) or inclusive jet production from CDF Run-2 (CDF2jets'09); that is, the high- p_T Z data are significant in the event that the jet datasets are not included, in overall consistency with the findings in Ref. [24]. The smaller ATLAS $t\bar{t}$ production data sets (ATL8ttb-pt'16, ATL8ttb-y_ave'16, ATL8ttb-mtt'16, ATL8ttb-y_ttb'16) have strong point-by-point sensitivity to the gluon, but will have a more diminished role when combined with other, larger data sets. HERA DIS (HERAI+II'15), BCDMS F_2^d (BCDMSd'90), and CMS inclusive jets at 8 TeV (CMS8jets'17) render the strongest overall constraints on the Higgs production cross section at the LHC according to the rankings in Table VI.

Quantifying correlations and sensitivities thus provides a comprehensive means of evaluating the ability of a global dataset to constrain our knowledge of nucleon structure. It must be emphasized, however, that this analysis is not a substitute for actually performing a QCD global analysis, which remains the single most robust means of determining the nucleon PDFs themselves. Rather, the method presented in the paper is a guiding tool to both supplement and direct fits by gauging the potential for improving PDFs with the incorporation of new datasets.

The essential ingredients of this study are the PDF-residual correlation and sensitivity $|C_f|$ and $|S_f|$, with the latter representing an extension of the correlation used elsewhere in the modern PDF literature. These definitions are robust enough that we can exhaustively score the data points in an arbitrary global dataset to construct and map the resulting distributions, as shown in Figs. 7 and 8. Accordingly, we found it possible to impose cuts on these distributions to identify points of especially strong correlation ($|C_f| > 0.7$) or sensitivity ($|S_f| > 0.25$); we stress that these cuts are chosen as approximate indicators, and any user can adjust them freely. On the other hand, the distributions themselves, as shown in the second panels of Figs. 7 and 8, are not subject to such cut choices. Although

the conclusions of this analysis are resistant to alterations in the basic approach, it is worth noting that other formats are possible for evaluating experimental sensitivities and performing the rankings of measurements. For example, one might use somewhat different matchings than those outlined in App. A to extract $\{x, \mu\}$ points from the experimental data, but we expect the resulting impact on the overall picture to be minor. Similarly, while the ordering inside ranking tables like Table V was decided according to the total sensitivity to serve our specific goal of identifying the most valuable experiments for the CTEQ-TEA fit, for other purposes one might produce alternative tables ranked according to point-averaged sensitivities, or sensitivities to specific flavors. Such alternate conventions would also yield important information, and PDFSENSE allows the user to do this. It should be stressed that these elections for the form of our presentation can always be recovered from the more fundamental information — the numerical values of the sensitivities detailed in the Supplementary Material of App. C.

While we have demonstrated these techniques in the context of the CT14 family of global fits, they are of sufficient generality that one could readily repeat our analysis using alternative PDF sets. For the sake of testing this point and validating our predictions for the most decisive experiments in the CTEQ-TEA dataset, we performed a preliminary fit including the CT14HERA2 and the candidate LHC experiments (‘CT18pre’), and directly compared PDFSENSE predictions against Lagrange multiplier scans quantifying the constraints these fitted measurements imposed on select quantities. This provided a demonstration of the robustness of our sensitivity-based analysis, which identified the same sets of high-impact measurements *before fitting*. The results of this study can be expected to vary somewhat depending on the specifics of the PDF sets used to compute $|C_f|$ and $|S_f|$, but we see this as an advantage of PDFSENSE. One could imagine exploiting them to undertake a systematic analysis of the impact of various theoretical assumptions implemented in competing global fits (*e.g.*, the choice of input PDF parametrization or the status of the perturbative QCD treatment implemented in various processes). The sensitivity S_f can be constructed either from the Hessian or Monte-Carlo PDF uncertainties, as prescribed by Eqs. (21) and (29), while the shifted residuals that are crucial to our analysis can be recovered from any type of covariance matrix, as argued in relation to Eq. (8). In the same spirit but on the side of the data, PDFSENSE empowers the user to evaluate the combined impact of multiple experimental datasets — for example, to evaluate the extent to which the impact of a proposed experiment might be diminished by the constraints already imposed by existing measurements. These various functions collectively suggest a number of possible avenues to use the presented approach and the PDFSENSE tool to advance PDF knowledge in the coming years.

Acknowledgments

We thank our CTEQ-TEA colleagues, Davison Soper, and Madeline Hamilton for support and insightful discussions, and appreciate helpful clarifications concerning the LHC experimental data sets from Alexander Glazov, Uta Klein, Bogdan Malescu, and Klaus Rabbertz. We also thank German Valencia, Ursula Laa, and Dianne Cook for helpful discussions related to data visualizations based on the PCA and t-SNE methods. This work was supported in part by the U.S. Department of Energy under Grant No. de-sc0010129 and by the National Natural Science Foundation of China under the Grant No. 11465018. T.J. Hobbs acknowledges support from an EIC Center Fellowship. The work of J.G. is sponsored by Shanghai Pujiang Program.

Appendix A: Approximate kinematical variables

In this section, we describe in detail our method for identifying the values of $\{x_i, \mu_i\}$ that correspond to experimental data.

For each experimental data point i , we can establish an approximate relation between the kinematical quantities for that data point, and unobserved quantities specifying the PDFs: the partonic momentum fraction x and QCD factorization scale μ . For example, in DIS, x and μ are approximately equal to Bjorken x_B and momentum transfer Q according to the Born-level kinematic relation. Although this relation is violated by higher-order radiative contributions, it will approximately hold in most scattering events. The same overall logic can be followed to relate the kinematical quantities in every process of the CTEQ-TEA global set to the *approximate* unobserved quantities x and μ in the PDFs. These relations vary by process and are used to assign approximate pairs $\{x_i, \mu_i\}$ for each data point.⁶

⁶ It should be pointed out that, while there are 5227 $\{x, \mu\}$ points generated by the 4021 physical measurements in the default CTEQ-TEA dataset of this study, occasionally there are instances in which $|C_f|$ and $|S_f|$ cannot be meaningfully computed for select flavors. For example, since the bottom quark PDF $b(x, \mu)$ has no sensible definition below its partonic threshold (*i.e.*, for $\mu < m_b = 4.75$ GeV), it

Specifically, for DIS, which primarily measures the differential cross sections of the form $d^2\sigma/(dx_B dQ^2)$, we simply take

$$\mu_i \approx Q|_i, \quad x_i \approx x_B|_i \quad (\text{A1})$$

as mentioned above, where the kinematical variables inside “ $|_i$ ” are evaluated at their experimentally measured values for the i^{th} data point. The above approximate relations hold even when (N)NLO radiative contributions are included.

For one-particle-inclusive particle production in hadron-hadron scattering of the form $AB \rightarrow CX$, we plot two x values if the rapidity y_C is known:

$$\mu_i \approx Q|_i, \quad x_i^\pm \approx \frac{Q}{\sqrt{s}} \exp(\pm y_C)|_i. \quad (\text{A2})$$

We set $y_C = 0$ if the rapidity is integrated away. We point out that for processes of this type, Eq. (A2) implies that a measurement in a single rapidity bin can in fact probe two distinct values of x ; for this and other potential reasons, the number of raw data points in such an experiment (N_{pt}) should not be expected to match the number of extracted $\{x, \mu\}$ points in the figures.

In vector boson production, $AB \rightarrow (\gamma^*, Z \rightarrow \ell\bar{\ell})X$ or $AB \rightarrow (W \rightarrow \ell\nu_\ell)X$, we set $Q = m_{\ell\bar{\ell}}$ (invariant mass of the lepton pair), and $y_C = y_\ell$ if a single-lepton rapidity is provided or $y_C = y_{\ell\bar{\ell}}$ if the lepton-pair rapidity is provided. If the rapidity y_ℓ of the lepton is known, yet $y_{\ell\bar{\ell}}$ of the pair is unknown, we use the fact that $y_\ell \sim y_{\ell\bar{\ell}} \pm 1$ for most events because of the shape of the decay leptonic tensor. Thus, the momentum fractions x_i^\pm can still be estimated as $x_i^\pm \approx (Q/\sqrt{s}) \exp(\pm y)|_i$, where $y \sim y_\ell$ (up to an error of less than 1 unit)

In single-inclusive jet production, $AB \rightarrow j + X$, we set $Q = 2p_{Tj}$, $y_C = y_j$.

In single-inclusive $t\bar{t}$ pair production, $AB \rightarrow t\bar{t}X$, we set $Q = m_{t\bar{t}}$, $y = y_{t\bar{t}}$ if known, or 0 otherwise.

In single-inclusive top (anti-)quark production, $AB \rightarrow (\bar{t})tX$, we take $Q = 2p_{Tt}$, $y = 0$ for $d\sigma/dp_{Tt}$ (as in Expt. ATLAS8ttb-pt'16). On the other hand, for $d\sigma/d\langle y_t \rangle$ or $d\sigma/dy_{t\bar{t}}$, in which the $t\bar{t}$ invariant mass is integrated out (Expts. ATLAS8ttb-y_ave'16 and ATLAS8ttb-y_ttb'16), we take an average mass scale $\mu_i = 400$ GeV that is slightly above the observed peak of $d\sigma/dm_{t\bar{t}}$ at $m_{t\bar{t}} \approx 2m_t$.

Lastly, for the $d\sigma/dp_T^Z$ measurements from $AB \rightarrow (\gamma^*, Z \rightarrow \ell\bar{\ell})X$ in Expts. ATLAS7ZpT'14 and ATLAS8ZpT'16, we take $Q = \sqrt{(p_T^Z)^2 + (M_Z)^2}$, $y_C = y_Z$. [Here Q denotes the boson's transverse mass, not the invariant mass.]

Appendix B: Tabulated results

In Tables II–IV we provide a detailed key for the individual experiments mapped in Fig. 1, including the physical process, number of points, and luminosities, where available. We group these tables broadly according to subprocess — Table II corresponds to DIS experiments, while Tables III and IV collect various measurements for the hadroproduction of, *e.g.*, gauge boson, jet, and $t\bar{t}$ pairs — and thus provide a translation key for the experimental short-hand names given in Fig. 1.

In Tables V and VI, we collect the flavor-specific ($|S_f^E|$) and overall ($\sum_f |S_f^E|$) sensitivities for the experimental datasets contained in this analysis. In Table V we list the total and point-averaged sensitivities for each main flavor ($\bar{d}, \bar{u}, g, u, d, s$), while Table VI gives the corresponding information for a number of quantities derived from these, as explained in the associated captions.

Appendix C: Supplementary Material

As Supplementary Material, we enclose in this Appendix a series of additional tables that further illustrate the details of our sensitivity analysis. These include a detailed breakdown of the various CTEQ-TEA experiments according to physical process (Table VII) and associated sensitivity rankings, both for individual PDF flavors (Table VIII) and for various derived quantities (Table IX). In addition, in Tables X and XI, we give numerical values of sensitivities corresponding to the rankings shown in Tables V and VI. In Tables XII and XIII, numerical values of sensitivities

is not possible to evaluate $|S_b|$ for data points extracted at μ scales below the b -quark mass. Similarly, there are situations when the extracted parton fraction $x_i \approx 1$, such that some PDF flavors $f(x_i, \mu_i) \approx 0$, and the Hessian procedures described in this paper do not yield a well-defined correlation or sensitivity. In these cases, we simply redact the associated $\{x_i, \mu_i\}$ points.

Experiment name	CT ID#	Dataset details	N_{pt}
BCDMSp'89	101	BCDMS F_2^p [54]	337
BCDMSd'90	102	BCDMS F_2^d [55]	250
NMCrat'97	104	NMC F_2^d/F_2^p [56]	123
CDHSW-F2'91	108	CDHSW F_2^p [57]	85
CDHSW-F3'91	109	CDHSW F_3^p [57]	96
CCFR-F2'01	110	CCFR F_2^p [58]	69
CCFR-F3'97	111	CCFR xF_3^p [59]	86
NuTeV-nu'06	124	NuTeV $\nu\mu\mu$ SIDIS [60]	38
NuTeV-nub'06	125	NuTeV $\bar{\nu}\mu\mu$ SIDIS [60]	33
CCFR SI nu'01	126	CCFR $\nu\mu\mu$ SIDIS [61]	40
CCFR SI nub'01	127	CCFR $\bar{\nu}\mu\mu$ SIDIS [61]	38
HERAb'06	145	H1 σ_r^b (57.4 pb $^{-1}$) [62][63]	10
HERAc'13	147	Combined HERA charm production (1.504 fb $^{-1}$) [64]	47
HERAI+II'15	160	HERA1+2 Combined NC and CC DIS (1 fb $^{-1}$) [6]	1120
HERA-FL'11	169	H1 F_L (121.6 pb $^{-1}$) [65]	9

TABLE II: Experimental datasets considered as part of CT14HERA2 and included in this analysis: deep-inelastic scattering. We point out that the numbering scheme (CT ID#) included in this and subsequent tables follows the standard CTEQ labeling system with, *e.g.*, Expt. IDs of the form 1XX representing DIS experiments, *etc.* The HERA combined data set HERAI+II'15 consists of both neutral-current (NC) and charge-current (CC) scattering events.

Experiment name	CT ID#	Dataset details	N_{pt}
E605'91	201	E605 DY [66]	119
E866rat'01	203	E866 DY, $\sigma_{pd}/(2\sigma_{pp})$ [67]	15
E866pp'03	204	E866 DY, $Q^3 d^2\sigma_{pp}/(dQdx_F)$ [68]	184
CDF1Wasy'96	225	CDF Run-1 $A_e(\eta^e)$ (110 pb $^{-1}$) [69]	11
CDF2Wasy'05	227	CDF Run-2 $A_e(\eta^e)$ (170 pb $^{-1}$) [70]	11
D02Masy'08	234	D0 Run-2 $A_\mu(\eta^\mu)$ (0.3 fb $^{-1}$) [71]	9
LHCb7WZ'12	240	LHCb 7 TeV W/Z muon forward- η Xsec (35 pb $^{-1}$) [72]	14
LHCb7Wasy'12	241	LHCb 7 TeV W $A_\mu(\eta^\mu)$ (35 pb $^{-1}$) [72]	5
ZyD02'08	260	D0 Run-2 Z $d\sigma/dy_Z$ (0.4 fb $^{-1}$) [73]	28
ZyCDF2'10	261	CDF Run-2 Z $d\sigma/dy_Z$ (2.1 fb $^{-1}$) [74]	29
CMS7Masy2'14	266	CMS 7 TeV $A_\mu(\eta)$ (4.7 fb $^{-1}$) [75]	11
CMS7Easy'12	267	CMS 7 TeV $A_e(\eta)$ (0.840 fb $^{-1}$) [76]	11
ATL7WZ'12	268	ATLAS 7 TeV W/Z Xsec, $A_\mu(\eta)$ (35 pb $^{-1}$) [77]	41
D02Easy2'15	281	D0 Run-2 $A_e(\eta)$ (9.7 fb $^{-1}$) [78]	13
CDF2jets'09	504	CDF Run-2 incl. jet ($d^2\sigma/dp_T^j dy_j$) (1.13 fb $^{-1}$) [79]	72
D02jets'08	514	D0 Run-2 incl. jet ($d^2\sigma/dp_T^j dy_j$) (0.7 fb $^{-1}$) [80]	110
ATL7jets'12	535	ATLAS 7 TeV incl. jet ($d^2\sigma/dp_T^j dy_j$) (35 pb $^{-1}$) [81]	90
CMS7jets'13	538	CMS 7 TeV incl. jet ($d^2\sigma/dp_T^j dy_j$) (5 fb $^{-1}$) [82]	133

TABLE III: Same as Table II, showing experimental datasets for production of vector bosons, single-inclusive jets, and $t\bar{t}$ pairs.

corresponding to Tables VIII and IX are also given. Lastly, in Tables XIV and XV, sensitivity ranking tables of the CTEQ-TEA dataset based upon a companion fit that excluded jet data are given, and corresponding numerical values are shown in Tables XVI and XVII.

Experiment name	CT ID#	Dataset details	N_{pt}
LHCb7ZWrap'15	245	LHCb 7 TeV Z/W muon forward- η Xsec (1.0 fb^{-1})	[83] 33
LHCb8Zee'15	246	LHCb 8 TeV Z electron forward- η $d\sigma/dy_z$ (2.0 fb^{-1})	[84] 17
ATL7ZpT'14	247	ATLAS 7 TeV $d\sigma/dp_T^Z$ (4.7 fb^{-1})	[85] 8
CMS8Wasy'16	249	CMS 8 TeV W muon, Xsec, $A_\mu(\eta^\mu)$ (18.8 fb^{-1})	[86] 33
LHCb8WZ'16	250	LHCb 8 TeV W/Z muon, Xsec, $A_\mu(\eta^\mu)$ (2.0 fb^{-1})	[87] 42
ATL8DY2D'16	252	ATLAS 8 TeV Z ($d^2\sigma/d y _{udmu}$) (20.3 fb^{-1})	[88] 48
ATL8ZpT'16	253	ATLAS 8 TeV ($d^2\sigma/dp_T^Z dm_{ll}$) (20.3 fb^{-1})	[89] 45
CMS7jets'14	542	CMS 7 TeV incl. jet, R=0.7, ($d^2\sigma/dp_T^j dy_j$) (5 fb^{-1})	[90] 158
ATLAS7jets'15	544	ATLAS 7 TeV incl. jet, R=0.6, ($d^2\sigma/dp_T^j dy_j$) (4.5 fb^{-1})	[91] 140
CMS8jets'17	545	CMS 8 TeV incl. jet, R=0.7, ($d^2\sigma/dp_T^j dy_j$) (19.7 fb^{-1})	[46] 185
ATL8ttb-pt'16	565	ATLAS 8 TeV $t\bar{t} d\sigma/dp_T^t$ (20.3 fb^{-1})	[92] 8
ATL8ttb-y_ave'16	566	ATLAS 8 TeV $t\bar{t} d\sigma/dy_{<t/\bar{t}>}$ (20.3 fb^{-1})	[92] 5
ATL8ttb-mtt'16	567	ATLAS 8 TeV $t\bar{t} d\sigma/dm_{t\bar{t}}$ (20.3 fb^{-1})	[92] 7
ATL8ttb-y_ttb'16	568	ATLAS 8 TeV $t\bar{t} d\sigma/dy_{t\bar{t}}$ (20.3 fb^{-1})	[92] 5

TABLE IV: Same as Table II, showing experimental datasets for production of vector bosons, single-inclusive jets, and $t\bar{t}$ pairs that were not incorporated in the CT14HERA2 fit but included in our augmented CTEQ-TEA set.

No.	Expt.	N_{pt}	Rankings, CT14 HERA2 NNLO PDFs												
			$\sum_f S_f^E $	$\langle \sum_f S_f^E \rangle$	$ S_d^E $	$\langle S_d^E \rangle$	$ S_u^E $	$\langle S_u^E \rangle$	$ S_g^E $	$\langle S_g^E \rangle$	$ S_c^E $	$\langle S_c^E \rangle$	$ S_s^E $	$\langle S_s^E \rangle$	
1	HERAI+IF'15	1120.	620.	0.0922	B		A	3	A	3	A	3	B		C
2	CCFR-F3'97	86	218.	0.423	C	1	C	1	A	3	B	1	C	2	
3	BCDMSp'89	337	184.	0.0908			C		C		B	3	C		
4	NMCrat'97	123	169.	0.229	C	2					C	2	B	2	
5	BCDMSd'90	250	141.	0.0939	C				C	3	C	3	C	3	
6	CDHSW-F3'91	96	115.	0.199	C	2	C	2		3	C	2	C	3	
7	E605'91	119	113.	0.158	C	2	C	2				3			
8	E866pp'03	184	103.	0.0935		3	C	3			C	3			
9	CCFR-F2'01	69	89.1	0.215		3		3	C	2		3		2	3
10	CMS8jets'17	185	87.6	0.0789					C	3					
11	CDHSW-F2'91	85	82.4	0.162		3		3		3		3	C	3	
12	CMS7jets'13	133	63.8	0.0799					C	3					
13	NuTeV-nu'06	38	58.9	0.259		3		3			3		3	C	1
14	CMS7jets'14	158	57.5	0.0606					C	3					
15	CCFR SI nub'01	38	49.4	0.217		3		3			3		3	C	1
16	ATLAS7jets'15	140	48.2	0.0574						3					
17	CCFR SI nu'01	40	48.	0.2		3		3			3		3	C	1
18	LHCb8WZ'16	42	41.4	0.164		3		3		3		3	2		
19	ATL7WZ'12	41	39.6	0.161		3		3			3		3		3
20	CMS8Wasy'16	33	39.2	0.198		2		3			3		2		3
21	D02jets'08	110	37.5	0.0568						3					
22	NuTeV-nub'06	33	36.7	0.185		3		3			3		3		2
23	ATL8DY2D'16	48	34.7	0.121		3		3			3				3
24	E866rat'01	15	33.3	0.37		1		1			3		2		
25	ATL7jets'12	90	30.4	0.0563						3					
26	LHCb7ZWrap'15	33	30.2	0.152		3		3		3		3	3		
27	CMS7Masy2'14	11	29.4	0.446		1		2		2		2	1		3
28	CDF2jets'09	72	21.5	0.0497						3					
29	ATL8ZpT'16	45	17.2	0.0638						3					3
30	HERAc'13	47	15.1	0.0537						3					
31	D02Masy'08	9	15.	0.278		3		3			2		2		2
32	CMS7Easy'12	11	14.3	0.216		2		3		3		3	2		
33	D02Easy2'15	13	14.	0.18		3		3			3		2		
34	ZyD02'08	28	11.6	0.0693							3		3		
35	ZyCDF2'10	29	11.2	0.0647							3				
36	CDF1Wasy'96	11	8.83	0.134		3		3			3		2		
37	LHCb7WZ'12	14	7.27	0.0866		3							3		
38	LHCb8Zee'15	17	7.1	0.0696							3				
39	ATL8ttb-pt'16	8	6.2	0.129		3		3		2					
40	LHCb7Wasy'12	5	6.11	0.204		2		3			3		2		3
41	ATL7ZpT'14	8	5.84	0.122		3		3		3		3	3		
42	HERA-FL'11	9	3.99	0.0739						2					
43	ATL8ttb-mtt'16	7	3.81	0.0907						2					
44	CDF2Wasy'05	11	3.7	0.056									3		
45	ATL8ttb-y_ttb'16	5	3.37	0.112						2					
46	ATL8ttb-y_ave'16	5	3.2	0.107						2					
47	HERAb'06	10	1.14	0.0191											

TABLE V: For each experiment E we have defined its flavor-specific sensitivity $|S_f^E|$ and its point-averaged counterpart $\langle |S_f^E| \rangle$ in Sec. IV B. Using these quantities, we tabulate the total overall (*i.e.*, flavor-summed) sensitivity and a flavor-dependent sensitivity for the various experiments in our dataset, ordering the table in descending magnitude for the overall sensitivity. Thus, row 1 for the combined HERA Run I + Run 2 dataset has the greatest overall sensitivity, while row 47 for the H1 σ_r^b reduced cross section has the least overall sensitivity according to that metric. For each flavor, we award particularly sensitive experiments a rank **A**, **B**, **C** or **1***, **1**, **2**, **3** based on their total and point-averaged sensitivities, respectively. These ranks are decided using the criteria: $C \iff |S_f^E| \in [20, 50]$, $B \iff |S_f^E| \in [50, 100]$, and $A \iff |S_f^E| > 100$ according to the total sensitivities for each flavor; and, analogously, $3 \iff \langle |S_f^E| \rangle \in [0.1, 0.25]$, $2 \iff \langle |S_f^E| \rangle \in [0.25, 0.5]$, $1 \iff \langle |S_f^E| \rangle \in [0.5, 1]$, and $1^* \iff \langle |S_f^E| \rangle > 1$ according to the point-averaged sensitivities. Experiments with sensitivities falling below the lowest ranks (that is, with $|S_f^E| < 20$ or $\langle |S_f^E| \rangle < 0.1$) are not awarded a rank for that category/ flavor. Note that we sum over the light quark + gluon flavors to compute $\langle \sum_f |S_f^E| \rangle$ within this and subsequent tables. Also, new experimental datasets not originally included in CT14HERA2 are indicated by **bold** Expt. names in the second column.

No.	Expt.	Rankings, CT14 HERA2 NNLO PDFs												
		$ S_{u_v}^E $	$\langle S_{u_v}^E \rangle$	$ S_{d_v}^E $	$\langle S_{d_v}^E \rangle$	$ S_{\bar{d}/\bar{u}}^E $	$\langle S_{\bar{d}/\bar{u}}^E \rangle$	$ S_{d/u}^E $	$\langle S_{d/u}^E \rangle$	$ S_{H7}^E $	$\langle S_{H7}^E \rangle$	$ S_{H8}^E $	$\langle S_{H8}^E \rangle$	$ S_{H14}^E $
1	HERAI+II'15	B		C		C		B		B		B		B
2	CCFR-F3'97	B	1	B	1			C	2		3		3	3
3	BCDMSp'89	B	3	C		C		C	3		C			
4	NMCrat'97	C	2	C	3	C	2	B	1					
5	BCDMSd'90	C		C	3			C		C		C		
6	CDHSW-F3'91	C	2	C	2				3					
7	E605'91	C	3	C	3									
8	E866pp'03	C	3											
9	CCFR-F2'01		3		3		3			3		3		3
10	CMS8jets'17									3	C	3	C	3
11	CDHSW-F2'91		3		3			3		3		3		
12	CMS7jets'13									3		3		3
13	NuTeV-nu'06											3		3
14	CMS7jets'14									3		3		3
15	CCFR SI nub'01													
16	ATLAS7jets'15													
17	CCFR SI nu'01													
18	LHCb8WZ'16		3		3		2		2		3		3	
19	ATL7WZ'12		3				3		3					
20	CMS8Wasy'16		3		3		2		2					
21	D02jets'08													
22	NuTeV-nub'06													
23	ATL8DY2D'16		3				3		3					
24	E866rat'01		2		2	C	1*		2		3		3	
25	ATL7jets'12									3		3		3
26	LHCb7ZWrap'15		3		3		2		2		3		3	
27	CMS7Masy2'14		2		2		1		1		3		3	3
28	CDF2jets'09													
29	ATL8ZpT'16													3
30	HERAc'13										3		3	3
31	D02Masy'08		2		2		2		2					3
32	CMS7Easy'12		3		3		2		2					
33	D02Easy2'15		3		2		3		2					
34	ZyD02'08		3											
35	ZyCDF2'10		3											
36	CDF1Wasy'96		3		2		3		2					
37	LHCb7WZ'12						3		3					
38	LHCb8Zee'15													
39	ATL8ttb-pt'16		3								2		2	2
40	LHCb7Wasy'12		3		3		2		2		3		3	3
41	ATL7ZpT'14								3		3		3	3
42	HERA-FL'11										3		3	
43	ATL8ttb-mtt'16										3		3	3
44	CDF2Wasy'05				3				3					
45	ATL8ttb-y_ttb'16										2		2	3
46	ATL8ttb-y_ave'16										2		2	3
47	HERAb'06													

TABLE VI: A horizontal continuation of the information in Table V, containing the flavor-dependent total and mean sensitivities of a number of derived quantities, as opposed to the individual flavors given in Table V. Going across, the total and mean sensitivities are tabulated for valence distributions of the u and d quarks, the partonic flavor ratios \bar{d}/\bar{u} and d/u , and the Higgs production cross section $\sigma_{pp \rightarrow H^0 X}$ at 7, 8, and 14 TeV, respectively. The ranking criteria, ordering, and other conventions are again as described in Table V.

Process	Experiment Names
DIS Old	BCDMSp'89, BCDMSd'90, NMCrat'97, CDHSW-F2'91, CDHSW-F3'91, CCFR-F2'01, CCFR-F3'97, NuTeV-nu'06, NuTeV-nub'06, CCFR SI nu'01, CCFR SI nub'01, HERAb'06, HERAc'13, HERAI+II'15, 169
DISCC Old	CDHSW-F2'91, CDHSW-F3'91, CCFR-F2'01, CCFR-F3'97, NuTeV-nu'06, NuTeV-nub'06, CCFR SI nu'01, CCFR SI nub'01
JP New	CMS7jets'14, ATLAS7jets'15, CMS8jets'17
DISNCCC	HERAI+II'15
VBZ Old	E605'91, E866rat'01, E866pp'03, ZyD02'08, ZyCDF2'10
DISNC Old	BCDMSp'89, BCDMSd'90, NMCrat'97, HERAb'06, HERAc'13, HERA-FL'11
JP Old	CDF2jets'09, D02jets'08, ATL7jets'12, CMS7jets'13
VBPW Old	CDF1Wasy'96, CDF2Wasy'05, D02Masy'08, LHCb7Wasy'12, CMS7Masy2'14, CMS7Easy'12, D02Easy2'15
VBPWZ New	LHCb7ZWrap'15, LHCb8WZ'16
VBZ New	LHCb8Zee'15, ATL8DY2D'16
VBPWZ Old	LHCb7WZ'12, ATL7WZ'12
VBPW New	CMS8Wasy'16
VBZpT	ATL7ZpT'14, ATL8ZpT'16
$t\bar{t}$	ATL8ttb-pt'16, ATL8ttb-y_ave'16, ATL8ttb-mtt'16, ATL8ttb-y_ttb'16

TABLE VII: The experimental IDs of the datasets making up the process types considered in this analysis; we identify these various processes by abbreviated labels: charge current DIS (DISCC), neutral current DIS (DISNC), NC/CC DIS (DISNCCC), and all DIS; Vector Boson Production (VBP) of the W (VBPW), Z (VBZ), and W/Z processes (VBPWZ); $p_T^{W/Z}$ of Z (VBZpT); jet production (JP) and $t\bar{t}$. “Old” sets were in CT14HERA2, but the “New” only in CTEQ-TEA.

No.	Process	N_{pt}	Rankings, CT14 HERA2 NNLO PDFs													
			$\sum_f S_f^E $	$\langle \sum_f S_f^E \rangle$	$ S_d^E $	$\langle S_d^E \rangle$	$ S_u^E $	$\langle S_u^E \rangle$	$ S_g^E $	$\langle S_g^E \rangle$	$ S_u^E $	$\langle S_u^E \rangle$	$ S_d^E $	$\langle S_d^E \rangle$	$ S_s^E $	$\langle S_s^E \rangle$
1	DIS Old	2381.	1.83E3	0.128	A	3										
2	DISCC Old	485	698.	0.24	A	2	A	3	B	3	A	2	A	2	A	3
3	DISNCCC	1120.	620.	0.0922	B		A	3	A	3	A	3	B		C	
4	DISNC Old	776	514.	0.11	B	3	B		B		A	3	A	3	C	
5	VBZ Old	375	272.	0.121	B	3	B	3	C		C	3	C			
6	JP New	483	193.	0.0667	C		C		B	3					C	
7	JP Old	405	153.	0.063			C		B	3					C	
8	VBPW Old	71	91.4	0.215	C	2		3			3	C	2			3
9	VBPWZ New	75	71.6	0.159		3		3		3		3	3			
10	VBPWZ Old	55	46.9	0.142		3		3			3		3			3
11	VBZ New	65	41.8	0.107		3		3			3					3
12	VBPW New	33	39.2	0.198		2		3			3		2			3
13	VBZpT	53	23.1	0.0725						3						3
14	$t\bar{t}$	25	16.6	0.111				3		2						

TABLE VIII: Similar to Table V, yet we tabulate the various types of processes rather than the separate experiments in our global CTEQ-TEA dataset. The process labels are explained in the caption of Table VII, which summarized the constituent experiments contributing to each process type.

		Rankings, CT14 HERA2 NNLO PDFs													
No.	Process	$ S_{u_v}^E $	$\langle S_{u_v}^E \rangle$	$ S_{d_v}^E $	$\langle S_{d_v}^E \rangle$	$ S_{\bar{d}/\bar{u}}^E $	$\langle S_{\bar{d}/\bar{u}}^E \rangle$	$ S_{d/u}^E $	$\langle S_{d/u}^E \rangle$	$ S_{H7}^E $	$\langle S_{H7}^E \rangle$	$ S_{H8}^E $	$\langle S_{H8}^E \rangle$	$ S_{H14}^E $	$\langle S_{H14}^E \rangle$
1	DIS Old	A	3	A	3	A		A	3	A		A		A	
2	DISCC Old	A	2	A	2	C		B	3	B	3	B	3	C	
3	DISNCCC	B		C		C		B		B		B		B	
4	DISNC Old	A	3	B		B	3	A	3	B		B		C	
5	VBZ Old	B	3	B	3	B	3	C							
6	JP New									C		B	3	B	3
7	JP Old									C	3	C	3	C	3
8	VBW Old		3		2	C	2	C	2						
9	VBWZ New		3		3	C	2	C	2		3		3		
10	VBWZ Old		3				3		3						
11	VBZ New								3						
12	VBW New		3		3		2		2						
13	VBZpT														3
14	$t\bar{t}$										2		2		3

TABLE IX: Continuation of Table VIII, listing the PDF combinations and Higgs production cross sections similarly to Table VI of the main paper.

No.	Expt.	N_{pt}	Values, CT14 HERA2 NNLO PDFs													
			$\sum_f S_f^E $	$\langle \sum_f S_f^E \rangle$	$ S_d^E $	$\langle S_d^E \rangle$	$ S_u^E $	$\langle S_u^E \rangle$	$ S_g^E $	$\langle S_g^E \rangle$	$ S_u^E $	$\langle S_u^E \rangle$	$ S_d^E $	$\langle S_d^E \rangle$	$ S_s^E $	$\langle S_s^E \rangle$
1	HERAI+II'15	1120.	620.	0.0922	78.3	0.0699	124.	0.111	143.	0.128	146.	0.13	83.	0.0741	45.	0.0402
2	CCFR-F3'97	86	218.	0.423	46.2	0.537	49.8	0.579	16.8	0.195	63.7	0.741	34.7	0.404	6.85	0.0797
3	BCDMSp'89	337	184.	0.0908	16.6	0.0492	31.1	0.0922	25.8	0.0765	81.2	0.241	20.3	0.0601	8.77	0.026
4	NMCrat'97	123	169.	0.229	44.4	0.361	9.87	0.0802	9.7	0.0789	36.4	0.296	61.4	0.499	7.44	0.0605
5	BCDMSd'90	250	141.	0.0939	24.3	0.0971	17.7	0.0707	26.5	0.106	26.9	0.108	36.2	0.145	9.19	0.0368
6	CDHSW-F3'91	96	115.	0.199	24.2	0.253	25.3	0.264	9.81	0.102	31.6	0.329	20.2	0.21	3.76	0.0392
7	E605'91	119	113.	0.158	42.	0.353	36.9	0.31	5.41	0.0455	13.3	0.112	7.81	0.0656	7.1	0.0596
8	E866pp'03	184	103.	0.0935	19.3	0.105	31.3	0.17	12.8	0.0693	23.2	0.126	9.63	0.0523	6.98	0.0379
9	CCFR-F2'01	69	89.1	0.215	15.2	0.22	9.32	0.135	21.1	0.306	14.6	0.211	19.6	0.284	9.3	0.135
10	CMS8jets'17	185	87.6	0.0789	10.4	0.0564	12.5	0.0676	36.7	0.198	9.08	0.0491	6.9	0.0373	11.9	0.0645
11	CDHSW-F2'91	85	82.4	0.162	11.7	0.138	9.14	0.107	19.8	0.233	15.7	0.185	20.5	0.241	5.55	0.0653
12	CMS7jets'13	133	63.8	0.0799	8.21	0.0617	8.87	0.0667	25.5	0.192	6.75	0.0508	6.23	0.0468	8.18	0.0615
13	NuTeV-nu'06	38	58.9	0.259	7.77	0.204	8.53	0.224	2.57	0.0676	6.41	0.169	8.45	0.222	25.2	0.664
14	CMS7jets'14	158	57.5	0.0606	7.45	0.0472	8.38	0.0531	23.7	0.15	4.76	0.0301	5.	0.0316	8.11	0.0513
15	CCFR SI nub'01	38	49.4	0.217	6.06	0.16	5.82	0.153	2.48	0.0652	6.39	0.168	7.37	0.194	21.3	0.559
16	ATLAS7jets'15	140	48.2	0.0574	6.62	0.0473	6.98	0.0499	19.8	0.141	3.94	0.0281	3.55	0.0253	7.34	0.0524
17	CCFR SI nu'01	40	48.	0.2	6.52	0.163	6.99	0.175	1.87	0.0468	5.33	0.133	6.96	0.174	20.4	0.509
18	LHCb8WZ'16	42	41.4	0.164	10.2	0.244	5.75	0.137	4.58	0.109	7.27	0.173	11.3	0.269	2.32	0.0552
19	ATL7WZ'12	41	39.6	0.161	8.09	0.197	5.14	0.125	3.1	0.0757	5.91	0.144	8.25	0.201	9.13	0.223
20	CMS8Wasy'16	33	39.2	0.198	9.04	0.274	5.08	0.154	3.1	0.0938	5.05	0.153	9.81	0.297	7.09	0.215
21	D02jets'08	110	37.5	0.0568	5.36	0.0487	5.68	0.0517	15.8	0.144	2.91	0.0265	2.33	0.0212	5.4	0.0491
22	NuTeV-nub'06	33	36.7	0.185	3.9	0.118	3.84	0.116	2.62	0.0795	4.75	0.144	5.33	0.161	16.3	0.493
23	ATL8DY2D'16	48	34.7	0.121	5.78	0.12	6.85	0.143	3.23	0.0673	5.8	0.121	4.7	0.098	8.36	0.174
24	E866rat'01	15	33.3	0.37	11.8	0.789	12.1	0.804	0.697	0.0464	3.59	0.239	3.98	0.265	1.16	0.0773
25	ATL7jets'12	90	30.4	0.0563	3.33	0.037	4.24	0.0471	13.	0.144	2.6	0.0289	2.35	0.0261	4.86	0.054
26	LHCb7ZWrap'15	33	30.2	0.152	6.15	0.186	4.71	0.143	3.71	0.112	6.24	0.189	7.02	0.213	2.34	0.0709
27	CMS7Masy2'14	11	29.4	0.446	8.43	0.767	3.24	0.294	2.91	0.265	3.35	0.305	8.86	0.805	2.62	0.238
28	CDF2jets'09	72	21.5	0.0497	2.92	0.0406	2.9	0.0403	9.06	0.126	2.77	0.0384	1.31	0.0182	2.5	0.0347
29	ATL8ZpT'16	45	17.2	0.0638	1.32	0.0293	2.18	0.0485	5.38	0.12	1.66	0.0368	1.29	0.0286	5.4	0.12
30	HERAc'13	47	15.1	0.0537	1.85	0.0393	1.69	0.036	6.53	0.139	1.97	0.0419	1.91	0.0406	1.2	0.0255
31	D02Masy'08	9	15.	0.278	1.85	0.205	2.08	0.231	0.638	0.0709	4.05	0.449	3.86	0.428	2.55	0.284
32	CMS7Easy'12	11	14.3	0.216	4.4	0.4	1.66	0.151	1.25	0.114	1.55	0.141	4.32	0.393	1.1	0.1
33	D02Easy2'15	13	14.	0.18	2.69	0.207	2.69	0.207	0.896	0.0689	2.8	0.215	4.1	0.315	0.865	0.0666
34	ZyD02'08	28	11.6	0.0693	1.69	0.0602	0.881	0.0315	1.49	0.0532	3.49	0.125	2.81	0.1	1.28	0.0457
35	ZyCDF2'10	29	11.2	0.0647	1.75	0.0603	1.07	0.0369	1.36	0.0467	3.15	0.109	2.81	0.0968	1.12	0.0386
36	CDF1Wasy'96	11	8.83	0.134	1.49	0.135	1.2	0.109	0.712	0.0647	1.26	0.115	3.34	0.304	0.828	0.0753
37	LHCb7WZ'12	14	7.27	0.0866	1.49	0.107	1.23	0.0882	0.973	0.0695	1.37	0.0979	1.67	0.119	0.535	0.0382
38	LHCb8Zee'15	17	7.1	0.0696	0.885	0.0521	1.48	0.0869	1.27	0.0747	1.75	0.103	1.23	0.0724	0.483	0.0284
39	ATL8ttb-pt'16	8	6.2	0.129	1.11	0.139	1.41	0.176	2.14	0.268	0.579	0.0724	0.514	0.0643	0.447	0.0559
40	LHCb7Wasy'12	5	6.11	0.204	1.67	0.334	0.856	0.171	0.466	0.0933	0.97	0.194	1.64	0.327	0.51	0.102
41	ATL7ZpT'14	8	5.84	0.122	1.31	0.163	0.939	0.117	1.18	0.148	0.891	0.111	1.24	0.155	0.286	0.0357
42	HERA-FL'11	9	3.99	0.0739	0.238	0.0265	0.364	0.0405	2.3	0.256	0.37	0.0411	0.238	0.0265	0.477	0.053
43	ATL8ttb-mtt'16	7	3.81	0.0907	0.177	0.0253	0.338	0.0482	2.26	0.322	0.408	0.0583	0.46	0.0657	0.167	0.0239
44	CDF2Wasy'05	11	3.7	0.056	0.57	0.0518	0.635	0.0578	0.151	0.0138	0.593	0.0539	1.33	0.121	0.422	0.0384
45	ATL8ttb-y.ttb'16	5	3.37	0.112	0.407	0.0814	0.461	0.0921	1.56	0.311	0.191	0.0382	0.45	0.09	0.308	0.0616
46	ATL8ttb-y.ave'16	5	3.2	0.107	0.273	0.0546	0.339	0.0678	1.57	0.314	0.194	0.0388	0.368	0.0736	0.455	0.0911
47	HERAb'06	10	1.14	0.0191	0.16	0.016	0.107	0.0107	0.463	0.0463	0.121	0.0121	0.165	0.0165	0.128	0.0128

TABLE X: Here we separately collect the numerical values of the total and point-averaged sensitivities used to determine the rankings in Table V of the main paper.

No.	Expt.	Values, CT14 HERA2 NNLO PDFs													
		$ S_{u_v}^E $	$\langle S_{u_v}^E \rangle$	$ S_{d_v}^E $	$\langle S_{d_v}^E \rangle$	$ S_{\bar{d}/\bar{u}}^E $	$\langle S_{\bar{d}/\bar{u}}^E \rangle$	$ S_{d/u}^E $	$\langle S_{d/u}^E \rangle$	$ S_{H7}^E $	$\langle S_{H7}^E \rangle$	$ S_{H8}^E $	$\langle S_{H8}^E \rangle$	$ S_{H14}^E $	$\langle S_{H14}^E \rangle$
1	HERAI+II'15	64.6	0.0577	36.7	0.0328	39.7	0.0354	63.7	0.0569	76.2	0.0681	74.3	0.0663	78.6	0.0701
2	CCFR-F3'97	77.5	0.901	65.4	0.761	5.87	0.0682	25.5	0.297	11.3	0.131	11.8	0.137	13.3	0.154
3	BCDMSp'89	70.8	0.21	21.3	0.0632	20.2	0.0598	40.4	0.12	21.4	0.0634	19.3	0.0573	11.7	0.0349
4	NMCrat'97	34.6	0.281	25.6	0.208	48.7	0.396	76.6	0.623	9.47	0.077	9.94	0.0808	10.5	0.0852
5	BCDMSd'90	20.3	0.0813	27.	0.108	12.6	0.0503	22.5	0.09	23.9	0.0958	23.1	0.0922	18.1	0.0724
6	CDHSW-F3'91	36.7	0.382	32.2	0.336	2.56	0.0266	12.3	0.128	5.45	0.0568	5.48	0.0571	5.88	0.0613
7	E605'91	21.6	0.181	23.7	0.199	11.1	0.0932	3.7	0.0311	1.67	0.014	1.82	0.0153	2.19	0.0184
8	E866pp'03	29.6	0.161	16.2	0.0882	17.7	0.0959	12.4	0.0675	9.6	0.0522	11.	0.0596	13.8	0.0749
9	CCFR-F2'01	10.6	0.154	12.	0.173	9.64	0.14	12.6	0.183	12.2	0.176	11.3	0.164	8.58	0.124
10	CMS8jets'17	11.2	0.0604	6.68	0.0361	6.48	0.035	6.65	0.036	19.3	0.105	20.8	0.112	26.6	0.144
11	CDHSW-F2'91	10.5	0.123	12.6	0.148	4.26	0.0501	12.2	0.143	16.7	0.196	15.	0.177	8.48	0.0998
12	CMS7jets'13	6.	0.0451	4.92	0.037	4.14	0.0311	3.66	0.0275	18.	0.135	18.3	0.137	18.9	0.142
13	NuTeV-nu'06	0.959	0.0252	1.12	0.0294	2.23	0.0587	3.68	0.0968	2.32	0.061	1.99	0.0524	1.8	0.0473
14	CMS7jets'14	4.56	0.0289	4.02	0.0254	4.64	0.0293	3.33	0.0211	18.5	0.117	18.3	0.116	17.2	0.109
15	CCFR SI nub'01	2.39	0.0629	1.92	0.0506	1.25	0.033	3.19	0.0839	3.3	0.0868	3.14	0.0827	2.69	0.0707
16	ATLAS7jets'15	4.17	0.0298	3.69	0.0263	3.55	0.0254	2.48	0.0177	10.1	0.072	11.	0.0787	13.4	0.0958
17	CCFR SI nu'01	0.594	0.0148	0.829	0.0207	1.3	0.0325	2.52	0.0629	1.37	0.0343	1.19	0.0297	1.34	0.0335
18	LHCb8WZ'16	6.35	0.151	5.98	0.142	12.7	0.303	13.2	0.313	4.53	0.108	4.37	0.104	3.62	0.0861
19	ATL7WZ'12	6.52	0.159	3.95	0.0963	9.07	0.221	8.54	0.208	1.83	0.0446	1.47	0.0358	1.29	0.0314
20	CMS8Wasy'16	6.84	0.207	4.5	0.136	10.4	0.315	9.68	0.293	1.58	0.0478	1.18	0.0357	1.73	0.0523
21	D02jets'08	2.51	0.0228	1.74	0.0158	2.91	0.0265	1.88	0.0171	8.03	0.073	8.39	0.0763	8.96	0.0814
22	NuTeV-nub'06	2.39	0.0723	2.1	0.0637	1.41	0.0427	2.93	0.0888	3.05	0.0925	2.85	0.0865	2.68	0.0811
23	ATL8DY2D'16	5.14	0.107	2.18	0.0455	5.56	0.116	6.07	0.126	4.13	0.086	3.93	0.0819	3.35	0.0699
24	E866rat'01	7.03	0.469	6.41	0.427	25.	1.67	4.78	0.319	2.01	0.134	1.83	0.122	1.17	0.0782
25	ATL7jets'12	2.65	0.0295	1.59	0.0177	1.77	0.0196	1.71	0.019	9.5	0.106	9.56	0.106	9.63	0.107
26	LHCb7ZWrap'15	4.95	0.15	4.73	0.143	8.36	0.253	8.55	0.259	4.34	0.131	4.11	0.125	2.96	0.0898
27	CMS7Masy2'14	5.21	0.474	2.88	0.262	9.87	0.897	10.8	0.981	1.59	0.144	1.63	0.148	2.15	0.196
28	CDF2jets'09	2.52	0.035	1.19	0.0165	1.95	0.027	1.43	0.0198	5.11	0.0709	4.72	0.0655	3.87	0.0538
29	ATL8ZpT'16	1.53	0.0339	0.86	0.0191	2.29	0.0508	1.63	0.0363	2.1	0.0468	2.09	0.0464	5.18	0.115
30	HERAc'13	0.985	0.021	0.619	0.0132	0.752	0.016	0.937	0.0199	5.52	0.117	5.42	0.115	4.81	0.102
31	D02Masy'08	3.85	0.428	4.14	0.46	2.7	0.3	3.78	0.42	0.512	0.0569	0.633	0.0704	0.986	0.11
32	CMS7Easy'12	2.24	0.203	1.21	0.11	5.18	0.471	5.23	0.475	0.958	0.0871	1.01	0.0918	1.05	0.0954
33	D02Easy2'15	3.02	0.232	4.47	0.343	2.51	0.193	4.77	0.367	0.378	0.0291	0.438	0.0337	0.545	0.0419
34	ZyD02'08	3.45	0.123	2.06	0.0735	1.6	0.057	1.74	0.0623	1.22	0.0436	0.971	0.0347	0.518	0.0185
35	ZyCDF2'10	3.08	0.106	2.42	0.0836	1.71	0.0591	2.26	0.0779	1.12	0.0386	0.887	0.0306	0.739	0.0255
36	CDF1Wasy'96	1.2	0.109	3.5	0.318	1.64	0.149	3.78	0.343	0.357	0.0325	0.442	0.0402	0.66	0.06
37	LHCb7WZ'12	0.871	0.0622	1.01	0.0725	1.54	0.11	1.7	0.121	1.07	0.0765	0.961	0.0686	0.572	0.0409
38	LHCb8Zee'15	0.537	0.0316	0.64	0.0377	0.704	0.0414	1.05	0.0617	0.714	0.042	0.579	0.0341	0.37	0.0218
39	ATL8ttb-pt'16	0.893	0.112	0.589	0.0737	0.234	0.0292	0.536	0.067	2.4	0.3	2.56	0.32	2.68	0.335
40	LHCb7Wasy'12	0.942	0.188	0.886	0.177	1.97	0.393	1.98	0.395	0.675	0.135	0.677	0.135	0.554	0.111
41	ATL7ZpT'14	0.0843	0.0105	0.189	0.0237	0.718	0.0898	0.809	0.101	1.63	0.203	1.56	0.195	1.35	0.169
42	HERA-FL'11	0.0644	0.00716	0.0624	0.00693	0.0874	0.00971	0.0828	0.0092	1.15	0.128	1.03	0.114	0.422	0.0469
43	ATL8ttb-mtt'16	0.402	0.0575	0.42	0.06	0.179	0.0256	0.259	0.037	1.08	0.154	1.05	0.15	1.22	0.174
44	CDF2Wasy'05	0.529	0.0481	1.35	0.123	0.67	0.0609	1.57	0.143	0.0668	0.00608	0.0794	0.00722	0.11	0.00998
45	ATL8ttb-y_ttb'16	0.13	0.0259	0.0977	0.0195	0.166	0.0333	0.293	0.0585	1.49	0.298	1.46	0.291	1.11	0.222
46	ATL8ttb-y_ave'16	0.121	0.0242	0.193	0.0386	0.177	0.0354	0.222	0.0444	1.31	0.262	1.34	0.268	1.21	0.243
47	HERAb'06	0.0873	0.00873	0.0543	0.00543	0.0927	0.00927	0.105	0.0105	0.491	0.0491	0.465	0.0465	0.349	0.0349

TABLE XI: Sensitivity values for Table VI of the main paper.

No.	Process	N_{pt}	Values, CT14 HERA2 NNLO PDFs													
			$\sum_f S_f^E $	$\langle \sum_f S_f^E \rangle$	$ S_d^E $	$\langle S_d^E \rangle$	$ S_u^E $	$\langle S_u^E \rangle$	$ S_g^E $	$\langle S_g^E \rangle$	$ S_u^E $	$\langle S_u^E \rangle$	$ S_d^E $	$\langle S_d^E \rangle$	$ S_s^E $	$\langle S_s^E \rangle$
1	DIS Old	2381.	1.83E3	0.128	287.	0.121	304.	0.128	292.	0.122	441.	0.185	326.	0.137	181.	0.0759
2	DISCC Old	485	698.	0.24	122.	0.251	119.	0.245	77.	0.159	148.	0.306	123.	0.254	109.	0.224
3	DISNCCC	1120.	620.	0.0922	78.3	0.0699	124.	0.111	143.	0.128	146.	0.13	83.	0.0741	45.	0.0402
4	DISNC Old	776	514.	0.11	87.5	0.113	60.8	0.0783	71.3	0.0919	147.	0.189	120.	0.155	27.2	0.0351
5	VBPZ Old	375	272.	0.121	76.6	0.204	82.2	0.219	21.7	0.0579	46.7	0.125	27.	0.0721	17.6	0.047
6	JP New	483	193.	0.0667	24.5	0.0508	27.9	0.0577	80.3	0.166	17.8	0.0368	15.4	0.032	27.4	0.0567
7	JP Old	405	153.	0.063	19.8	0.0489	21.7	0.0536	63.4	0.157	15.	0.0371	12.2	0.0302	20.9	0.0517
8	VBPW Old	71	91.4	0.215	21.1	0.297	12.4	0.174	7.03	0.099	14.6	0.205	27.4	0.386	8.89	0.125
9	VBPWZ New	75	71.6	0.159	16.4	0.218	10.5	0.14	8.29	0.111	13.5	0.18	18.3	0.244	4.66	0.0621
10	VBPWZ Old	55	46.9	0.142	9.59	0.174	6.38	0.116	4.08	0.0741	7.29	0.132	9.91	0.18	9.67	0.176
11	VBPZ New	65	41.8	0.107	6.67	0.103	8.33	0.128	4.5	0.0692	7.55	0.116	5.94	0.0913	8.84	0.136
12	VBPW New	33	39.2	0.198	9.04	0.274	5.08	0.154	3.1	0.0938	5.05	0.153	9.81	0.297	7.09	0.215
13	VBPZpT	53	23.1	0.0725	2.63	0.0496	3.12	0.0589	6.56	0.124	2.55	0.0481	2.52	0.0476	5.68	0.107
14	$t\bar{t}$	25	16.6	0.111	1.97	0.0787	2.55	0.102	7.52	0.301	1.37	0.0549	1.79	0.0717	1.38	0.0551

TABLE XII: Sensitivity values for Table VIII.

No.	Process	Values, CT14 HERA2 NNLO PDFs													
		$ S_{u_v}^E $	$\langle S_{u_v}^E \rangle$	$ S_{d_v}^E $	$\langle S_{d_v}^E \rangle$	$ S_{d/\bar{u}}^E $	$\langle S_{d/\bar{u}}^E \rangle$	$ S_{d/u}^E $	$\langle S_{d/u}^E \rangle$	$ S_{H7}^E $	$\langle S_{H7}^E \rangle$	$ S_{H8}^E $	$\langle S_{H8}^E \rangle$	$ S_{H14}^E $	$\langle S_{H14}^E \rangle$
1	DIS Old	333.	0.14	240.	0.101	151.	0.0632	279.	0.117	194.	0.0814	186.	0.0782	169.	0.0711
2	DISCC Old	142.	0.292	128.	0.264	28.5	0.0588	74.9	0.154	55.6	0.115	52.7	0.109	44.7	0.0922
3	DISNCCC	64.6	0.0577	36.7	0.0328	39.7	0.0354	63.7	0.0569	76.2	0.0681	74.3	0.0663	78.6	0.0701
4	DISNC Old	127.	0.163	74.6	0.0961	82.4	0.106	141.	0.181	61.9	0.0798	59.2	0.0763	45.9	0.0592
5	VBPZ Old	64.7	0.173	50.8	0.135	57.1	0.152	24.9	0.0664	15.6	0.0417	16.5	0.0439	18.4	0.0491
6	JP New	19.9	0.0412	14.4	0.0298	14.7	0.0304	12.5	0.0258	47.9	0.0991	50.1	0.104	57.2	0.118
7	JP Old	13.7	0.0338	9.45	0.0233	10.8	0.0266	8.68	0.0214	40.6	0.1	40.9	0.101	41.3	0.102
8	VBPW Old	17.	0.239	18.4	0.26	24.5	0.346	31.9	0.449	4.53	0.0639	4.91	0.0691	6.06	0.0853
9	VBPWZ New	11.3	0.151	10.7	0.143	21.1	0.281	21.7	0.289	8.86	0.118	8.49	0.113	6.58	0.0877
10	VBPWZ Old	7.39	0.134	4.96	0.0902	10.6	0.193	10.2	0.186	2.9	0.0527	2.43	0.0441	1.86	0.0338
11	VBPZ New	5.67	0.0873	2.82	0.0434	6.27	0.0964	7.12	0.109	4.84	0.0745	4.51	0.0694	3.72	0.0573
12	VBPW New	6.84	0.207	4.5	0.136	10.4	0.315	9.68	0.293	1.58	0.0478	1.18	0.0357	1.73	0.0523
13	VBPZpT	1.61	0.0304	1.05	0.0198	3.	0.0567	2.44	0.0461	3.73	0.0704	3.65	0.0689	6.53	0.123
14	$t\bar{t}$	1.55	0.0618	1.3	0.052	0.756	0.0302	1.31	0.0524	6.28	0.251	6.4	0.256	6.22	0.249

TABLE XIII: Sensitivity values for Table IX.

No.	Expt.	N_{pt}	Rankings, CT14 HERA2 NNLO PDFs fitted without jet data													
			$\sum_f S_f^E $	$\langle \sum_f S_f^E \rangle$	$ S_d^E $	$\langle S_d^E \rangle$	$ S_u^E $	$\langle S_u^E \rangle$	$ S_g^E $	$\langle S_g^E \rangle$	$ S_u^E $	$\langle S_u^E \rangle$	$ S_d^E $	$\langle S_d^E \rangle$	$ S_s^E $	$\langle S_s^E \rangle$
1	HERAI+IP'15	1120.	599.	0.0892	B		A	3	A	3	A	3	B		B	
2	BCDMSp'89	337	230.	0.114	C		C	3	C	3	B	3	C		C	
3	CCFR-F3'97	86	223.	0.433	B	1	B	1		3	B	1	C	2		3
4	CMS8jets'17	185	205.	0.185	C	3	C	3	B	2					C	3
5	NMCrat'97	123	168.	0.228	C	2	C	3			C	2	B	2		
6	BCDMSd'90	250	160.	0.107	C	3	C	3	C	3	C	3	C	3		
7	CMS7jets'13	133	131.	0.165	C	3	C	3	B	2						3
8	CMS7jets'14	158	126.	0.133	C	3	C	3	C	2						3
9	CDHSW-F3'91	96	117.	0.203	C	2	C	2		3	C	2		3		
10	E605'91	119	112.	0.157	C	2	C	2				3				
11	ATLAS7jets'15	140	109.	0.129		3	C	3	C	2						3
12	E866pp'03	184	107.	0.0966		3	C	3			C	3				
13	CCFR-F2'01	69	103.	0.248		2		3	C	2		3		2		3
14	CDHSW-F2'91	85	90.6	0.178		3		3		3		3	C	3		3
15	D02jets'08	110	90.4	0.137		3		3	C	2						3
16	NuTeV-nu'06	38	67.2	0.295		3		2		3		3		2	C	1
17	CDF2jets'09	72	61.9	0.143		3		3	C	2						3
18	ATL7jets'12	90	61.2	0.113		3		3	C	2						3
19	CCFR SI nu'01	40	54.7	0.228		3		3				3		3	C	1
20	CCFR SI nub'01	38	54.2	0.238		3		3				3		3	C	1
21	ATL8DY2D'16	48	40.9	0.142		3		3		3		3		3		3
22	NuTeV-nub'06	33	40.3	0.204		3		3		3		3		3		1
23	ATL7WZ'12	41	39.3	0.16		3		3				3		3		3
24	LHCb8WZ'16	42	38.8	0.154		3		3				3		2		
25	CMS8Wasy'16	33	36.9	0.187		2		3				3		2		3
26	E866rat'01	15	34.9	0.388		1		1		3		3		2		3
27	CMS7Masy2'14	11	30.1	0.457		1		2		3		2		1		3
28	LHCb7ZWrap'15	33	27.9	0.141		3		3		3		3		3		
29	ATL8ZpT'16	45	23.4	0.0865						3						3
30	HERAc'13	47	17.3	0.0614						3						
31	D02Masy'08	9	14.5	0.269		2		3		2		2		2		3
32	CMS7Easy'12	11	13.9	0.211		2		3				3		2		
33	ZyD02'08	28	13.3	0.0792								3		3		
34	ZyCDF2'10	29	12.6	0.0722										3		
35	D02Easy2'15	13	12.3	0.158		3		3				3		2		
36	CDF1Wasy'96	11	7.39	0.112		3						3		3		
37	LHCb7WZ'12	14	7.27	0.0865		3								3		
38	ATL8ttb-pt'16	8	6.91	0.144		3		3		2						
39	LHCb8Zee'15	17	6.31	0.0619												
40	ATL8ttb-mtt'16	7	5.94	0.141				3		2						
41	ATL7ZpT'14	8	5.73	0.119		3		3		3		3		3		
42	LHCb7Wasy'12	5	5.4	0.18		2		3				3		2		
43	ATL8ttb-y_ave'16	5	4.95	0.165		3		3		2						3
44	ATL8ttb-y_ttb'16	5	4.35	0.145		3		3		2						
45	CDF2Wasy'05	11	3.57	0.0541												
46	HERA-FL'11	9	1.82	0.0337						3						
47	HERAb'06	10	1.47	0.0244												

TABLE XIV: Experiment rankings as in Table V of the main paper, for the PDFs obtained using the CT14HERA2 NNLO data sets (Tables II, III of the main paper), with the exclusion of Tevatron and LHC jet production experiments. The **bold** font indicates those experiments which were *not* fitted as constraints leading to the PDF parametrization *CT14 HERA2 NNLO PDFs fitted without jet data* used to evaluate the sensitivities in this table.

No.	Expt.	Rankings, CT14 HERA2 NNLO PDFs fitted without jet data												
		$ S_{u_v}^E $	$\langle S_{u_v}^E \rangle$	$ S_{d_v}^E $	$\langle S_{d_v}^E \rangle$	$ S_{\bar{d}/\bar{u}}^E $	$\langle S_{\bar{d}/\bar{u}}^E \rangle$	$ S_{d/u}^E $	$\langle S_{d/u}^E \rangle$	$ S_{H7}^E $	$\langle S_{H7}^E \rangle$	$ S_{H8}^E $	$\langle S_{H8}^E \rangle$	$ S_{H14}^E $
1	HERAI+II'15	B		C		C		B		B		B		A
2	BCDMSp'89	B	3	C		C		C	3	C		C		C
3	CCFR-F3'97	B	1	B	1		3	C	2		3		3	3
4	CMS8jets'17						3			C	3		C	3
5	NMCrat'97	C	2	C	3	C	2	B	1					
6	BCDMSd'90			C	3			C		C	3		C	3
7	CMS7jets'13									C	2		C	2
8	CMS7jets'14									C	2		C	3
9	CDHSW-F3'91	C	2	C	2				3					
10	E605'91		3	C	3		3							
11	ATLAS7jets'15									C	3		C	3
12	E866pp'03	C	3										C	3
13	CCFR-F2'01		3		3		3		3		2		3	3
14	CDHSW-F2'91		3		3		3		3		3		3	3
15	D02jets'08										3		3	3
16	NuTeV-nu'06						3		3		3		3	3
17	CDF2jets'09										3		3	3
18	ATL7jets'12										3		3	3
19	CCFR SI nu'01						3				3		3	3
20	CCFR SI nub'01										3		3	3
21	ATL8DY2D'16		3				3		3					
22	NuTeV-nub'06													
23	ATL7WZ'12		3		3		3		3		3		3	3
24	LHCb8WZ'16		3		3		2		2					
25	CMS8Wasy'16		3		3		2		2					
26	E866rat'01		2		2	C	1*		2		3		3	3
27	CMS7Masy2'14		2		2		1*		1*					
28	LHCb7ZWrap'15		3		3		3		2		3			
29	ATL8ZpT'16										3		3	3
30	HERAc'13										3		3	3
31	D02Masy'08		2		2		2		2		2		2	2
32	CMS7Easy'12		3		3		2		2					
33	ZyD02'08													
34	ZyCDF2'10													
35	D02Easy2'15		3		2				2					
36	CDF1Wasy'96		3		3		3		2					
37	LHCb7WZ'12								3					
38	ATL8ttb-pt'16		3		3						1		1	1
39	LHCb8Zee'15													
40	ATL8ttb-mtt'16				3						2		2	2
41	ATL7ZpT'14										3		3	3
42	LHCb7Wasy'12		3		3		2		2		3		3	3
43	ATL8ttb-y_ave'16				3						2		2	2
44	ATL8ttb-y_ttb'16										2		2	2
45	CDF2Wasy'05								3					
46	HERA-FL'11													
47	HERAb'06													

TABLE XV: Continuation of Table XIV for the PDFs obtained without imposing constraints from jet production experiments. The PDF combinations and Higgs production cross sections are the same as in Table VI of the main paper.

No.	Expt.	N_{pt}	Values, CT14 HERA2 NNLO PDFs fitted without jet data													
			$\sum_f S_f^E $	$\langle \sum_f S_f^E \rangle$	$ S_d^E $	$\langle S_d^E \rangle$	$ S_u^E $	$\langle S_u^E \rangle$	$ S_g^E $	$\langle S_g^E \rangle$	$ S_u^E $	$\langle S_u^E \rangle$	$ S_d^E $	$\langle S_d^E \rangle$	$ S_s^E $	$\langle S_s^E \rangle$
1	HERAI+IF'15	1120.	599.	0.0892	73.8	0.0659	122.	0.109	143.	0.128	136.	0.121	73.8	0.0659	51.1	0.0457
2	BCDMSp'89	337	230.	0.114	25.	0.0742	38.8	0.115	45.6	0.135	76.9	0.228	22.3	0.0662	21.	0.0622
3	CCFR-F3'97	86	223.	0.433	50.8	0.591	51.3	0.597	19.5	0.227	61.3	0.713	30.2	0.352	10.1	0.117
4	CMS8jets'17	185	205.	0.185	30.2	0.163	39.1	0.211	72.3	0.391	15.2	0.0824	14.5	0.0784	33.6	0.181
5	NMCrat'97	123	168.	0.228	45.7	0.371	12.9	0.105	6.69	0.0544	37.8	0.308	58.6	0.476	6.77	0.0551
6	BCDMSd'90	250	160.	0.107	28.7	0.115	23.5	0.0942	33.1	0.132	25.2	0.101	35.1	0.14	14.7	0.059
7	CMS7jets'13	133	131.	0.165	20.1	0.151	24.1	0.181	51.1	0.384	8.87	0.0667	7.44	0.0559	19.8	0.149
8	CMS7jets'14	158	126.	0.133	20.	0.127	23.6	0.149	46.	0.291	9.59	0.0607	8.09	0.0512	19.2	0.121
9	CDHSW-F3'91	96	117.	0.203	26.	0.271	25.5	0.266	10.9	0.114	30.	0.312	18.5	0.192	5.94	0.0619
10	E605'91	119	112.	0.157	42.5	0.357	30.1	0.253	9.58	0.0805	12.6	0.106	9.99	0.084	7.22	0.0607
11	ATLAS7jets'15	140	109.	0.129	17.5	0.125	20.1	0.144	37.8	0.27	8.94	0.0638	6.93	0.0495	17.5	0.125
12	E866pp'03	184	107.	0.0966	19.	0.103	30.	0.163	16.8	0.0911	21.3	0.116	12.	0.065	7.72	0.042
13	CCFR-F2'01	69	103.	0.248	17.8	0.258	14.2	0.205	24.5	0.355	15.	0.218	19.2	0.279	11.9	0.172
14	CDHSW-F2'91	85	90.6	0.178	13.3	0.157	11.6	0.137	18.7	0.22	16.1	0.19	20.6	0.243	10.2	0.12
15	D02jets'08	110	90.4	0.137	14.8	0.135	17.7	0.161	31.2	0.284	6.96	0.0633	5.15	0.0468	14.5	0.132
16	NuTeV-nu'06	38	67.2	0.295	8.5	0.224	10.1	0.266	3.81	0.1	7.18	0.189	10.4	0.274	27.2	0.716
17	CDF2jets'09	72	61.9	0.143	9.85	0.137	12.1	0.168	21.	0.292	4.58	0.0636	3.44	0.0478	10.9	0.151
18	ATL7jets'12	90	61.2	0.113	9.07	0.101	11.4	0.127	23.9	0.266	3.92	0.0435	2.88	0.032	9.97	0.111
19	CCFR SI nu'01	40	54.7	0.228	6.92	0.173	8.46	0.212	2.44	0.061	6.19	0.155	8.11	0.203	22.5	0.564
20	CCFR SI nub'01	38	54.2	0.238	6.03	0.159	6.58	0.173	3.34	0.0878	6.79	0.179	6.55	0.172	24.9	0.656
21	ATL8DY2D'16	48	40.9	0.142	6.66	0.139	7.92	0.165	5.96	0.124	6.	0.125	5.4	0.113	9.	0.188
22	NuTeV-nub'06	33	40.3	0.204	4.72	0.143	3.58	0.109	3.54	0.107	4.55	0.138	5.43	0.165	18.5	0.561
23	ATL7WZ'12	41	39.3	0.16	8.88	0.216	5.28	0.129	3.67	0.0895	4.6	0.112	9.14	0.223	7.78	0.19
24	LHCb8WZ'16	42	38.8	0.154	9.68	0.23	5.78	0.138	3.92	0.0932	6.03	0.144	10.8	0.258	2.57	0.0613
25	CMS8Wasy'16	33	36.9	0.187	9.62	0.292	5.5	0.167	2.05	0.062	3.92	0.119	9.97	0.302	5.87	0.178
26	E866rat'01	15	34.9	0.388	11.4	0.759	11.2	0.744	2.52	0.168	3.29	0.219	3.92	0.262	2.63	0.175
27	CMS7Masy2'14	11	30.1	0.457	8.91	0.81	5.23	0.475	1.13	0.102	4.71	0.428	8.39	0.762	1.79	0.163
28	LHCb7ZWrap'15	33	27.9	0.141	5.61	0.17	4.55	0.138	3.68	0.112	4.68	0.142	6.95	0.211	2.47	0.0749
29	ATL8ZpT'16	45	23.4	0.0865	1.58	0.0351	2.8	0.0622	9.71	0.216	1.99	0.0442	1.84	0.0409	5.45	0.121
30	HERAc'13	47	17.3	0.0614	2.2	0.0468	2.15	0.0457	7.33	0.156	2.41	0.0512	2.28	0.0484	0.955	0.0203
31	D02Masy'08	9	14.5	0.269	2.33	0.259	1.29	0.143	2.92	0.324	3.77	0.418	2.94	0.327	1.3	0.144
32	CMS7Easy'12	11	13.9	0.211	4.24	0.385	2.6	0.236	0.416	0.0378	2.18	0.198	3.76	0.341	0.747	0.0679
33	ZyD02'08	28	13.3	0.0792	2.18	0.0777	1.16	0.0414	1.54	0.055	2.99	0.107	3.42	0.122	2.03	0.0725
34	ZyCDF2'10	29	12.6	0.0722	1.96	0.0677	1.13	0.039	1.49	0.0514	2.73	0.0942	3.15	0.109	2.1	0.0723
35	D02Easy2'15	13	12.3	0.158	2.32	0.178	1.86	0.143	1.17	0.0896	2.19	0.168	3.83	0.295	0.979	0.0753
36	CDF1Wasy'96	11	7.39	0.112	1.37	0.125	0.752	0.0684	0.82	0.0745	1.23	0.112	2.75	0.25	0.461	0.042
37	LHCb7WZ'12	14	7.27	0.0865	1.45	0.104	1.29	0.092	1.03	0.0736	1.15	0.0824	1.72	0.123	0.629	0.0449
38	ATL8ttb-pt'16	8	6.91	0.144	1.48	0.185	1.71	0.213	2.78	0.347	0.271	0.0339	0.255	0.0319	0.423	0.0529
39	LHCb8Zee'15	17	6.31	0.0619	0.897	0.0528	1.26	0.0743	1.3	0.0765	0.948	0.0558	1.13	0.0665	0.772	0.0454
40	ATL8ttb-mtt'16	7	5.94	0.141	0.599	0.0856	0.86	0.123	3.32	0.474	0.345	0.0492	0.382	0.0546	0.433	0.0618
41	ATL7ZpT'14	8	5.73	0.119	1.1	0.138	0.989	0.124	1.46	0.183	0.809	0.101	1.06	0.132	0.315	0.0394
42	LHCb7Wasy'12	5	5.4	0.18	1.45	0.291	0.892	0.178	0.269	0.0537	0.866	0.173	1.55	0.31	0.37	0.074
43	ATL8ttb-y_ave'16	5	4.95	0.165	0.617	0.123	0.887	0.177	2.23	0.446	0.399	0.0799	0.28	0.0559	0.538	0.108
44	ATL8ttb-y_ttb'16	5	4.35	0.145	0.623	0.125	0.716	0.143	2.01	0.403	0.355	0.0709	0.289	0.0579	0.351	0.0702
45	CDF2Wasy'05	11	3.57	0.0541	0.614	0.0558	0.504	0.0459	0.521	0.0474	0.606	0.055	1.09	0.0991	0.235	0.0214
46	HERA-FL'11	9	1.82	0.0337	0.119	0.0132	0.0199	0.00221	1.37	0.152	0.0239	0.00266	0.118	0.0132	0.174	0.0193
47	HERAb'06	10	1.47	0.0244	0.203	0.0203	0.141	0.0141	0.674	0.0674	0.153	0.0153	0.208	0.0208	0.088	0.0088

TABLE XVI: Sensitivity values for Table XIV.

No.	Expt.	Values, CT14 HERA2 NNLO PDFs fitted without jet data													
		$ S_{u_v}^E $	$\langle S_{u_v}^E \rangle$	$ S_{d_v}^E $	$\langle S_{d_v}^E \rangle$	$ S_{\bar{d}/\bar{u}}^E $	$\langle S_{\bar{d}/\bar{u}}^E \rangle$	$ S_{d/u}^E $	$\langle S_{d/u}^E \rangle$	$ S_{H7}^E $	$\langle S_{H7}^E \rangle$	$ S_{H8}^E $	$\langle S_{H8}^E \rangle$	$ S_{H14}^E $	$\langle S_{H14}^E \rangle$
1	HERAI+II'15	56.6	0.0505	36.	0.0321	44.9	0.0401	58.8	0.0525	90.6	0.0809	95.4	0.0852	111.	0.0993
2	BCDMSp'89	66.3	0.197	26.4	0.0784	22.5	0.0667	38.	0.113	32.9	0.0975	31.4	0.0932	25.2	0.0748
3	CCFR-F3'97	77.1	0.896	67.2	0.781	10.4	0.121	31.6	0.367	10.1	0.117	11.3	0.131	14.4	0.167
4	CMS8jets'17	17.8	0.0962	14.9	0.0806	18.8	0.102	10.3	0.0559	39.9	0.216	40.5	0.219	41.4	0.224
5	NMCrat'97	36.9	0.3	27.8	0.226	49.	0.398	76.	0.618	8.66	0.0704	8.53	0.0693	8.13	0.0661
6	BCDMSd'90	18.7	0.0746	27.7	0.111	14.	0.056	21.8	0.0871	29.6	0.118	28.5	0.114	23.3	0.0933
7	CMS7jets'13	9.71	0.073	11.1	0.0831	10.5	0.0789	5.37	0.0404	46.	0.346	46.3	0.348	44.3	0.333
8	CMS7jets'14	8.55	0.0541	11.	0.0696	10.1	0.0637	4.64	0.0294	41.3	0.261	40.8	0.258	36.8	0.233
9	CDHSW-F3'91	35.7	0.372	32.4	0.337	4.86	0.0507	14.1	0.147	4.15	0.0433	4.81	0.0501	6.58	0.0686
10	E605'91	18.7	0.157	26.9	0.226	17.5	0.147	4.69	0.0394	9.25	0.0777	9.53	0.0801	9.73	0.0818
11	ATLAS7jets'15	6.46	0.0462	7.63	0.0545	10.6	0.0755	3.88	0.0277	22.9	0.164	23.	0.164	22.2	0.159
12	E866pp'03	25.9	0.141	15.1	0.0821	17.1	0.0931	13.5	0.0736	15.	0.0815	16.8	0.0912	20.7	0.112
13	CCFR-F2'01	8.94	0.13	13.5	0.196	8.88	0.129	10.8	0.156	17.4	0.252	16.5	0.239	13.	0.189
14	CDHSW-F2'91	10.6	0.125	13.1	0.154	3.2	0.0377	11.7	0.138	13.5	0.159	11.9	0.14	7.92	0.0931
15	D02jets'08	7.5	0.0682	6.58	0.0598	8.85	0.0805	3.82	0.0347	19.1	0.173	18.1	0.165	14.8	0.134
16	NuTeV-nu'06	1.77	0.0465	2.41	0.0634	6.75	0.178	4.4	0.116	8.23	0.217	7.87	0.207	6.62	0.174
17	CDF2jets'09	4.12	0.0572	3.74	0.052	6.35	0.0882	2.55	0.0354	14.2	0.198	13.4	0.187	10.6	0.148
18	ATL7jets'12	4.56	0.0507	4.96	0.0552	5.28	0.0587	2.2	0.0244	19.9	0.221	19.4	0.216	17.7	0.197
19	CCFR SI nu'01	1.2	0.0299	1.63	0.0408	4.11	0.103	2.92	0.0729	4.69	0.117	4.44	0.111	3.65	0.0913
20	CCFR SI nub'01	2.21	0.0581	1.03	0.0272	2.24	0.059	1.97	0.0519	5.15	0.136	4.95	0.13	4.27	0.112
21	ATL8DY2D'16	5.37	0.112	3.39	0.0707	6.03	0.126	7.15	0.149	3.53	0.0736	3.75	0.0781	4.29	0.0894
22	NuTeV-nub'06	2.22	0.0673	1.09	0.033	2.68	0.0813	3.03	0.092	2.62	0.0793	2.52	0.0763	2.2	0.0666
23	ATL7WZ'12	6.95	0.17	4.74	0.116	10.1	0.247	10.1	0.248	4.69	0.114	4.79	0.117	4.7	0.115
24	LHCb8WZ'16	4.91	0.117	5.9	0.141	11.7	0.28	12.7	0.302	3.58	0.0853	3.39	0.0807	2.6	0.062
25	CMS8Wasy'16	7.02	0.213	5.12	0.155	11.9	0.362	11.3	0.342	3.09	0.0937	3.1	0.0941	2.94	0.0891
26	E866rat'01	4.51	0.301	5.01	0.334	24.8	1.65	4.6	0.307	2.53	0.168	2.52	0.168	2.23	0.149
27	CMS7Masy2'14	4.92	0.447	3.67	0.334	10.7	0.976	11.5	1.04	0.609	0.0554	0.696	0.0633	0.856	0.0778
28	LHCb7ZWrap'15	3.66	0.111	5.08	0.154	7.41	0.225	8.33	0.252	3.37	0.102	3.13	0.0949	2.21	0.0669
29	ATL8ZpT'16	1.76	0.0391	1.13	0.0252	3.36	0.0746	2.67	0.0593	4.88	0.108	6.04	0.134	9.06	0.201
30	HERAc'13	0.902	0.0192	0.985	0.021	0.614	0.0131	0.84	0.0179	6.79	0.144	6.73	0.143	6.32	0.135
31	D02Masy'08	4.	0.445	2.6	0.289	2.85	0.316	4.36	0.485	2.32	0.257	2.41	0.268	2.4	0.266
32	CMS7Easy'12	1.99	0.181	2.15	0.196	5.2	0.473	5.24	0.477	0.227	0.0207	0.251	0.0228	0.294	0.0268
33	ZyD02'08	2.76	0.0986	2.68	0.0956	1.89	0.0675	2.	0.0714	1.63	0.0583	1.49	0.0531	0.925	0.033
34	ZyCDF2'10	2.54	0.0877	2.6	0.0897	2.15	0.0741	2.38	0.0821	1.35	0.0465	1.17	0.0404	0.679	0.0234
35	D02Easy2'15	2.8	0.215	4.46	0.343	1.26	0.097	4.08	0.314	0.621	0.0478	0.668	0.0514	0.823	0.0633
36	CDF1Wasy'96	1.29	0.118	2.35	0.214	1.24	0.113	3.21	0.292	0.493	0.0448	0.527	0.0479	0.589	0.0535
37	LHCb7WZ'12	0.76	0.0543	1.14	0.0815	1.36	0.0971	1.75	0.125	0.845	0.0604	0.745	0.0532	0.548	0.0391
38	ATL8ttb-pt'16	0.96	0.12	1.28	0.16	0.213	0.0266	0.227	0.0284	4.7	0.587	4.75	0.594	4.54	0.568
39	LHCb8Zee'15	0.349	0.0205	0.719	0.0423	0.884	0.052	1.14	0.0673	0.707	0.0416	0.586	0.0345	0.208	0.0122
40	ATL8ttb-mtt'16	0.629	0.0898	0.844	0.121	0.387	0.0553	0.231	0.033	2.23	0.319	2.34	0.334	2.5	0.357
41	ATL7ZpT'14	0.242	0.0302	0.193	0.0241	0.349	0.0436	0.547	0.0683	1.81	0.226	1.79	0.223	1.59	0.199
42	LHCb7Wasy'12	0.726	0.145	1.02	0.204	1.68	0.336	1.88	0.376	0.588	0.118	0.594	0.119	0.568	0.114
43	ATL8ttb-y_ave'16	0.324	0.0648	0.529	0.106	0.254	0.0508	0.151	0.0302	2.17	0.433	2.16	0.431	1.94	0.389
44	ATL8ttb-y_ttb'16	0.15	0.0301	0.499	0.0998	0.139	0.0278	0.141	0.0283	2.05	0.41	2.01	0.401	1.71	0.341
45	CDF2Wasy'05	0.638	0.058	0.768	0.0698	0.614	0.0558	1.36	0.124	0.413	0.0375	0.438	0.0398	0.468	0.0426
46	HERA-FL'11	0.0789	0.00876	0.043	0.00478	0.122	0.0136	0.119	0.0132	0.662	0.0736	0.582	0.0647	0.314	0.0349
47	HERAb'06	0.0953	0.00953	0.0979	0.00979	0.0933	0.00933	0.111	0.0111	0.676	0.0676	0.658	0.0658	0.564	0.0564

TABLE XVII: Sensitivity values for Table XV.

-
- [1] S. Dulat, T.-J. Hou, J. Gao, M. Guzzi, J. Huston, P. Nadolsky, J. Pumplin, C. Schmidt, D. Stump, and C.-P. Yuan, *Phys. Rev.* **D93**, 033006 (2016), 1506.07443.
- [2] L. A. Harland-Lang, A. D. Martin, P. Motylinski, and R. S. Thorne, *Eur. Phys. J.* **C75**, 204 (2015), 1412.3989.
- [3] R. D. Ball et al. (NNPDF) (2017), 1706.00428.
- [4] S. Alekhin, J. Blümlein, S. Moch, and R. Placakyte (2017), 1701.05838.
- [5] A. Accardi, L. T. Brady, W. Melnitchouk, J. F. Owens, and N. Sato, *Phys. Rev.* **D93**, 114017 (2016), 1602.03154.
- [6] H. Abramowicz et al. (ZEUS, H1), *Eur. Phys. J.* **C75**, 580 (2015), 1506.06042.
- [7] S. Alekhin et al., *Eur. Phys. J.* **C75**, 304 (2015), 1410.4412.
- [8] J. Gao, L. Harland-Lang, and J. Rojo (2017), 1709.04922.
- [9] J. Butterworth et al., *J. Phys.* **G43**, 023001 (2016), 1510.03865.
- [10] T.-J. Hou, S. Dulat, J. Gao, M. Guzzi, J. Huston, P. Nadolsky, J. Pumplin, C. Schmidt, D. Stump, and C.-P. Yuan, *Phys. Rev.* **D95**, 034003 (2017), 1609.07968.
- [11] S. Camarda et al. (HERAFitter developers' Team), *Eur. Phys. J.* **C75**, 458 (2015), 1503.05221.
- [12] R. D. Ball, V. Bertone, F. Cerutti, L. Del Debbio, S. Forte, A. Guffanti, J. I. Latorre, J. Rojo, and M. Ubiali (NNPDF), *Nucl. Phys.* **B849**, 112 (2011), [Erratum: *Nucl. Phys.*B855,927(2012)], 1012.0836.
- [13] R. D. Ball, V. Bertone, F. Cerutti, L. Del Debbio, S. Forte, A. Guffanti, N. P. Hartland, J. I. Latorre, J. Rojo, and M. Ubiali, *Nucl. Phys.* **B855**, 608 (2012), 1108.1758.
- [14] N. Sato, J. F. Owens, and H. Prosper, *Phys. Rev.* **D89**, 114020 (2014), 1310.1089.
- [15] H. Paukkunen and P. Zurita, *JHEP* **12**, 100 (2014), 1402.6623.
- [16] J. Pumplin, D. Stump, R. Brock, D. Casey, J. Huston, J. Kalk, H. L. Lai, and W. K. Tung, *Phys. Rev.* **D65**, 014013 (2001), hep-ph/0101032.
- [17] P. M. Nadolsky and Z. Sullivan, eConf **C010630**, P510 (2001), hep-ph/0110378.
- [18] J. Pumplin, D. R. Stump, J. Huston, H. L. Lai, P. M. Nadolsky, and W. K. Tung, *JHEP* **07**, 012 (2002), hep-ph/0201195.
- [19] P. M. Nadolsky, H.-L. Lai, Q.-H. Cao, J. Huston, J. Pumplin, D. Stump, W.-K. Tung, and C.-P. Yuan, *Phys. Rev.* **D78**, 013004 (2008), 0802.0007.
- [20] R. D. Ball, L. Del Debbio, S. Forte, A. Guffanti, J. I. Latorre, A. Piccione, J. Rojo, and M. Ubiali (NNPDF), *Nucl. Phys.* **B809**, 1 (2009), [Erratum: *Nucl. Phys.*B816,293(2009)], 0808.1231.
- [21] S. Carrazza, S. Forte, Z. Kassabov, and J. Rojo, *Eur. Phys. J.* **C76**, 205 (2016), 1602.00005.
- [22] C. Anastasiou, C. Duhr, F. Dulat, E. Furlan, T. Gehrmann, F. Herzog, A. Lazopoulos, and B. Mistlberger, *JHEP* **05**, 058 (2016), 1602.00695.
- [23] M. Czakon, N. P. Hartland, A. Mitov, E. R. Nocera, and J. Rojo, *JHEP* **04**, 044 (2017), 1611.08609.
- [24] R. Boughezal, A. Guffanti, F. Petriello, and M. Ubiali, *JHEP* **07**, 130 (2017), 1705.00343.
- [25] A. Accardi et al., *Eur. Phys. J.* **A52**, 268 (2016), 1212.1701.
- [26] D. Boer et al. (2011), 1108.1713.
- [27] S. Abeyratne et al. (2012), 1209.0757.
- [28] E. C. Aschenauer et al. (2014), 1409.1633.
- [29] J. L. Abelleira Fernandez et al. (LHeC Study Group), *J. Phys.* **G39**, 075001 (2012), 1206.2913.
- [30] H.-W. Lin et al., *Prog. Part. Nucl. Phys.* **100**, 107 (2018), 1711.07916.
- [31] M. Gockeler, R. Horsley, E.-M. Ilgenfritz, H. Perlt, P. E. L. Rakow, G. Schierholz, and A. Schiller, *Phys. Rev.* **D53**, 2317 (1996), hep-lat/9508004.
- [32] X. Ji, *Phys. Rev. Lett.* **110**, 262002 (2013), 1305.1539.
- [33] C. Schmidt, J. Pumplin, and C. P. Yuan (2018), 1806.07950.
- [34] G. R. Farrar and D. R. Jackson, *Phys. Rev. Lett.* **35**, 1416 (1975).
- [35] T. J. Hobbs, M. Alberg, and G. A. Miller, *Phys. Rev.* **C91**, 035205 (2015), 1412.4871.
- [36] T. J. Hobbs, J. T. Londergan, and W. Melnitchouk, *Phys. Rev.* **D89**, 074008 (2014), 1311.1578.
- [37] W. T. Giele and S. Keller, *Phys. Rev.* **D58**, 094023 (1998), hep-ph/9803393.
- [38] W. T. Giele, S. A. Keller, and D. A. Kosower (2001), hep-ph/0104052.
- [39] D. Stump, J. Pumplin, R. Brock, D. Casey, J. Huston, J. Kalk, H. L. Lai, and W. K. Tung, *Phys. Rev.* **D65**, 014012 (2001), hep-ph/0101051.
- [40] J. Gao, M. Guzzi, J. Huston, H.-L. Lai, Z. Li, P. Nadolsky, J. Pumplin, D. Stump, and C.-P. Yuan, *Phys. Rev.* **D89**, 033009 (2014), 1302.6246.
- [41] R. D. Ball et al., *JHEP* **04**, 125 (2013), 1211.5142.
- [42] <http://projector.tensorflow.org>.
- [43] PDFSense website: <http://metapdf.hepforge.org/PDFSense/>.
- [44] D. Cook, U. Laa, and G. Valencia (2018), 1806.09742.
- [45] L. van der Maaten and G. Hinton, *Journal of Machine Learning Research* **9**, 2579 (2008).
- [46] V. Khachatryan et al. (CMS), *JHEP* **03**, 156 (2017), 1609.05331.
- [47] J. Pumplin, *Phys. Rev.* **D81**, 074010 (2010), 0909.0268.
- [48] V. Khachatryan et al. (CMS), *Eur. Phys. J.* **C75**, 288 (2015), 1410.6765.
- [49] J. Pumplin, D. R. Stump, and W. K. Tung, *Phys. Rev.* **D65**, 014011 (2001), hep-ph/0008191.
- [50] R. Brock, D. Casey, J. Huston, J. Kalk, J. Pumplin, D. Stump, and W. K. Tung, in *Workshop on B Physics at the*

- Tevatron: Run II and Beyond Batavia, Illinois, September 23-25, 1999* (2000), pp. 159–161, [,159(2000)], hep-ph/0006148.
- [51] A. M. Sirunyan et al. (CMS), *Eur. Phys. J.* **C77**, 459 (2017), 1703.01630.
 - [52] T.-J. Hou et al., in preparation (2018).
 - [53] T.-J. Hou, S. Dulat, J. Gao, M. Guzzi, J. Huston, P. Nadolsky, C. Schmidt, J. Winter, K. Xie, and C. P. Yuan, *JHEP* **02**, 059 (2018), 1707.00657.
 - [54] A. C. Benvenuti et al. (BCDMS), *Phys. Lett.* **B223**, 485 (1989).
 - [55] A. C. Benvenuti et al. (BCDMS), *Phys. Lett.* **B237**, 592 (1990).
 - [56] M. Arneodo et al. (New Muon Collaboration), *Nucl. Phys.* **B483**, 3 (1997), hep-ph/9610231.
 - [57] J. P. Berge et al., *Z. Phys.* **C49**, 187 (1991).
 - [58] U.-K. Yang et al. (CCFR/NuTeV), *Phys. Rev. Lett.* **86**, 2742 (2001), hep-ex/0009041.
 - [59] W. G. Seligman et al., *Phys. Rev. Lett.* **79**, 1213 (1997), hep-ex/9701017.
 - [60] D. A. Mason, Ph.D. thesis, Oregon U. (2006), URL <http://lss.fnal.gov/archive/thesis/2000/fermilab-thesis-2006-01.pdf>.
 - [61] M. Goncharov et al. (NuTeV), *Phys. Rev.* **D64**, 112006 (2001), hep-ex/0102049.
 - [62] A. Aktas et al. (H1), *Eur. Phys. J.* **C40**, 349 (2005), hep-ex/0411046.
 - [63] A. Aktas et al. (H1), *Eur. Phys. J.* **C45**, 23 (2006), hep-ex/0507081.
 - [64] H. Abramowicz et al. (ZEUS, H1), *Eur. Phys. J.* **C73**, 2311 (2013), 1211.1182.
 - [65] F. D. Aaron et al. (H1), *Eur. Phys. J.* **C71**, 1579 (2011), 1012.4355.
 - [66] G. Moreno et al., *Phys. Rev.* **D43**, 2815 (1991).
 - [67] R. S. Towell et al. (NuSea), *Phys. Rev.* **D64**, 052002 (2001), hep-ex/0103030.
 - [68] J. C. Webb et al. (NuSea) (2003), hep-ex/0302019.
 - [69] F. Abe et al. (CDF), *Phys. Rev. Lett.* **77**, 2616 (1996).
 - [70] D. Acosta et al. (CDF), *Phys. Rev.* **D71**, 051104 (2005), hep-ex/0501023.
 - [71] V. M. Abazov et al. (D0), *Phys. Rev.* **D77**, 011106 (2008), 0709.4254.
 - [72] R. Aaij et al. (LHCb), *JHEP* **06**, 058 (2012), 1204.1620.
 - [73] V. M. Abazov et al. (D0), *Phys. Lett.* **B658**, 112 (2008), hep-ex/0608052.
 - [74] T. A. Aaltonen et al. (CDF), *Phys. Lett.* **B692**, 232 (2010), 0908.3914.
 - [75] S. Chatrchyan et al. (CMS), *Phys. Rev.* **D90**, 032004 (2014), 1312.6283.
 - [76] S. Chatrchyan et al. (CMS), *Phys. Rev. Lett.* **109**, 111806 (2012), 1206.2598.
 - [77] G. Aad et al. (ATLAS), *Phys. Rev.* **D85**, 072004 (2012), 1109.5141.
 - [78] V. M. Abazov et al. (D0), *Phys. Rev.* **D91**, 032007 (2015), [Erratum: *Phys. Rev.*D91,no.7,079901(2015)], 1412.2862.
 - [79] T. Aaltonen et al. (CDF), *Phys. Rev.* **D78**, 052006 (2008), [Erratum: *Phys. Rev.*D79,119902(2009)], 0807.2204.
 - [80] V. M. Abazov et al. (D0), *Phys. Rev. Lett.* **101**, 062001 (2008), 0802.2400.
 - [81] G. Aad et al. (ATLAS), *Phys. Rev.* **D86**, 014022 (2012), 1112.6297.
 - [82] S. Chatrchyan et al. (CMS), *Phys. Rev.* **D87**, 112002 (2013), [Erratum: *Phys. Rev.*D87,no.11,119902(2013)], 1212.6660.
 - [83] R. Aaij et al. (LHCb), *JHEP* **08**, 039 (2015), 1505.07024.
 - [84] R. Aaij et al. (LHCb), *JHEP* **05**, 109 (2015), 1503.00963.
 - [85] G. Aad et al. (ATLAS), *JHEP* **09**, 145 (2014), 1406.3660.
 - [86] V. Khachatryan et al. (CMS), *Eur. Phys. J.* **C76**, 469 (2016), 1603.01803.
 - [87] R. Aaij et al. (LHCb), *JHEP* **01**, 155 (2016), 1511.08039.
 - [88] G. Aad et al. (ATLAS), *JHEP* **08**, 009 (2016), 1606.01736.
 - [89] G. Aad et al. (ATLAS), *Eur. Phys. J.* **C76**, 291 (2016), 1512.02192.
 - [90] S. Chatrchyan et al. (CMS), *Phys. Rev.* **D90**, 072006 (2014), 1406.0324.
 - [91] G. Aad et al. (ATLAS), *JHEP* **02**, 153 (2015), [Erratum: *JHEP*09,141(2015)], 1410.8857.
 - [92] G. Aad et al. (ATLAS), *Eur. Phys. J.* **C76**, 538 (2016), 1511.04716.